ONE DIMENSIONAL ELECTRON SPIN IMAGING FOR SINGLE SPIN DETECTION AND MANIPULATION USING A GRADIENT FIELD

A Dissertation

by

CHANG-SEOK SHIN

Submitted to the Office of Graduate Studies of
Texas A&M University
in partial fulfillment of the requirements for the degree of

DOCTOR OF PHILOSOPHY

May 2008

Major Subject: Electrical Engineering

ONE DIMENSIONAL ELECTRON SPIN IMAGING FOR SINGLE SPIN DETECTION AND MANIPULATION USING A GRADIENT FIELD

A Dissertation

by

CHANG-SEOK SHIN

Submitted to the Office of Graduate Studies of
Texas A&M University
in partial fulfillment of the requirements for the degree of

DOCTOR OF PHILOSOPHY

Approved by:

Chair of Committee,	Philip Hemmer
Committee Members,	Ohannes Eknoyan
	Robert D. Nevels
	Jaan Laane
Head of Department,	Costas N. Georghiades

May 2008

Major Subject: Electrical Engineering

ABSTRACT

One Dimensional Electron Spin Imaging for Single Spin Detection and Manipulation Using a Gradient Field. (May 2008)

Chang-Seok Shin, B.S., University of Seoul, Republic of Korea;

M.S., Texas A&M University

Chair of Advisory Committee: Dr. Philip Hemmer

The ability to resolve molecules individually has many potential applications. These include understanding the local environments of single molecules including details of their interactions with surroundings. The ability to individually address and manipulate the spin states is also required for spin based quantum information processing. Although optical detection techniques, such as optically detected electron spin resonance (ESR) seem very powerful in these contexts, multiple molecules in the focal volume of a diffraction limited confocal microscope spot cannot in general be resolved individually. Here we propose to solve this problem using optically detected ESR imaging based on the use of high field gradients.

In the present research, subwavelength single molecule imaging is demonstrated by using the optically detected ESR technique and the optically detected electron spin echo envelope modulation (ESEEM) technique. Ultra fast Rabi nutation experiments are also performed to demonstrate the feasibility of fast spin manipulations at a low microwave power.

Micrometer sized gradient coils, together with micrometer sized co-planar microstrip transmission lines, are designed and fabricated by optical lithography in order to produce the necessary high magnetic field gradients. These fabricated devices are used to demonstrate this subwavelength imaging technique by imaging single electron spins of the nitrogen-vacancy (NV) defect in diamond. In this demonstration, multiple NV defects, unresolved in a single focal volume of a diffraction limited microscope are successfully resolved by the optically detected ESR techniques. Specifically, two neighboring NV defects separated by about 84nm are resolved. Ultra Fast electron spin nutation with an oscillation period of 1.33ns is also achieved by the high microwave magnetic field induced by the current flowing through the fabricated co-planar microstrip lines.

These optically detected ESR and ESEEM techniques combined with the micrometer sized gradient coil may find many applications, including single molecule imaging and quantum information processing.

DEDICATION

To my Lord Jesus Christ, and my family and parents.

ACKNOWLEDGEMENTS

There are a number of people who encouraged, guided, and helped me finish this work throughout my Ph.D. study and research process. No matter what their contribution was, it would not have been possible for me to accomplish my degree without them.

I first would like to give special thanks to my advisor Dr. Philip Hemmer for his support, guidance, and encouragement. His tremendous advice and mentoring was the most crucial part of my research, and his deep understanding of various fields including quantum information processing deserves my respect. I also want to give many thanks to Dr. Roman Kolesov for his help and co-work in the nitrogen-vacancy (NV) diamond project. He brought my lifeless knowledge to life, encouraged me to jump into the new fields, and extended my understanding of quantum system with theory. I also thank Dr. Fedor Jelezko and Dr. B. Gopala Krishnan (Gopi) in Stuttgart, Germany for the co-work in the ultra fast Rabi nutation experiments and single spin imaging experiments.

I thank my committee members, Dr. Robert Nevels, Dr. Ohannes Eknoyan, Dr. Jaan Laane and Dr. Mosong Cheng for their valuable instructions. I want to give many thanks to my colleagues, Dr. Zhijie Deng, Dr. Mughees Khan, Dr. Elizabeth Trajkov, Changdong Kim and Dr. Aleksander Wojcik for their contributions on the experimental setups. Without their contributions it would have been impossible for me to build and optimize the experimental setup. I also thank Huiliang Zhang, Honam Yum and Petr Anisimov for their help and the discussions we had. I give thanks to Mr. Robert Atkins

for his help to our lab and to the staff members of the materials characterization facility (MCF) for their assistance in the fabrication facilities. I also give my thanks to Dr. Petr P. Borbat at the National Biomedical Research Center for Advanced ESR Technology (ACERT), Cornell University, for his valuable suggestions on the design of high speed high current switches, and I thank Todd A. Zapata for editing my draft. I thank Texas A&M University and the electrical and computer engineering department faculty and staff for providing me wonderful opportunities to study here.

Many thanks go to my beloved friends in my church for their encouragement and prayers. Finally, special thanks to my lovely wife Yoonkyung, my beautiful daughters Mary and Phoebe for their patience and love, to my brother Changwoon for his encouragement, and to my extended family in Korea for their unconditional love.

NOMENCLATURE

NV	Nitrogen Vacancy
ESR	Electron Spin Resonance, which is also called Electron Paramagnetic Resonance (EPR)
ESEEM	Electron Spin Echo Envelope Modulation
MW	Microwave
RF	Radio Frequency
CW	Continuous Wave
FWHM	Full Width at Half Maximum
APD	Avalanche Photo Detector
TTL	Transistor-Transistor Logic
ECL	Emitter-Coupled Logic
ND	Nano Diamond
FFT	Fast Fourier Transform
EIT	Electromagnetically Induced Transparency

TABLE OF CONTENTS

CHAPTER Page

LIST OF FIGURES

FIGURE Page

FIGURE Page

FIGURE Page

FIGURE Page

FIGURE Page

FIGURE Page

FIGURE Page

FIGURE Page

FIGURE Page

LIST OF TABLES

CHAPTER I

INTRODUCTION: THE IMPORTANCE OF RESEARCH

A. Importance of the Research

Understanding local environments of molecules and their interactions has been one of the ultimate goals of the natural science for centuries. After the astonishment of scientific community by the first discovery of nuclear spin echoes by E. Hahn in 1950[1], and their application to Sodium-Ammonia solutions reported by Richard Blume[2], spin echo techniques including nuclear spin echo, electron spin echo, and electron-nuclear spin echo has been one of the fundamental tools to investigate 'molecules' in details.

Envelope modulation of the electron spin echo[3], optically detected electron spin echo[4], electron nuclear double resonance[5] and magnetic resonance[6] of a single molecular spin were also demonstrated. Though development of technologies has greatly enhanced the ability to understand dynamics of molecules, dynamics at single molecule level are still required to overcome the loss of information caused by ensemble averaging.

The detection and manipulation of spins in a single molecule is also important for quantum information processing. Recently, much quantum information research has been conducted on single nitrogen vacancy defects in diamond including coherent single spin detections, manipulations, and thereby solid state quantum bit realizations.

This thesis follows the style of *Nature*.

Optical detection techniques, such as optically detected ESR seem very powerful tools in these contexts. Due to the nature of the molecular structure, many molecules can exist in a small volume, and state-of-the-art-technologies, such as focused ion beam implantation make it possible to create a single defect, and/or many defects, such as nitrogen vacancy defects in nanometer scale volume. Therefore, quantum information applications require the ability to detect and manipulate single spins that are not resolved by the diffraction limited confocal microscope spot. Here we propose to solve this problem using ESR imaging based on the use of high field gradients.

Recently, atom trapping and manipulation in vacuum was demonstrated by using micro-electromagnets at low temperature (~20K)[7]. Micro-electromagnets with smallest feature size of 3μm by 1μm were fabricated on sapphire substrates by optical lithography followed by electroplating. A gold (Au) wire in micrometer size can support up to several amperes with power dissipation of 10kW/cm^2 at liquid nitrogen or helium temperatures in vacuum, and produce a field gradient of 1Gauss/nm. By using the field gradient created by such a micro-electromagnet together with optically detected electron spin resonance techniques, it is possible to resolve multiple defects present in the focal volume, and thereby spin manipulation of individual defects, with nanometer-scale separation, is feasible.

Micrometer sized microwave striplines can be integrated with the gradient field structures to simultaneously achieve ultra fast spin manipulation at low microwave powers.

This dissertation describes the optically detected ESR setup with experimental procedures and the design and fabrication of micro-electromagnets and microwave coplanar striplnes that operate at room temperature. The fabricated devices are then used to perform a proof-of-principle sub-wavelength imaging demonstration experiment using single NV spins in diamond. The devices described can find many applications, in single electron spin imaging, quantum computing applications, etc.

B. Review of NV Defects in Diamond in the Context of Solid State Quantum Computing

Diamond has many unique properties due to its rigid crystal structure[8]. But defects created by impurities or vacancy in diamond can change electrical, thermal, mechanical, and chemical properties of diamond. There are four types of diamond, i.e. type Ia, Ib, IIa, IIb depending on the concentration of the impurities, such as nitrogen atoms, or boron atoms. In type Ia diamond, substitutional nitrogen atoms are present in aggregate forms, but in type Ib diamond, they are present as isolated substitutional nitrogen atoms. Type IIa diamond is very pure, and there is no or very small amount of impurities. Type IIb diamond has boron atom impurities, but not any nitrogen atoms. Depending on the impurities present and its concentration, diamond absorbs different wavelengths, so it appears in different colors[9, 10, 11, 12].

Nitrogen vacancy (NV) defects have attracted much interest due to their optical properties. Vacancies created by radiation damage by high energy electrons or neutrons (~2MeV) migrate toward nitrogen atoms during the annealing process at over 900K. In

consequence, NV defects are formed. Annealing experiments, and optical studies suggested that NV defect consists of substitutional nitrogen atom and neighboring vacancy of carbon atom, and it is also suggested that it has trigonal symmetry (C_{3v}), and NV defects are formed along the C_3 major axis, which is the [111] direction[13].

It has been reported that NV defects possess many interesting optical properties described as follows. The fluorescence of NV defects was originally believed due to from an excited state (E^1) to lower state, a singlet state (A^1). Later, it was claimed that electronic ground state of NV defects is a triplet state (A^3). This is because the EPR signal observed under optical illumination was characteristic of a ground triplet state (A^3). The fluorescence lifetime of NV defects in type Ib natural diamond was determined to be 13ns, and 11.6ns in synthetic diamond[14]. The optical transition from $E^3 \rightarrow A^3$ gives rise to zero phonon line at 637nm with phonon side band to lower energy in emission. It was also proposed that optical relaxation from $E^3 \rightarrow A^3$ has a preference to the lower ground state spin sublevels, which may be used to polarize electron spins[15]. This was supported by experiments showing an optically detected spin coherence even without any external magnetic bias field[16]. It was further supported by optical hole burning experiments with non-zero external magnetic fields[17], electron nuclear double resonance by Raman heterodyne detection techniques[18], and nearly degenerate four-wave-mixing (NDFWM) spectroscopy that the electronic ground state is indeed a triplet state (A^3). It is also confirmed that a metastable singlet state (A^1) does exist, which was observed as ultra narrow Lorentzian-shaped resonance in NDFWM spectrum[19].

In the absence of external magnetic fields, the triplet ground spin states of NV defects are split into m_s=0 and m_s=+/-1 states with a zero field splitting of D=2.88GHz due to dipolar coupling of two unpaired electrons. This zero field splitting causes magnetic anisotropy, and strongly affects the magnetic properties of these defects. It can be detected as a resonant absorption of microwave electromagnetic energy by the electrons[20]. It is experimentally shown that zero field splitting, D is positive for NV, and optical illumination makes the NV spin polarize to the m_s=0 ground state[21]. It is estimated by modeling that the intersystem crossing rates of the excited m_s=+/-1 state to the metastable singlet state A^1 is three orders of magnitude higher than that of excited m_s=0 to metastable state, and that relaxation from the metastable state to triplet ground state is almost exclusively to m_s=0. In consequence, strong spin polarization to the m_s=0 state is prepared after a few cycles of optical pumping. The strong dependence of intersystem crossing rates upon spin orientation also results in a decrease of fluorescence intensity by about 30% upon simultaneous irradiation with resonant microwave electromagnetic energy (i.e. spin transition energy from m_s=0 to m_s=+/-1), and this can be used to identify the relative population of the electron spin states at room temperature[22].

The charge state of NV defects is either neutral with a zero phonon line at 575nm or negative with zero phonon line at 637nm. In type Ib diamond, negatively charged NV defects are dominant possibly due to the excess concentration of nitrogen impurities ~ 50 to 120 ppm[23]. However, recent experiments demonstrated that upon intense

irradiation at 514nm the charge state of NV defects can be converted from neutral (NV^0) to the negative (NV^-), or vise versa, and will relax back to the original state in the dark[24].

Much research including electron spin resonance measurements, electron nuclear double resonance measurements, nuclear magnetic resonance measurements, and optically detected magnetic resonance were performed in order to understand the local environment of NV defects in diamond. These studies gave dipolar coupling constants, hyperfine coupling constants, quadrupole splitting, etc[25, 26, 27]. Coupling constants of the electron spin of NV defects with their ^{14}N nuclear spins were experimentally determined to be $A_{\parallel}$=2.3MHz, $A_{\perp}$=2.1MHz, and P=-5.05MHz. For the coupling of electron spins with ^{13}C nuclear spin, $A_{\parallel}$=205MHz, $A_{\perp}$=123MHz[28].

When a non-zero external magnetic field is applied parallel to the [111] direction of the diamond, the otherwise degenerate electron doublet ground states (m_s=+/-1) show electronic Zeeman splitting with a linear dependence with a constant of $g_e\beta_e$=2.8MHz/Gauss vs. the magnetic field strength. When a weak magnetic field was applied (~ up to 200Gauss), strong nuclear modulation was observed in the Hahn echo decay, which was attributed to the hyperfine interactions of the nuclear spins of nearby ^{13}C atoms with the triplet spins of the NV defect electrons[29].

Two types of cross relaxations (CR) were observed, resulting in an abrupt change in the fluorescence emission: one is CR between NV defects and neighboring substitutional nitrogen atom when external magnetic field at 514Gauss is applied along [111] direction, the other between NV defects oriented along the external magnetic field and proximal NV defects oriented at 109.28 degrees from external magnetic field when

600Gauss of magnetic field applied along [111] direction. Especially for 0Gauss and 600Gauss cases, characteristic decay time T_d was greatly affected, T_d~250μs (decrease by a factor of 3 was observed), so that dipole-dipole interactions between NV defects were thought to be a main cause of the spin diffusion in samples with high NV concentrations[29]. However, recent studies on the NV defects in ultra pure type IIa diamonds showed that interactions of NV defects with neighboring substitutional nitrogen atom is the major source of spin decoherence in all but the most pure diamonds[30].

At about 1030 Gauss of external magnetic field along the (111) direction, the m_s=-1 level approaches to the m_s=0, but they do not cross due to the off-diagonal terms of the hyperfine interactions, which is known as level anticrossing (LAC). Wave functions close to the LAC are mixture of m_s=0 and m_s=-1, and at 1030Gauss equilibrium may be established between the population of m_s=0 state and of m_s=-1 state, therefore the optically detected EPR signal measured from the population difference between these states will disappear. However, the dephasing rate detected by the Raman heterodyne EPR echo signal did not show any dependency on the magnetic field near level anticorssing, which supported the assertion that LAC is not associated with the EPR signal collapse. This is verified using the Raman heterodyne scheme. If the RF frequency was kept the same, and magnetic field strength was swept across 1030Gauss, the Raman-heterodyne detected EPR signal reversed sign, which was attributed to the optical pumping to the m_s=0 state[31].

It was also experimentally shown that Raman EPR signal was only detected in the lower-energy side of zero phonon line, which was attributed to non-radiative internal relaxation of the excited state at a factor of 10 times faster rate than the inverse fluorescence lifetime on the higher-energy side[32]. However, recent measurements on single NV defects using our deposited electrodes disproved this assertion. Normally, both electron and nitrogen nuclear spins are preserved during the optical excitation and relaxation processes. But near LAC, ground spin states are mixed upon irradiation with a resonant RF signal, in consequence otherwise forbidden transitions are allowed.

When an external magnetic field at about 1028Gauss is applied with a slight misalignment (~0.2 to 0.6 degrees off) from the [111] direction, and a strong coupling RF signal is applied at a fixed frequency and weak probe RF signal is swept across the absorption band, electromagnetically induced narrow transparency can be observed in the ESR absorption spectrum. In a Λ configuration of the energy levels, this occurs when the energy difference between probing field and coupling field matches the transition frequency of two lower levels[33]. Furthermore, by applying an additional driving RF field together with coupling RF field and probing RF field, the EIT transparency feature splits in to a doublet or a triplet, which was attributed to the dynamic stark effect[34]. Such Raman-excited spin coherences may open the possibility of efficient preparation of quantum bits, and the ability to perform arbitrary single-quantum-bit rotations[35].

With the development of recent technologies, such as high resolution confocal microscopy, single photon detectors, etc., all the aforementioned research is being

extended to single molecules or few molecules at room temperature in the context of single molecule imaging, single spin detection and manipulation, and other applications including quantum cryptography for secure communications, and other quantum information processes.

The fluorescence of single NV defects was observed with confocal optical microscopy at room temperature, and optically detected magnetic resonance on a single NV defect was also reported, which made it possible to study local environments of the defect at the single molecular level[36]. Single defects were created in type Ib diamond after electron irradiation (2MeV with dosage of 10^{12} e/cm^2) followed by annealing at 900 degrees C. A fluorescence image was acquired with a home-built confocal optical microscope at room temperature. By reducing the radiation dosage, a fluorescence spot size of 330nm, close to diffraction limited spot size, was achieved, and further reduction in dosage did not decrease the spot size, but the average distance between spots increased. Therefore, this fluorescence spot could be assumed to be originated from a single defect.

However, due to the fact that the diffraction limited spot size of conventional fluorescent microscopy is much larger than a single defect, two or more defects orientated in the same direction within the same focal volume can not be resolved.

A non-classical dipolar emitter, such as a nitrogen-vacancy (NV) defect in diamond emits one photon at a time, i.e. when a single atom has absorbed one photon, it should return to the ground state by emitting one photon in order to absorb a second

photon. Therefore, in principle, photon correlation experiments can tell if there exists more than one defect.

Detectors generally have dead time of the same order as the correlation time, which makes it impossible to measure the arrival times between the photons with nanosecond resolution. But it can be overcome by using the Hanbury-Brown-Twiss setup with 2 avalanche photodiodes (APD)[37]. Second order autocorrelation function, $g^2(\tau)$ of the fluorescence signal from these 2 APDs with Hanbury-Brown-Twiss setup can be used to determine the number of defects in the focal volume of the diffraction limited spot, if the number of defects are only a few[38, 39].

It was also clearly shown that fluorescence intensity depends nonlinearly on the optical excitation power, which was efficiently modeled by 3 level systems including a metastable state[40]. Though NV defects have high quantum efficiency (~1), the collection efficiency is typically very low due to the total internal reflection, and aberrations caused by the high refractive index of the host material, and the signal to noise ratio is relatively low due to the background noise from the diamond crystal or other defects located near the focal volume.

In order to overcome these drawbacks, diamond nano-crystals (typical size of 50nm or less) were proposed as a single photon source. NV defects using a nano diamond crystal can be created in synthetic diamond powder from de Beers. The fluorescence lifetime of NV defects in a nano diamond crystal was determined to be 25ns, which is larger by a factor of 2 than that of defects in bulk diamond. This is attributed to the lower effective refractive index of nano diamond crystals spin-coated on

fused silica. The effective index is lower than that of bulk diamond, since the nano diamond crystals are smaller than the optical wavelength and surrounded in half air and half fused silica[41]. Due to the small size of nano diamond crystals, they can be easily implanted in a micro-cavity, deposited on a fiber tip, or used as biomarkers[42].

Nevertheless, it is still desired to create single defects in the bulk diamond especially for quantum computing applications, where quantum bits (or qubits) were realized by the interactions of the spins of a single NV defect with other spins, such as carbon nuclei, nitrogen nuclei, or the spins of a neighboring NV defect. It was reported that a single NV defect can be efficiently generated by implantation of nitrogen (^{14}N) ions in pure type IIa diamond (nitrogen concentration < 0.1 ppm)[43]. In order to confirm that the single NV defects created in type IIa diamond after ion implantation are from the implanted nitrogen ions, not from the intrinsic nitrogen impurities present in the diamond, nitrogen isotopes (^{15}N) were implanted (natural abundance of ^{15}N is 0.37%). Since ^{15}N has nuclear spin of I=½ (c.f. I=1 for ^{14}N), the hyperfine spectrum measured by ODMR can confirm that if NV defects are created by implanted nitrogen ions or naturally present nitrogen atoms[44].

In summary, due to the following superior properties of NV defects in diamond, much research on single spin detection, manipulation, and qubit operation were conducted in the context of solid state quantum computing. First, NV defects can easily be excited and detected due to strong electric dipole optical transition. Second, a high degree of spin polarization to the ground electronic state is automatically produced by optical excitation. Third, single-atom detection and single-atom electron spin resonance

have already been demonstrated for NV centers[45]. Fourth, NV centers are optically stable. Fifth, the host material is relatively non-magnetic, except for 1.1% ^{13}C isotopes,[46] so that the spin lifetime is relatively long even at room temperature[47] and $T_1 >$ 1 second was recently observed at low temperature. Sixth, at low temperature the optical homogeneous line-width is close to the radiative limit[48], so there is the possibility of spectrally resolving single color centers. Seventh, it has been demonstrated that over 1000's of NV centers can be created in a single spatial location, of volume < 200 nm^3, using a focused ion beam source[49].

Electron spin echo envelope modulation produced by coupling to the ^{14}N nucleus at high field (~1.3T) at low temperature, 1.4K, was demonstrated in the context of a single qubit operation. The authors also proposed that this work could be extended to two-quibt realization on a single defect[50]. Single spin states using nano diamond crystals at low temperature, and coherent oscillations of single electrons at low temperature and room temperature were demonstrated[51].

The hyperfine interaction of an electron spin with a nitrogen (^{14}N) nuclear spin[52], and of an electron spin with carbon (^{13}C) nuclear spins[53] on a single NV defect were observed. It was also proposed that un-perturbed spin coherences should have long lifetimes in the absence of optical excitation, due to the observed decrease of spin coherence lifetime on optical excitation. Rabi oscillations of a single nuclear spin (^{13}C) was observed, and a two quantum bit conditional quantum gate was experimentally demonstrated via the hyperfine interaction of the electron spin of a single NV defect and a nuclear spin of neighboring carbon atom (^{13}C)[54]. It was proposed that this quantum

gate should be scalable by fabricating arrays of NV defects with nm spacings using focused ion and electron beams[55], and the dipolar coupling between nearby NV molecules[56]. Anisotropic hyperfine interactions of the electron spin of a single NV defect with neighboring nitrogen nuclear spins were further studied by the magneto-photoluminescence microscope[57], and strong coherent coupling of the electron spin and nuclear spin of a single NV defect created by focused ion beam implantation in ultra pure type IIa diamond was also demonstrated, and phase coherence time, T_2 of 350μs was measured at room temperature[58]. Local environments created by proximal carbon atoms (^{13}C) and the other carbon atoms were further studied in terms of coherent coupling or dephasing, and it was demonstrated that individually isolated proximal nuclei in diamond can be coherently addressed, and manipulated via the nearby electron spin[59].

More details about single NV defects in diamond for quantum computing applications are found in the review papers[60, 61, 62].

C. Dissertation Outline

In chapter II, the concept of confocal microscopy and home-built laser scanning fluorescence confocal microscopy setup are reviewed. Experimental procedures including the CW ESR experiment, photon antibunching experiment, and pulse mode ESR and electron spin echo experiment are described in detail with preliminary results. Device fabrication including design of microwave stripline and gradient coil, optical lithography, copper electroplating, and etching process are also discussed.

In chapter III, one dimensional ESR imaging for a single spin imaging using a gradient coil are presented with the detailed experimental procedures and experimental results discussed. For single spin imaging purpose, electron spin echo envelope modulation (ESEEM) using a gradient coil is presented, and the results are discussed together with ESR experiments. In order to demonstrate the feasibility of ultra fast electron spin manipulation, fast Rabi nutation experiments are presented using the fabricated micrometer size co-planar microwave strip-lines.

In chapter IV, major results of this work are summarized, and future applications are discussed. References are listed in the reference section. In the appendix, home built circuits including logic conversion circuit from ECL to TTL, nano second switching circuit for DC current, and a ramp signal generator for MW frequency sweep are briefly described and photo images of the experimental setup are shown as well. PCB fabrication for MW circuit board is also briefly described.

CHAPTER II

EXPERIMENTAL SETUP WITH PRELIMINARY RESULTS AND DEVICE FABRICATIONS

A. Fluorescence Confocal Microscopy Concept and Experimental Setup

1. Optical Setup for Laser Scanning Fluorescence Confocal Microscope

The electron spin resonance (ESR) technique is one of the fundamental methods used to understand spin physics of the paramagnetic materials, such as NV defects in diamond. Optically detected ESR is of particular interest since the ESR technique can easily be integrated with fully developed confocal microscopy, and take advantage of its inherent high resolution. Since the optically detected ESR signal originates from the area which is being irradiated by the optical excitation, the resolution is at least as good as the diffraction limit.

In confocal microscopy, a coherent point source illuminates a tiny region of the sample under the microscope objective. Fluorescence signal is collected from the area, illuminated by the point source, but noise originating from other areas is efficiently rejected by the pinhole. In consequence, the quality of the images is superior to that of conventional microscopy in terms of sharpness and contrast.

A schematic diagram of confocal fluorescence microscopy is shown in figure 2.1.

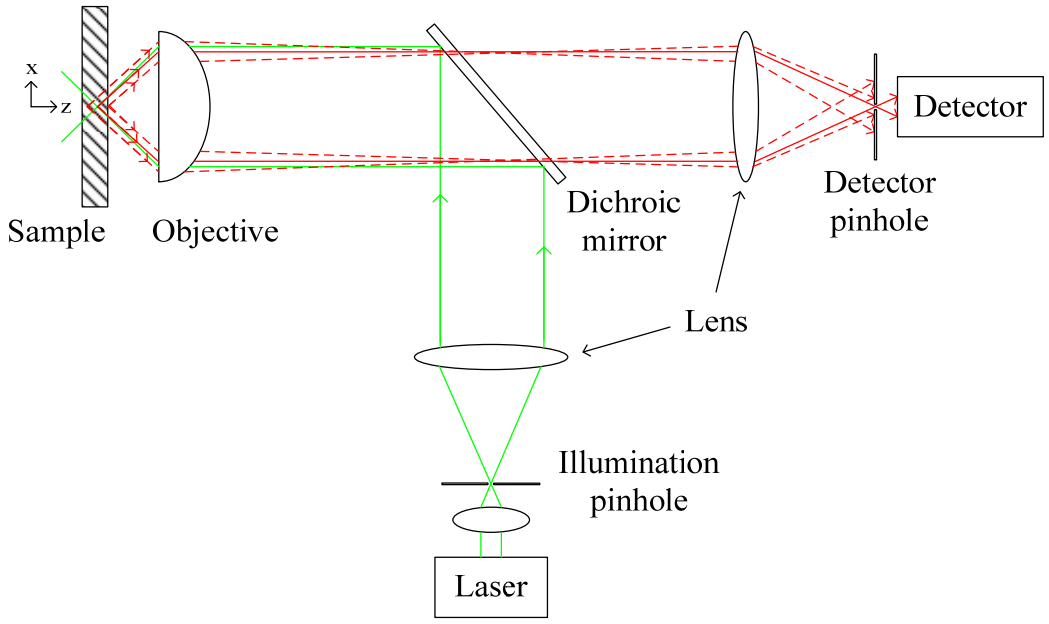

Figure 2.1 Schematic diagram of confocal fluorescence microscopy. Green solid line is for illumination, red solid or red dashed lines are for fluorescence.

There are two important features in the configuration of confocal microscopy. One is that illumination is a point source, which is a coherent laser or an illumination pinhole. The other is that a matching pinhole is placed before the detector. In the confocal configuration, the illumination pinhole, detector pinhole, and focal point of the objective should all be in an optically equivalent plane, and the pinholes should be accurately aligned relative to each other. In this configuration, a single point located in the focal plane of the objective will be illuminated by the point source, and the scattered light will be imaged on the detector pinhole, and will efficiently pass through to illuminate the detector. Any other stray light rays originated from below or above the focal plane, or to either side, will be rejected by the detector pinhole. Therefore, the confocal configuration gives higher contrast.

Since signal is collected from a specific focal plane, optical sectioning is possible by moving the sample along the z-axis, so that three dimensional imaging can be done by using a stack of optical sections.

The point spread function (PSF) is a measure that quantifies the performance of an imaging system[63]. There are two independent point spread functions in the confocal microscopy setup: one for the point source, which describes the distribution of the source light in the object focal plane, and the other for the return light, which describes the distribution of light in the image of the point source in the object plane projected onto the detector pinhole plane. Since they are independent, the total PSF of a confocal microscopy is the product of the PSF for the source and the PSF for the return light.

When a point source is focused by a lens, the intensity of the image in the focal plane varies spatially. This is defined as an intensity PSF, $I_h(r) = |h(r)|^2$ where $h(r)$ is Airy function in the paraxial approximation.

$$h(r) = \frac{2 \cdot J_1(\upsilon)}{\upsilon} \tag{2.1}$$

where $J_1(\upsilon)$ is the first order Bessel function of the first kind, $\upsilon = krn\sin(\theta_o) = kr(N.A.)$ and $k=2\pi/\lambda$, and $N.A.$ is the numerical aperture of the lens. The full width at half maximum (FWHM) of an intensity PSF is given by

$$d_{3dB} = \frac{0.51\lambda}{N.A.} \tag{2.2}$$

The Airy function has its first null at $\upsilon = kr(N.A.) = 3.83$, therefore the full width at first null is given by

$$d_{null\ to\ null} = \frac{1.22\lambda}{N.A.} \tag{2.3}$$

and 84% of the total power is distributed within the first Airy ring. Here, a single lens system with immersion medium of air is assumed,

However, equation (2.3) should be modified for the case where an infinity corrected lens system is used, the immersion medium is not air, or numerical aperture of the objective lens is so large that paraxial approximation is no longer valid. For the infinity corrected lens system with an arbitrary immersion medium, the diffraction limited spot size can be calculated by[64]

$$d_{\infty} = 1.22\lambda \left[\left(\frac{n_o}{N.A.} \right)^2 - 1 \right]^{1/2} \tag{2.4}$$

In our experimental setup, an oil immersion microscope objective (UPLSAPO 100XO, *N.A.* = 1.4, Olympus), with immersion oil n_o=1.517 (Chemika 56821 from Fluka) are used. From equation (2.4), the diffraction limited spot size with a 532nm laser is calculated to be 270nm at the focal point of the objective lens.

Now in order to choose the right size for the detection pinhole, the spot size of the return light at the detection pinhole plane should be calculated. This is approximated by simply adding the magnification of the objective lens to equation (2.4).

$$d_{pinhole} = 1.22\lambda M \left[\left(\frac{n_o}{N.A.} \right)^2 - 1 \right]^{1/2} \tag{2.5}$$

The focal length of the infinity corrected microscope objective lens in our setup is f_o= *L/M* =1.8mm, where *L* is designed tube length of 180mm, and *M* is designed

magnification of 100. A relay lens with focal length, f_t=175mm is used before the detector pinhole, so the effective magnification is $M_e=f_t/f_o$ =97.2. The fluorescence spectrum of negatively charged NV defects ranges from 637nm to 800nm. Since we do not want to lose any signal, λ=800nm was used to calculate spot size of the return light at the detection pinhole plane, which gave $d_{pinhole}$= 39.6μm. This may be used to determine the pinhole size.

The output of the single mode fiber serves as an illumination pinhole, and an oil immersion objective lens serves as the illumination focusing lens and the fluorescence collecting lens at the same time. A schematic diagram of the excitation part of home-built laser scanning confocal microscopy setup is shown in figure 2.2. A diode laser pumped Nd:YAG laser at 532nm (Compass 315M-100, Coherent) was used as an excitation laser with a maximum output power of 100mW. The Nd:YAG crystal has very strong absorption band around 800nm, so it is efficiently pumped by a diode laser at 800nm. Since the fundamental wavelength of Nd:YAG crystal is 1064nm, the 532nm laser line is achieve by using a frequency doubling resonator.

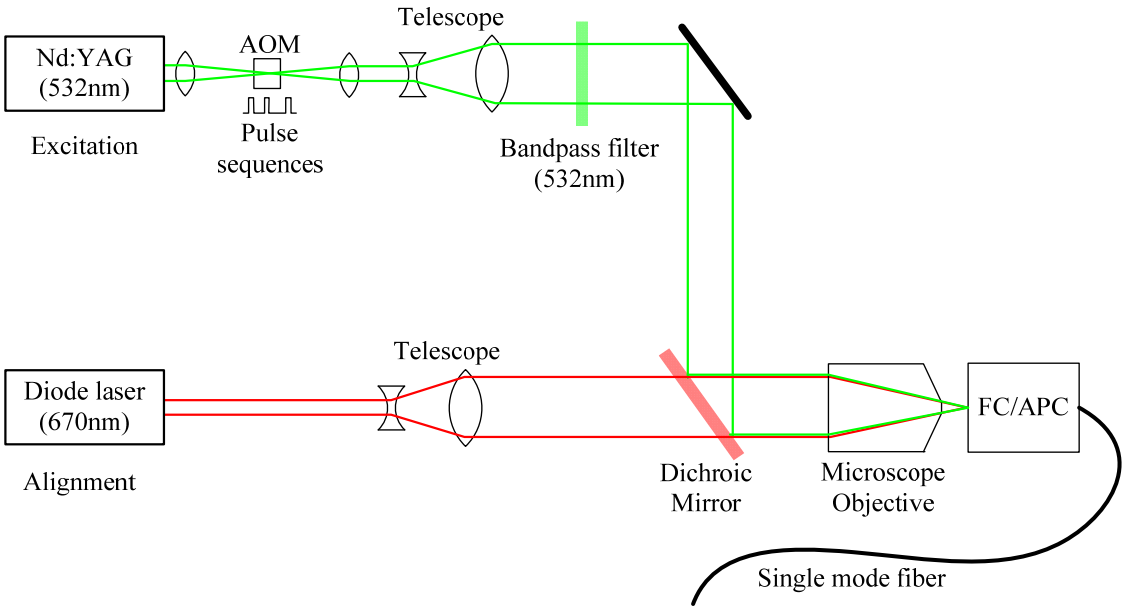

Figure 2.2 Schematic diagram of the excitation part of the home-built laser scanning confocal microscopy setup.

Typically, a long-pass filter is placed at the detection channel, so that shorter wavelengths, such as the excitation wavelength is efficiently rejected, but longer wavelengths of the excitation laser, such as 800nm, and 1064nm can pass through, thereby becoming a serious source of background noise. In order to purify the excitation wavelength, an interference filter at 532nm with a 3nm bandwidth was used. Since the spectrum of the fluorescence from NV defects is from 637nm to 800nm, aligning the detection pinhole using 523nm may not be accurate due to the chromic aberrations of the optics. Therefore a diode laser at 670nm (ThorLabs) serves as an alignment laser for the detection channel. Both excitation laser and alignment laser are combined by the dichroic mirror (Optarius), and coupled into the single mode fiber (PM460-HP, ThorLabs). Telescopes (Zoom beam expanders, Melles Griot) are used to expand the beam diameters of the excitation laser (532nm) and the alignment laser

(670nm), respectively, such that they match the entrance pupil of the microscope objective lens (Plan Achro, 10X, N.A.=0.25, American Optics). In this way, the beam diameters are a minimum at the focal plane and use the full numerical aperture of the objective. This situation gives maximum coupling efficiency into the fiber core. Typically, maximum coupling efficiency is about 55%. The input side of the single mode fiber is connectorized with FC/APC ends in order to avoid Fabry-Perot interference effects caused by back-reflections from the output side of the fiber, which is connectorized with FC/PC. The output beam of the single mode fiber with the FC/PC connector is a Gaussian profile, and excitation laser and alignment laser are almost overlapped to each other.

Electron spin manipulation should be carried out in the absence of the optical excitation in order to avoid re-distribution of the electron spin state by optical pumping. An acousto-optic modulator (AOM) is used to switch on/off the optical excitation in nano seconds. An RF signal, which is switched by an external TTL input, is converted by AOM transducer into a sound wave, which travels in the Lead Molybdate ($PbMoO_4$) crystal of the AOM. Due to the refractive index variations induced by the sound wave, the incoming light will be deflected. Therefore the AOM together with iris aligned to pass only the first order deflected beam switches the optical excitation on/off. In our setup, an AOM (1205C-2, ISOMET) together with digital RF driver (220 Series, ISOMET) are used. Typically, for this type of AOM, the deflection efficiency and switching (or rising/falling) time are inversely related. The reason is that the AOM is designed to give maximum deflection efficiency for a large beam diameter, but

switching time is slow due to the time it takes the sound pulse to cross the laser beam. A smaller laser beam switches faster but has lower diffraction efficiency, due to the AOM design. Here a plano-convex lens with a focal length of 150mm was used before the AOM to achieve a small focused beam and therefore a fast switching time. The lens was placed at 180mm before the AOM, since the laser beam was diverging. At the lens position, the incoming laser beam diameter is about 3mm, and beam waist of the focused laser spot was 65μm, measured using burn papers in the air. With this configuration, the deflection efficiency for the first order mode is 51%, and the rise time is 14ns, and fall time is 23ns. Though the RF driver of the AOM has delay time of only 12ns, total delay time of 250ns was measured, which was attributed to the slow sound wave velocity in the crystal, i.e. 3.63mm/μs. Specifically, when the RF signal is applied to the transducer, a sound wave is generated, and travels along the crystal. The refractive index modulated by the sound wave deflects the laser beam. Since the lateral distance between the transducer and the region where laser beam is passing is about 1mm, it will take about 300ns for the sound wave to arrive at the region, and thereby switching of the laser beam is delayed.

A schematic diagram of the imaging and detection part of home-built laser scanning confocal microscope is shown in figure 2.3. Here, another microscope objective lens (Plan Achro, 10X, N.A=0.25, American Optics) serves as a collimation lens for the output beam of the single mode fiber. Since the smallest spot size at the sample, i.e. the diffraction limited spot size, is achieved when the input beam diameter is matched to the entrance pupil of the microscope objective lens (i.e. oil immersion lens at

the sample), a set of lenses can be inserted after the collimation M.O. lens so that we have enough degrees of freedom to change the laser beam diameter, while keeping the correct collimation.

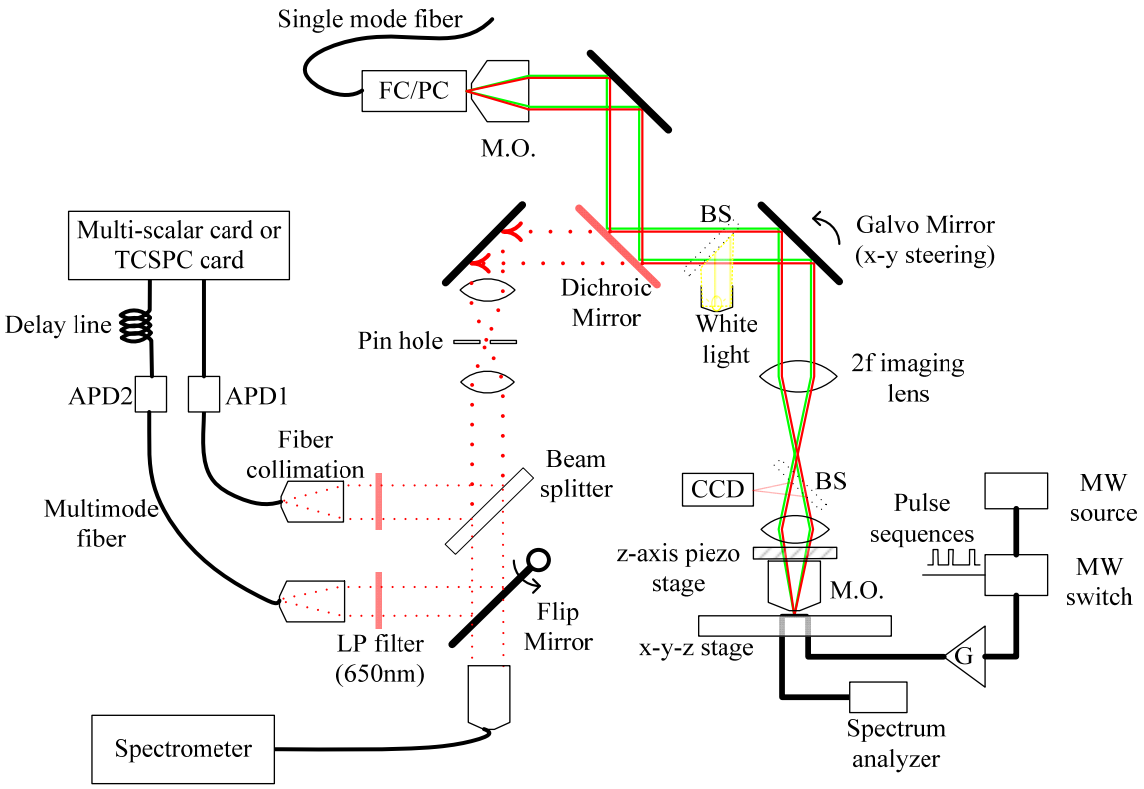

Figure 2.3 Schematic diagram of the imaging and detection parts of home-built laser scanning confocal microscopy setup. Solid lines indicate the optical path for excitation and alignment lasers, and dotted line indicates the optical path for fluorescence signal.

Two Galvanometer mirrors (MicroMax Series 670, Cambridge Technology, Inc.) located at 2f distance before the imaging lens (Achormatic, Plano-Convex, f=200mm, Thorlabs) steer the output beam in x-y directions. The steering motions (or angular motions) of the beam are imaged by the lens at 2f distance after the imaging lens. At this position, the beam is re-collimated by an identical lens, and immediately directed

into the microscope objective lens. The objective lens converts the angular motion of the laser beam into the x-y position scanning motion in the object plane.

Focusing of the microscope objective is precisely controlled by a piezo stage (Z-axis lens positioning system, Piezosystem Jena, Inc.). A CCD camera and white light illumination are inserted with beam splitters to produce a white light image on a TV screen.

The fluorescence signal collected by the objective lens follows the optical path backwards. It is filtered by a dichroic mirror (Optarius) and a long pass filter (FEL0650, Thorlabs) in order to remove background light such as stray light from excitation laser, room light, or the Raman scatter from the sample. The noise wavelengths are identified by the spectrometer, and rejected by using proper filters. The fluorescence signal is also spatially filtered by a pinhole in order to reject background light originated from other than the focal volume, and then it is directed to detectors.

The spatially and spectrally filtered fluorescence signal is coupled into the multimode fiber (AFS50/125Y, Thorlabs) by a fiber collimation lens (F260FC-B, Thorlabs), and detected by the two APDs (SPCM-AQR-13-FC, PerkinElmer), or the spectrometer (MicroSpec, Roper Scientific Acton Research). Optics, such as mirrors, beam splitters, fibers, etc were checked for their sensitivity to room light noise in the absence of the laser excitation, and then covered properly in order to reject any room light noise.

When a single photon arrives at the APD, it generates a 35ns TTL pulse. This TTL output pulse is recorded by the multichannel scaler (SR430, Stanford Research Systems Inc.), and the recorded data is passed to a computer via a GPIB interface in order to generate a fluorescence image, or to perform pulsed ESR experiments. In order to perform time correlation experiments, i.e. photon antibunching experiments, TTL output pulses from APD1 and APD2 are used as a start pulse and a stop pulse, respectively, for the TCSPC module (Time correlated single photon counting module, Becker & Hickl GmbH).

Good optical alignment is crucial to get the maximum signal to noise ratio with the highest resolution achievable. Alignment of the optics, and optimization were carried out as follows. First, the optical excitation (532nm) is correctly focused in the objective lens object plane in order to get smallest spot size and the maximum power density at the sample. The smallest focused beam diameter can be achieved by first matching the beam diameter of the laser to that of the entrance pupil of the objective lens. Assuming that the excitation laser, alignment laser and white light illumination are properly collimated, then they should all focus in the same plane on the sample. However when the CCD camera is placed at the objective lens image plane, the excitation laser (532nm) can often be slightly out of focus when the white light or alignment laser (670nm) are in focus, due to the aberrations, especially chromatic aberrations from the optics.

Initial alignment was done by using the alignment laser (670nm) to get the smallest spot at the TV screen, and to get the maximum retro-reflected light intensity at

the detector. After that, the fluorescence image was acquired from a spin-coated nano-diamond crystal sample, which contains single NV defects. Once a single defect was identified by an antibunching experiment, a series of fluorescence images were acquired by changing the fine focus of the objective lens. At this time, signal was coupled into the multimode fiber leading to the detector, but the pinhole was not placed. Due to the large core size of the multimode fiber, most of the fluorescence signal is detected, so that it is possible to obtain fluorescence images, which are the replicas of the cross section of the excitation laser spot in the object plane of the objective lens.

Figure 2.4 shows a series of fluorescence images of the spin-coated nano-diamond crystals obtained by adjusting the focus of the objective lens. One turn of the fine focus adjustment knob of the Z-axis piezo lens positioning system in the counter clock wise direction moves the objective lens focus about 400nm out of the sample. Here, the optical excitation power was adjusted to avoid any saturation. When the focus of the excitation laser was about 400nm off from that of the alignment laser, the best fluorescence image was obtained in terms of the spot size and the brightness.

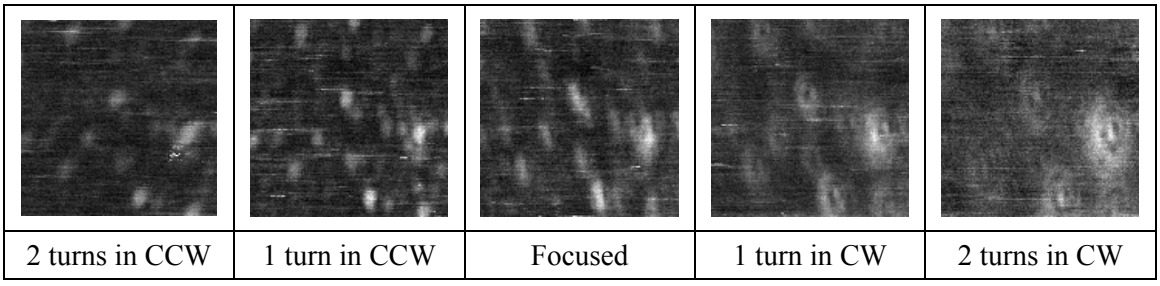

2 turns in CCW	1 turn in CCW	Focused	1 turn in CW	2 turns in CW

Figure 2.4 Fluorescence images of spin-coated nano-diamond crystal. It was initially focused with the alignment laser (670nm). Scanned area is about 6μm by 6μm.

Now the focus knob was adjusted to the best fluorescence image, and the position of the CCD camera was moved to get the smallest excitation laser spot on the TV screen. In this way, the excitation laser will be correctly focused when the smallest excitation laser spot is shown on the TV screen.

Second, the optimum size of the pinhole on the detection channel should be determined, and it should be properly aligned with the fluorescence optical axis. The calculated pinhole size from equation (2.5) was about 40μm. Once the focus of the excitation laser was adjusted to get smallest spot on the TV screen, a pinhole was carefully inserted into the detection channel as seen in the schematic diagram in figure 2.3, and aligned to get the maximum fluorescence signal. In order to achieve a higher signal to noise ratio, the actual pinhole size and its location should be determined by a compromise between how efficiently the fluorescence signal originating from out of the object focal plane is rejected, while still keeping as much fluorescence signal as possible from a single NV defect. First, in order to determine the pinhole position, the pinhole was moved along the optical axis, and the focus of the excitation laser was adjusted to get maximum signal at each pinhole location. In this way we can simultaneously find the best focus of the optical excitation, and the proper location of the pinhole along the optical path. The fluorescence photon count rates from a single NV defect as a function of pinhole position are shown in figure 2.5 (a). Once the focus of the excitation laser was optimized , we can see how efficiently the fluorescence signal originating from out of focal plane is rejected by the pinhole as seen in figure 2.5 (b). This time, focus of the excitation laser was fixed at a single NV defect, but the location of the pinhole was

moved along the optical path, and fluorescence signal was recorded as a function of pinhole location.

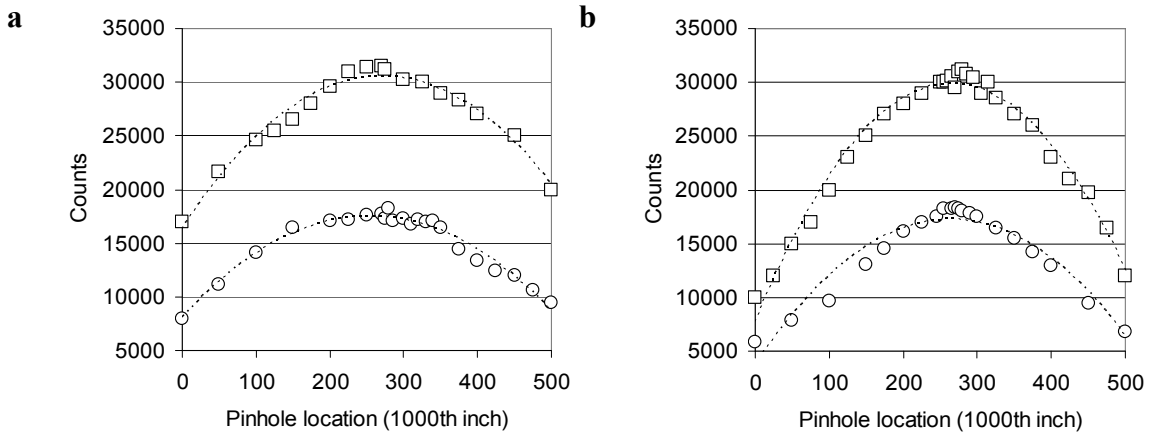

Figure 2.5 **a**, Fluorescence photon counts rate from a single NV defect was recorded along the optical path while the excitation focus and pinhole location changes at the same time. **b**, It is recorded while pinhole location changes, but the excitation focus was kept the same. Square is for 50μm pinhole, and circle is for 40μm pinhole.

The 40μm pinhole rejects background noise originating from out of the object focal point more efficiently than 50μm pinhole due to its small size, but signal count rates for the 40μm pinhole were smaller than for the 50μm pinhole by a factor of 2 as seen figure 2.5. When a signal to noise ratio, defined by the ratio of signal counts from a single NV defect over the background counts, was calculated, it was 4.67 with the 40μm pinhole, and 4.37 with the 50μm pinhole. Since the 50μm pinhole gives twice signal more than the 40μm pinhole with about the same signal to noise ratio, the 50μm pinhole was chosen in the setup.

Normalized antibunching curves on a single NV defect with various pinhole sizes are shown in figure 2.6. Photon antibunching experiments are discussed in detail in the next section.

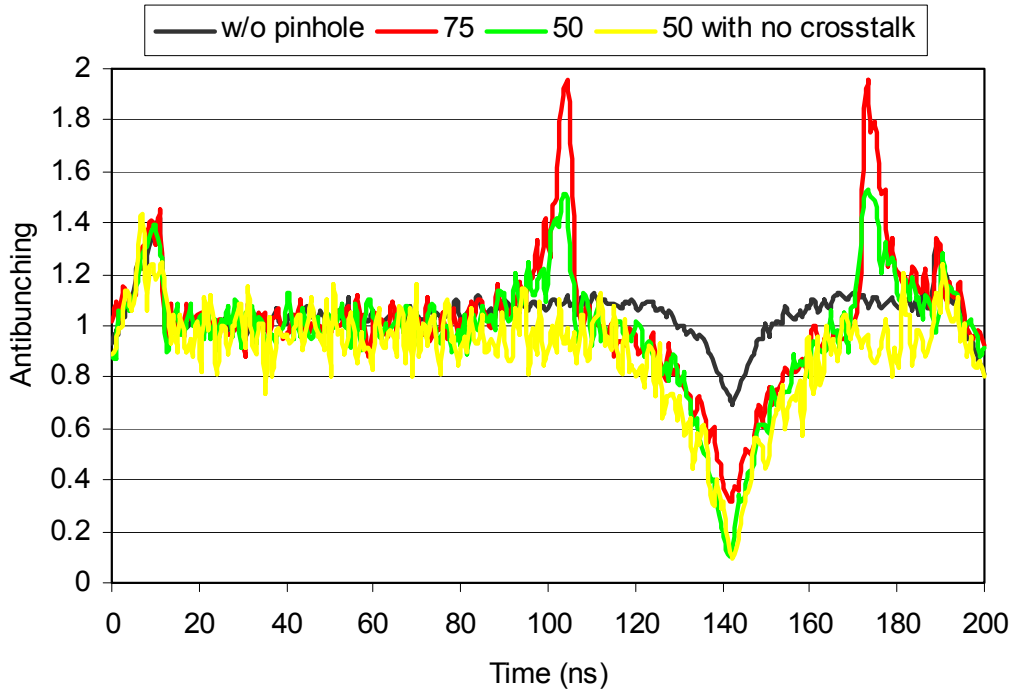

Figure 2.6 Normalized antibunching curves with various pinhole sizes in microns as indicated in the legend. Optical excitation of 90μW is applied for the cases of 75μm pinhole, 50μm pinhole, and 200μW for the case of without pinhole.

Theoretically, the antibunching dip for a single photon emitter, such as a single NV defect should go down to zero. However, NV defects present out of the object focal plane can be irradiated by the unfocused optical excitation, and fluorescence signal from these behaves as noise signal. When there is no pinhole inserted, the antibunching dip was 0.72. But, this decreased to 0.32 or 0.11 by inserting 75μm or 50μm pinholes,

respectively. So the 50μm pinhole most efficiently rejected the background noise originating out of the object focal plane or either side of the focal point.

After inserting a pinhole of, either 50μm or 75μm, unexpected peaks on either side of antibunching dip i.e. at 104ns, and 173ns showed up. This is attributed to the optical crosstalk between two APDs[65]. When photons hit the APD, an avalanche of hot carriers is triggered. In consequence, a small amount of light with spectral range of 600nm to 1000nm is emitted from APD. This emission spectrum follows optical path in the reverse direction, and is reflected back, and detected by either of the APD. Due to the wide range of this emission spectrum, which overlaps the spectrum of NV defects, this can not be efficiently filtered out by the optical filters. In our setup, a large reflection of this APD emission occurs at the back surface of the pinhole, and the lens surface. Without changing the optical alignment, the pinhole and lens were tilted by about 10 degrees, so that the reflected emission signal could not be detected by the APDs. As a result, this optical crosstalk was efficiently rejected, and thereby the unexpected peaks disappeared as shown in figure 2.6.

In summary of this section, concept of the confocal microscopy was discussed, and home-built laser scanning confocal microscopy was developed. Signal to noise ratio of the home-built confocal microscopy was good enough to distinguish if the defects are singles or not by doing photon antibunching experiments, which is discussed in section B of the chapter II.

2. Timing Control for ESR Experiments

As mentioned previously, in the CW ESR experiment, coherent electron spin-manipulation should be carried out in the absence of the optical excitation, and then detected by a short optical probe pulse. Manipulation of the ground state electron spins is performed by applying a resonant microwave signal. The microwave signal from the source (HP8350B with HP83592A, Hewlett-Packard) is switched on/off by a microwave switch (Ultra high speed SPST, Custom microwave components, Inc.), and then amplified by a 20Watt TWT amplifier (1277H, S-Band, Hughes). The time averaged microwave signal level is checked by a spectrum analyzer (492, Tektronix) during the experiment. The microwave circuit board and fabricated devices were tested by a vector network analyzer (HP8510B, Hewlett-Packard) beforehand.

In general, each piece of equipment has a different response time. In order to acquire valid data, accurate timing control is crucial. A schematic diagram for timing control of the equipment is shown in figure 2.7. Here, a digital delay/pulse generator (DG535, Stanford Research System Inc.) serves as a master timing control. The digital delay/pulse generator outputs TTL pulses with a pre-determined width at a certain temporal location with a pre-determined triggering rate. TTL output signal is converted into a ramp signal (0~10Volts) by a home-built ramp signal generator, which sweeps the frequency of the microwave source.

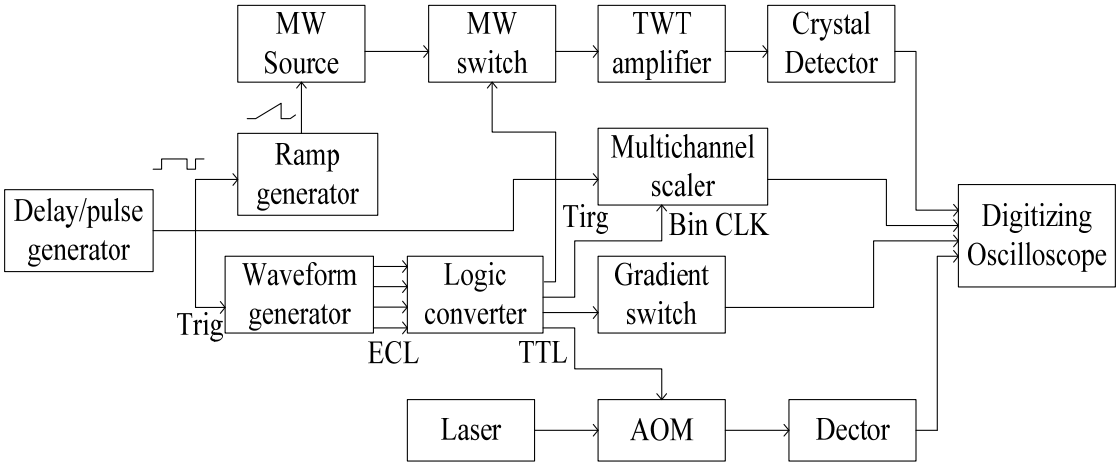

Figure 2.7 Schematic diagram for timing control of the equipments.

At the same time, this TTL signal triggers the multichannel scaler for data acquisition and the arbitrary waveform generator (AWG2041, Tektronix) for pulse sequence generation. The digital outputs of the AWG2041 are ECL signals that are converted into TTL signals by a home-built logic converter. TTL signal from each channel of the logic converter switches on/off the optical excitation via the AOM, the microwave signal via the microwave switch, or the DC gradient pulse via the gradient pulse switch, and serves as a clock signal for the respective bins of the multichannel scaler. A digitizing oscilloscope (TDS640A, Tektronix) is used to check their synchronization. The maximum delay time of the delay generator should be long enough to compensate for any delay caused by the slow response of electronic equipment, by an optical path, or delay by a coaxial cable length.

First, the time delay between optical excitation and the microwave signal was measured as follows. A high speed APD module (C5658, Hamamatsu) to detect the optical excitation and a crystal detector (423A, Hewlett-Packard) for the microwave

signal are placed at the sample location, and output signals from each detector are measured after the same length of coaxial cables by the digitizing oscilloscope. Delay caused by the crystal detector or the optical detector are typically negligible compared to overall delay of the microwave signal, or optical excitation signal, therefore the detectors were assumed to have zero second delay. Total time delays for the optical excitation signal and for the microwave signal are measured to be 250ns, and 60ns, respectively. Therefore, the microwave signal should be delayed by 190ns in order to be synchronized with the optical excitation.

The delay time between the fluorescence signal and data acquisition of the multichannel scaler was measured as follows. It is assumed that the excitation (green) laser instantaneously generates a fluorescence (red) photon at the sample surface. The multichannel scaler card is triggered at the rising edge of the master trigger signal, when the excitation laser generates a 'red' photon, which travels along the optical path and is detected by the high speed APD. When this red photon arrives at the photon counting APD on the detection channel, this APD outputs a 35ns TTL pulse corresponding to the detected 'red' photon, which then travels along the coaxial cable, and arrives at the multichannel scaler, which then puts out a its own signal. The delay time, which is the time difference between the trigger signal and the output signal of the multichannel scaler card, was measured to be 60ns, i.e. it takes 60ns for the 'red' photon to be recorded by the multichannel scaler.

A current pulse for the magnetic field gradient is generated by the DC gradient switch shown in figure 2.7. At the sample location, the delay of the current pulse with

respect to the microwave signal was measured, i.e. 43ns. But due to the distributed inductance of the striplines on the microwave circuit board, and of the fabricated device, the net rise time was measured to be about 5ns. In the experiments, especially for the frequency swept experiments, it is desired to have a constant magnetic field while the microwave signal is being applied, since the electronic Zeeman splitting is proportional to the magnetic field strength. Therefore, a total advance time of 143ns is applied to the input signal of the gradient switch.

For the frequency swept experiments, a TTL output pulse of the delay/pulse generator is applied to the input port of the ramp signal generator, which converts it into a 0 to 10Volt ramp signal according to the TTL pulse width. The microwave frequency is linearly mapped on to the bin numbers of the multichannel scaler. In order to keep the time-averaged microwave power dissipation the same, total sweep time was adjusted from 2.6ms to 10ms in 512 sets equally spaced bin sets depending on the maximum current applied to the DC gradient coil. Each set of data bins consists of two bins, i.e. one bin for the fluorescence signal produced by the probe pulse excitation, and another bin for the fluorescence signal produced by the preparation excitation pulse. The probe pulse is short enough that it does not completely polarize the spin whereas the preparation pulse is much longer and does completely polarize the spin to m_s=0 state. Therefore, when the fluorescence signal generated by the probe pulse is subtracted from the fluorescence signal generated by the preparation pulse the difference gives the net magnetization signal of the spins. Data from the bin for the preparation pulse is used to optimize the width of the probe pulse at a given optical excitation power. If the probe

pulse width is too short at a given optical excitation power, only part of the spin polarization will be detected during the probe pulse, and the remaining spins will be detected by the preparation pulse resulting in a smaller difference signal. Therefore, by optimizing the probe pulse width, maximum polarization signal can be detected.

Any timing uncertainty between the microwave frequency and bin number was assumed to be negligible, as long as the total frequency sweep time was set to be equal to the data collection time for one record of the multichannel scaler, and both were synchronized to each other.

The microwave frequency is fixed to the spin transition frequency for Rabi nutation experiments or spin echo experiments. Detailed pulse sequences for the experiments are discussed in following section.

B. Experimental Procedure and Preliminary Results

More than 100 luminescent defects have been reported in diamond[66]. Among them, Nitrogen vacancy (NV) defects are of particular interest due to their superior optical properties in terms of spin detection, and polarization. This is important for quantum computing applications. Nitrogen atoms, which are naturally present as impurities or implanted by ion-implantation, can substitute for carbon atoms. During a high temperature annealing process, they can combine with vacancies, which migrate to the neighboring sites of carbon atoms to form stable NV color centers. This is shown schematically in figure 2.8 (a), and the schematic diagram for the electronic structure of NV defects is shown in figure 2.8 (b).

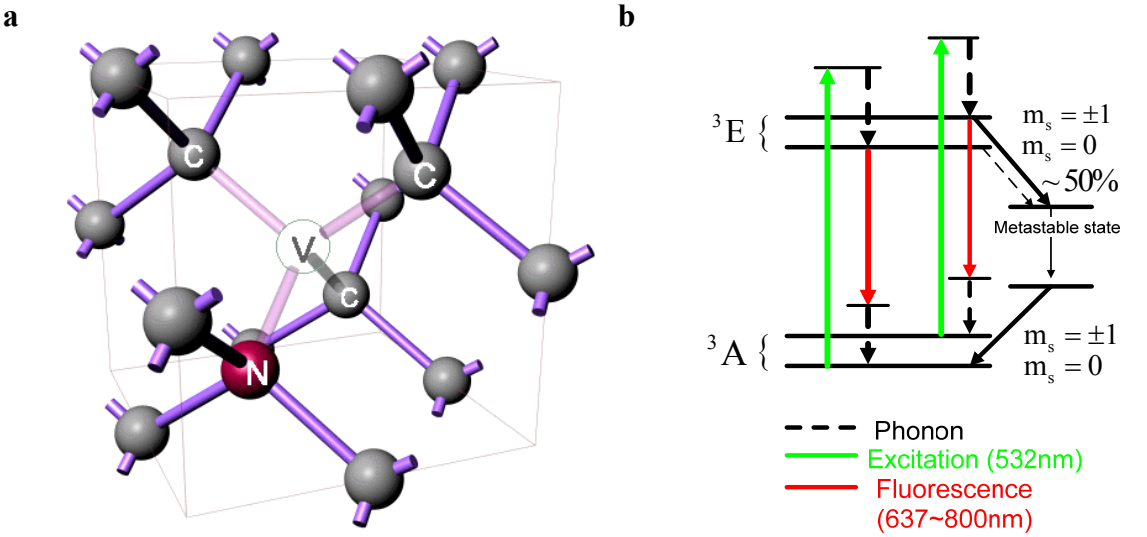

Figure 2.8 **a**, Structure of NV defects in diamond. **b**, Simplified electronic structure of NV defects in diamond.

Since NV defects have strong electric dipolar optical transitions, single NV defects can be optically detected even at room temperature. Once the NV is optically excited, it experiences spontaneous emission, with a characteristic emission spectrum having a zero phonon line at 637nm that can be detected by spectrometer.

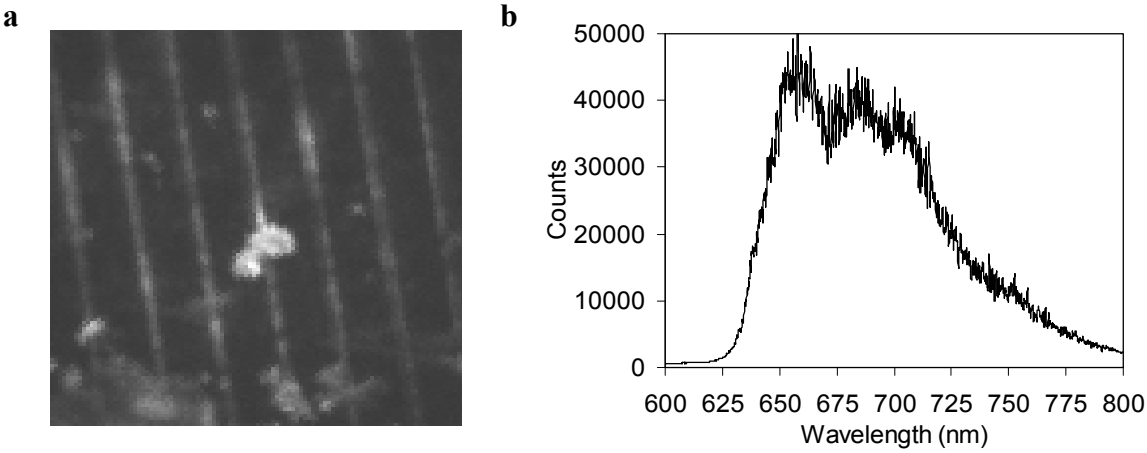

Figure 2.9 **a**, Fluorescence image of NV defects in bulk diamond. **b**, Characteristic emission spectrum of NV defects measured at room temperature. NV defects are created by ion-implantation followed by annealing process.

Though the majority of defects present in our sample are NV defects, it is always necessary to check the emission spectrum of individual defects to be sure they are NV defects. A fluorescence image of NV defects created by Ga ion-implantation followed by annealing in bulk nitrogen-doped diamond, are shown in figure 2.9 (a) and the characteristic emission spectrum of NV defects are shown in figure 2.9 (b).

1. Photon Antibunching Experiments

Since the diffraction limited spot size of the conventional fluorescent microscope is generally much larger than the size of single molecules, such as NV defects, it is possible to have 2 or more defects present within the focal volume that cannot be resolved.

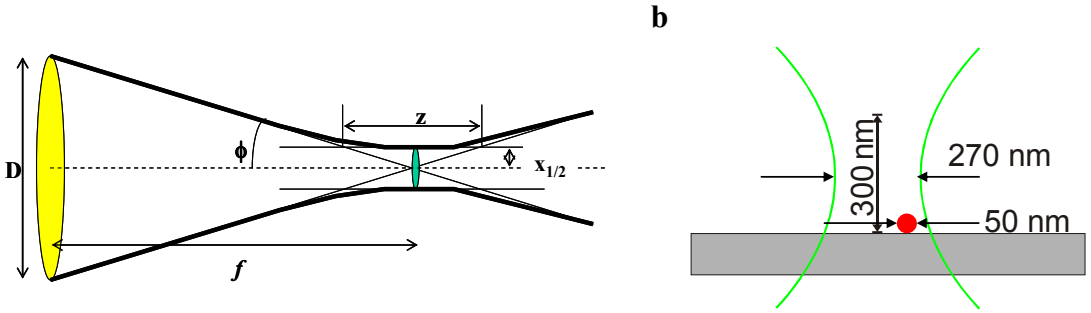

Figure 2.10 **a**, Schematic diagram for a single lens system. **b**, Schematic diagram of its cross sectional view of the focal volume of an oil immersion lens with N.A. of 1.4 and immersion oil of n_o=1.517, excitation wavelength at 532nm. A typical nano-diamond crystal is shown as red dot in the figure.

The performance of a microscope objective for a single lens system is illustrated in the schematic diagram in figure 2.10. The diffraction limited spot size can be calculated by equation (2.4), and depth of focus is defined by

$$z = 1.22 \cdot 4\lambda \left(\frac{f}{D} \right)^2 \cos\phi \qquad (2.6)$$

with $N.A. = n_o \sin\phi = n_o \left(\frac{D}{2f} \right)$.

A non-classical dipolar emitter, such as a nitrogen-vacancy (NV) defect in diamond emits one photon at a time. The reason is that when a single atom has absorbed one photon, it should return to the ground state by emitting one photon in order to absorb a second photon and then emit a second photon. Assuming that an initial emitted photon is detected at time τ=0, the photon correlation function gives the probability of a second photon detection event at time t + τ. From the shape of the correlation function, it is theoretically possible to tell if there is more than one molecule present in the focal volume. The second order autocorrelation function, $g^2(\tau)$ of the fluorescence intensity, $I(t)$ from a non-classical emitter is defined by[67, 68,69,70]

$$g^2(\tau) = \frac{\langle I(t) I(t+\tau) \rangle}{\langle I(t) \rangle^2} \qquad (2.7)$$

where $\langle I(t) I(t+\tau) \rangle = \lim_{T \to \infty} \frac{1}{T} \int_0^T I(t) I(t+\tau)\, dt$.

Due to the dead time of the detectors, which is typically of the same order as the correlation time, it is impossible to do photon correlation experiments with a single detector. In our setup, the single photon counting module (SPCM-AQR-13-FC, PerkinElmer) has dead time of 60ns, therefore if two photons arrive at the same detector within 60ns temporal distance, the second photon can not be detected by the detector.

By using the Hanbury-Brown-Twiss setup with 2 avalanche photodiodes (APD) this problem can be overcome. Schematic diagram of the Hanbury-Brown-Twiss setup is shown in figure 2.11.

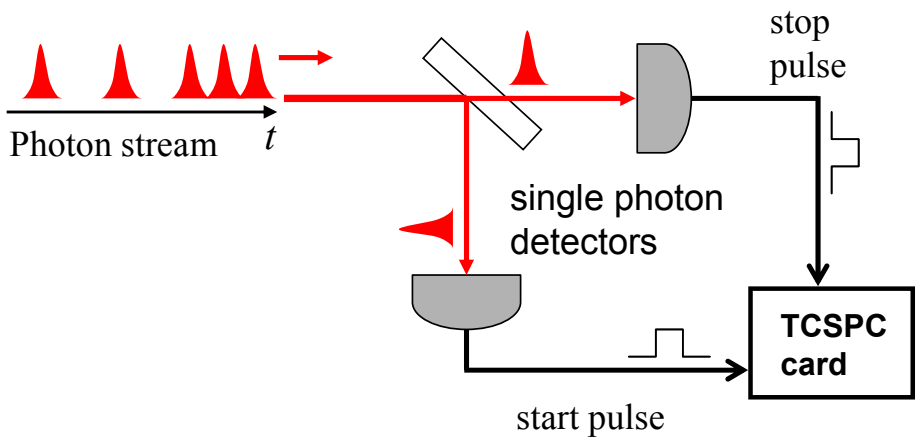

Figure 2.11 Schematic diagram of the Hanbury-Brwon-Twiss setup with 2 APDs, and time correlated single photon counting (TCSPC) card.

The second order correlation function of two detectors is defined by[71]

$$g_c^{\,2}(\tau) = \frac{\langle I_{d1}(t) I_{d2}(t+\tau) \rangle}{\langle I_{d1}(t) \rangle \langle I_{d2}(t) \rangle} \qquad (2.8)$$

where $I_{d1}(t)$, $I_{d2}(t)$ are the fluorescence intensities recorded by detector 1, and detector 2, respectively, and equation (2.8) is equivalent to the normalized autocorrelation function of the fluorescence intensity, i.e. equation (2.7) [72].

In order to derive the second order correlation function for the NV, the electronic structure was assumed to be a 3-level system as seen in figure 2.12. And the time evolution of the population is given by[73]

$$\frac{d}{dt}\begin{pmatrix}\sigma_1\\ \sigma_2\\ \sigma_3\end{pmatrix}=\begin{pmatrix}-k_{12} & k_{21} & 0\\ k_{12} & -k_{21}-k_{23} & k_{32}\\ 0 & k_{23} & -k_{32}\end{pmatrix}\begin{pmatrix}\sigma_1\\ \sigma_2\\ \sigma_3\end{pmatrix} \tag{2.9}$$

with the initial condition $\sigma_1=1$, $\sigma_2=0$, $\sigma_3=0$.

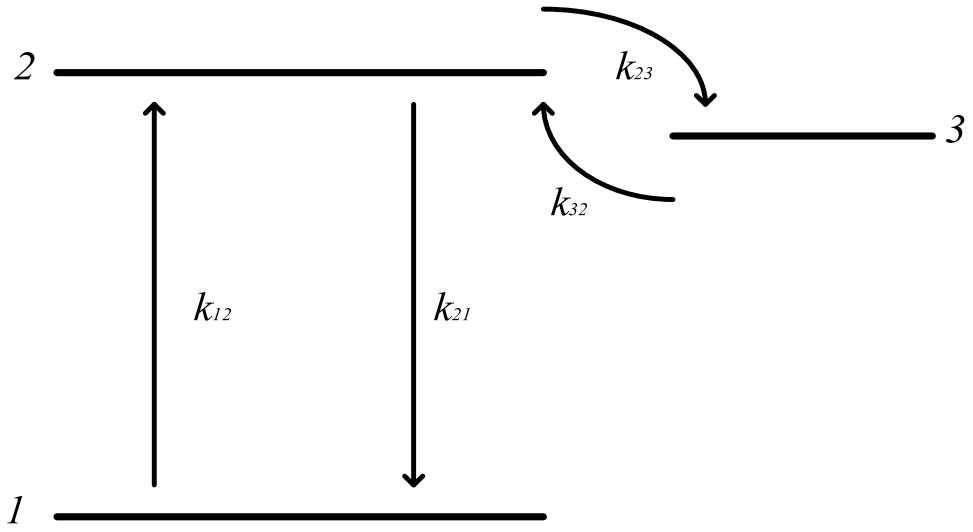

Figure 2.12 Three-level scheme for NV defects in diamond.

An analytical solution of equation (2.9) with back ground noise determined from experimental data is given by

$$g^2(\tau)=\frac{\sigma_2(\tau)}{\sigma_2(\infty)}=1+\rho-\frac{1+g_e}{2}e^{-\left(\frac{k_t+k_1}{2}\right)|\tau-\tau_d|}-\frac{1-g_e}{2}e^{-\left(\frac{k_t-k_1}{2}\right)|\tau-\tau_d|} \tag{2.10}$$

where ρ is back ground noise, τ_d is delay time corresponding to the delay line given to the stop channel, and the steady-state population of the fluorescing state is,

$$\sigma_2(\infty)=\frac{k_{12}k_{32}}{k_{12}k_{23}+k_{12}k_{32}+k_{21}k_{32}} \tag{2.11}$$

$$k_t=k_{12}+k_{21}+k_{23}+k_{32} \tag{2.12}$$

$$k_1^2 = \left(\left(k_{12} + k_{21} - k_{23} - k_{32} \right)^2 + 4k_{21}k_{23} \right) \tag{2.13}$$

$$g_e = \frac{2k_{12}k_{32} + k_{32}\left(k_{12} + k_{21} - k_{23} - k_{32} \right)}{k_1 k_{32}}. \tag{2.14}$$

Where g_e, k_t, k_1, $\sigma_2(\infty)$ and ρ are determined by fitting equation (2.10) to the normalized experimental data. Antibunching experiments on a single NV defect in bulk diamond with various optical excitation powers were performed, and the experimental data are shown in figure 2.13.

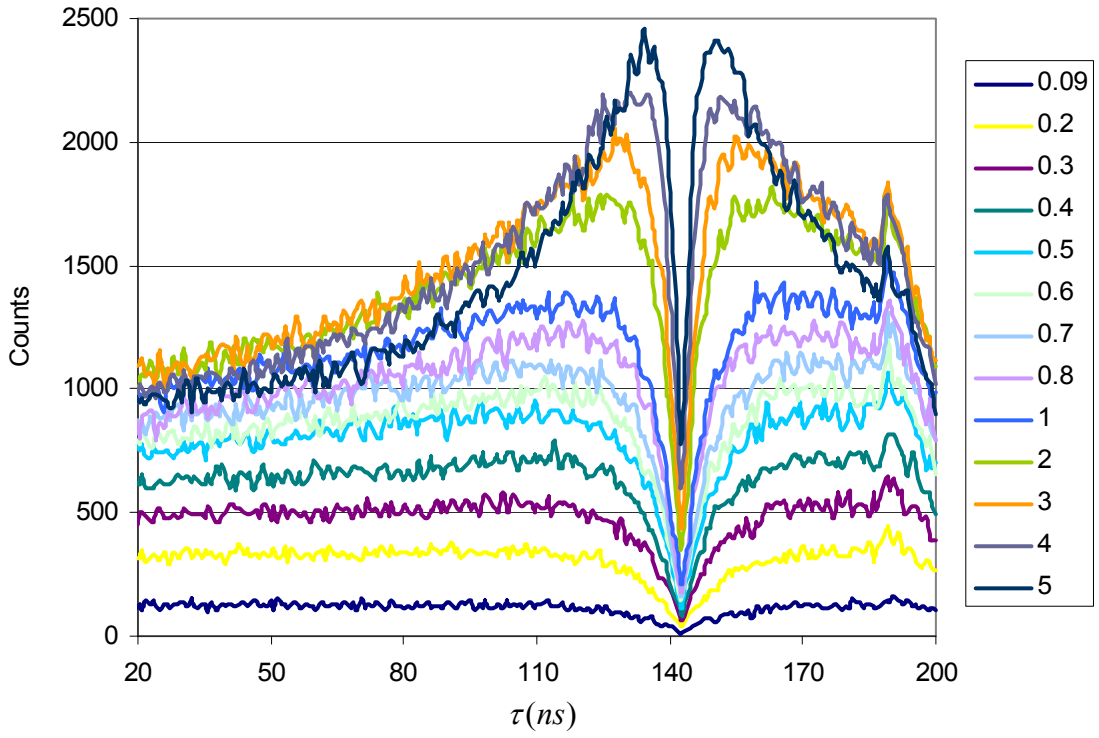

Figure 2.13 Experimental data of photon antibunching experiments on a single NV defect in bulk diamond with various optical excitation powers are plotted as a function of τ. Optical power (mW) was measured in front of the microscope objective. Timing jitter was less than 350ps.

As the optical excitation power increased, the total counts increased, and the minimum of the antibunching dip, which may be associated with background noise, also increased. Assuming that a photon was emitted from a single NV defect at $\tau = \tau_d = 142.2ns$, a probability to find the second photon is zero, which means that the minimum antibunching dip should go down to zero. But due to the background noise in the experiments, the minimum antibunching dip does not go down to zero. Figure 2.14 shows the signal vs. background noise as a function of optical excitation power. Initially, the signal increased as optical power increased, but after a saturation point, it did not increase any more, yet the noise continued to increase as optical power increased further.

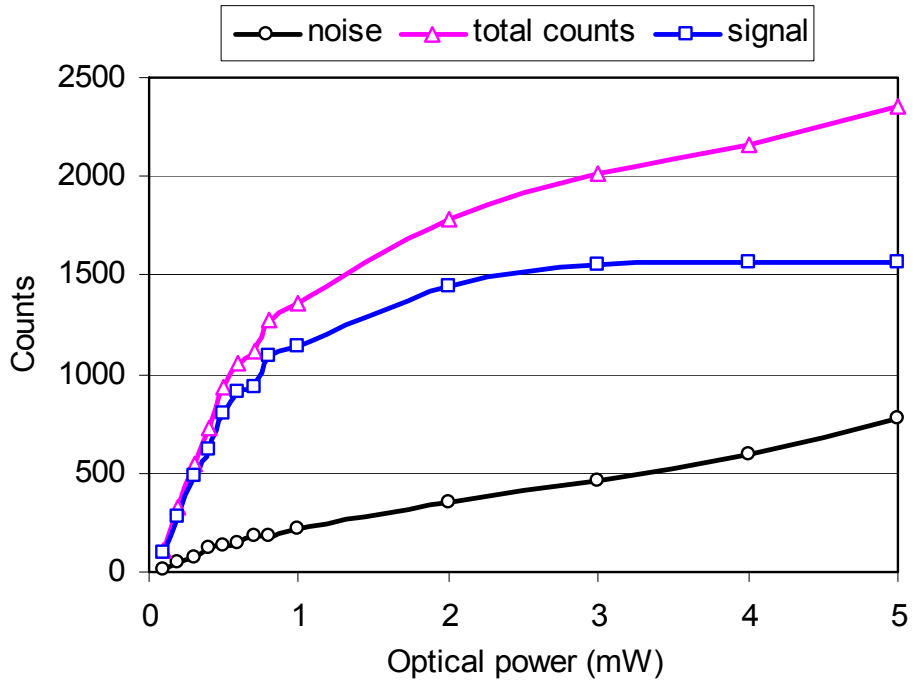

Figure 2.14 Signal vs. noise level as a function of optical excitation power. Signal counts were obtained by subtracting the noise counts from total counts.

Assuming that a single NV defect emitter is a Poissonian light source, the coincidence counts shown in figure 2.13 can be normalized as follows.

$$g_m^2(\tau) = \frac{C_N(\tau)}{r_c \cdot r_s \cdot \Delta t \cdot T} \tag{2.15}$$

where r_c is rate on the start channel, r_s is rate on the stop channel, Δt is the time width of a bin, T is total integration time, $C_N(\tau)$ is total counts in each time bin. In these experiments, Δt = 0.78125ns, and T =300s were used.

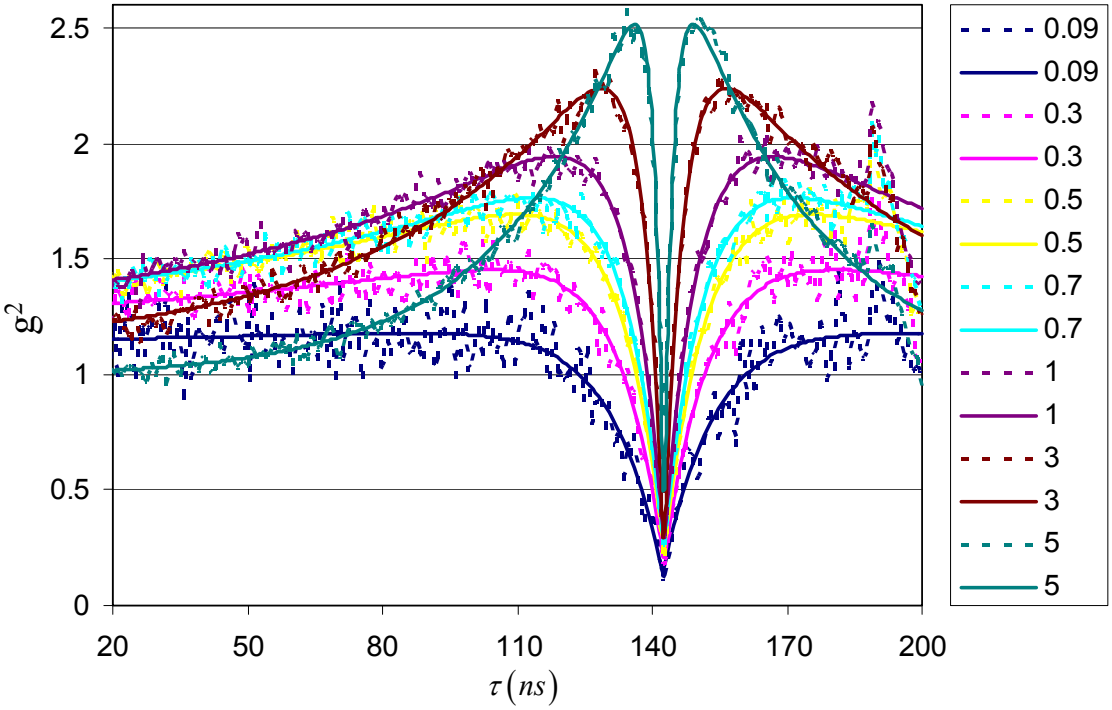

Figure 2.15 Normalized photon correlation experimental data on a single NV defect in bulk diamond. Time delay of τ_d=142.1875ns corresponds to the delay line inserted on the stop channel. For small optical power, fluorescence lifetime, τ=11.6ns was measured. Dotted lines are experimental data, and solid lines are fitted curves for 3-level system. Optical power (mW) was measured before the objective lens.

Figure 2.15 shows normalized experimental data calculated by equation (2.15) along with fitted curves using equation (2.10) with ρ, g_e, k_t, $k_{1,}$ as free parameters for various optical excitation powers. The second order photon correlation function for the 3-level system model showed good agreement with the experimental data.

For the case of multiple defects with relatively small optical excitation power, i.e. smaller than that of saturation, equation (2.10) can be simplified as follows.

$$g^2(\tau) = 1 - \frac{1}{N} e^{-|\tau - \tau_d|/\tau_1} + \rho \qquad (2.16)$$

Where τ_d is time delay, τ_1 is photon life time, N is the number of NV defects irradiated in the focal volume, ρ is background noise. Figure 2.16 shows the photon correlation experimental data on a single NV defect and 2 NV defects with fitted curves from equation (2.16). Antibunching dips of $g^2(\tau)$ have minima of 0.11, and 0.57 for a single NV defect, and for 2 NV defects, respectively. If several NV defects are present in the focal volume, number of NV defects are being irradiated in the volume can be estimated by the equation (2.16), as long as the background noise is small enough.

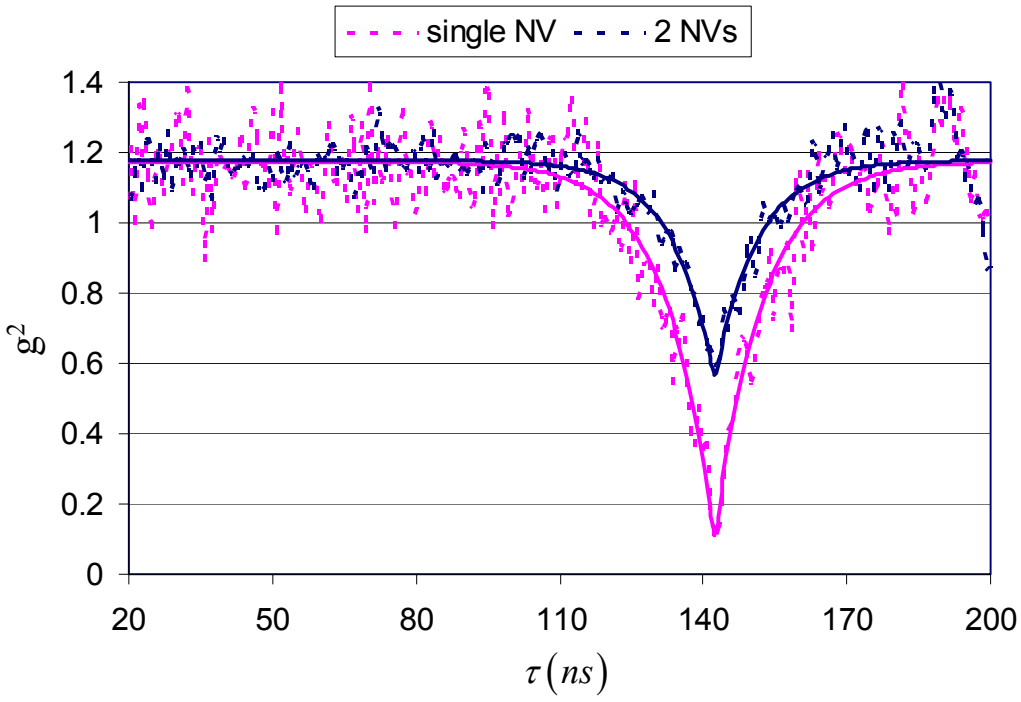

Figure 2.16 Second order photon correlation function on a single NV defect, and 2 NV defects, with optical power of 90μW, and 220μW, respectively. Dotted lines are experimental data, and solid lines for fitted curves.

In the electron spin resonance (ESR) experiments, a statistical error is square root of the total fluorescence counts, and the time-averaged maximum ESR signal is about 30 percent of the total fluorescence counts. As a result, the more counts we have, the higher signal to noise ratio we get. Higher optical excitation power generates more signal photons, but at the same time background noise increases, and the faster spin polarization rate to the m_s=0 state occur. Therefore, in order to detect a pure m_s=-1or m_s=+1 spin state, too much optical excitation power should be avoided. Yet, if the optical power is too small, the total data acquisition time needed to get a reasonable signal to noise ratio would be too long. Typically for these experiments, the total

number of sweeps for an ESR experiment is about 300,000 with a sweep rate of about 300Hz, so that the total data acquisition time is about 1000s.

By doing antibunching experiments, the saturation behavior of the NV defects with respect to a given optical power can be monitored, and thereby proper optical power can be determined for the most efficient data acquisition.

2. Background Theory and Preliminary Experiments for CW ESR

The total energy operator of the quantum states can be expressed as

$$\mathbf{H}\Psi = E\Psi \tag{2.17}$$

where **H** is the Hamiltonian for the total energy of the quantum system, and Ψ is the quantum states of the system, which is a vector in this case, i.e. $\Psi = \sum_{S_z=-1}^{1} c_{S_z} \left| S_z \right\rangle$. Eigenvalues ($E$) of the spin Hamiltonian (**H**) indicate the allowed energy levels for the quantum states, and the strength of transition between quantum states can be calculated by using eigenvalues and eigenstates.

Interactions of the ground state electron spins of NV defects with neighboring ^{14}N nuclear spins, and/or an external magnetic field are described by the spin Hamiltonian as follows:[74, 75, 76, 77]

$$\mathbf{H} = D\left(S_z^2 - \frac{1}{3}S^2 \right) + g_e\beta_e \mathbf{BS} + \mathbf{S}A\mathbf{I} - g_n\beta_n \mathbf{BI} + P\left(I_z^2 - \frac{1}{3}I^2 \right) \tag{2.18}$$

where D=2.87GHz is the zero field splitting, **B** is the external magnetic field, **S** is the electron spin vector, **I** is the nuclear spin vector, A is the hyper fine coupling tensor with $A_\perp$=2.1MHz, $A_\parallel$=2.3MHz**,** P = -5.04 MHz is quadrupole coupling of the nitrogen

nuclear spins, $g_e\beta_e$ =2.8MHz/Gauss and $g_n\beta_n$ =0.307KHz/Gauss. The zero field splitting (*D*) causes a splitting of ground triplet states into a singlet, m_s=0, and a degenerate doublet, m_s=+/-1 in the absence of an external magnetic field. This is a consequence of the molecular structure, and it has profound effects on magnetic properties of the NV molecules[78].

In NV defects, hyperfine coupling between the electron and nuclear spins, nuclear Zeeman splitting, and nuclear quadrupole coupling are all small compared to the zero field electron spin splitting, and the electron Zeeman splitting. Therefore, they can be easily masked by ESR line broadening caused by a large optical excitation power, and/or microwave power. In this case, the spin Hamiltonian can be simplified as;

$$\mathbf{H} = D\left(S_z^2 - \frac{\left(\sqrt{S(S+1)}\right)^2}{3} \right) + g_e\beta_e \mathbf{BS} \tag{2.19}$$

By applying an external magnetic field, the otherwise degenerate ground electron spin states, m_s=+/-1 are split, and they can be resolved.

Using $\mathbf{B} = \hat{x}B_x + \hat{y}B_y + \hat{z}B_z$, $\mathbf{S} = \hat{x}S_x + \hat{y}S_y + \hat{z}S_z$ and total electron spin S =1, Hamiltonian of the electron spins of the NV defects can be re-written as,

$$\mathbf{H} = D\left(S_z^2 - \frac{2}{3} \right) + g_e\beta_e \left(B_x S_x + B_y S_y + B_z S_z \right) \tag{2.20}$$

where *D*=2.87GHz and $g_e\beta_e$ =2.8MHz/Gauss. By definition, the x and y components of electron spin can be expressed as

$$S_x = \frac{\left(S_+ + S_-\right)}{2} \tag{2.21}$$

$$S_y = \frac{\left(S_+ - S_-\right)}{2i} \tag{2.22}$$

Where the raising operator and lowering operators are defined, respectively, by

$$S_+ \left|S_z\right\rangle = \sqrt{\left(S + S_z + 1\right)\left(S - S_z\right)}\left|S_z + 1\right\rangle \tag{2.23}$$

$$S_- \left|S_z\right\rangle = \sqrt{\left(S + S_z\right)\left(S - S_z + 1\right)}\left|S_z - 1\right\rangle \tag{2.24}$$

Since $\Psi = \sum_{S_z=-1}^{1} c_{S_z}\left|\psi_{S_z}\right\rangle$ where $\left\{\left|\psi_{-1}\right\rangle,\left|\psi_0\right\rangle,\left|\psi_{+1}\right\rangle\right\} = \left\{\left|m_s = -1\right\rangle,\left|m_s = 0\right\rangle,\left|m_s = +1\right\rangle\right\}$ for the electron spin states of the NV defects in diamond, equation (2.17) will be written as

$$\mathbf{H}\Psi = D\begin{pmatrix} 1/3 & 0 & 0 \\ 0 & -2/3 & 0 \\ 0 & 0 & 1/3 \end{pmatrix}\begin{pmatrix} \left|\psi_{-1}\right\rangle \\ \left|\psi_0\right\rangle \\ \left|\psi_{+1}\right\rangle \end{pmatrix} + g_e\beta_e\begin{pmatrix} -B_z & \frac{B_x - iB_y}{\sqrt{2}} & 0 \\ \frac{B_x + iB_y}{\sqrt{2}} & 0 & \frac{B_x - iB_y}{\sqrt{2}} \\ 0 & \frac{B_x + iB_y}{\sqrt{2}} & B_z \end{pmatrix}\begin{pmatrix} \left|\psi_{-1}\right\rangle \\ \left|\psi_0\right\rangle \\ \left|\psi_{+1}\right\rangle \end{pmatrix} \tag{2.25}$$

The external magnetic field can be expressed as

$$\mathbf{B} = \hat{x}B_0\sin\theta\cos\phi + \hat{y}B_0\sin\theta\sin\phi + \hat{z}B_0\cos\theta \tag{2.26}$$

where θ is the angle of the field from the NV quantized axis. Due to the C_{3v} symmetry of the NV defects in diamond, we can assume that ϕ=0.

Then the spin Hamiltonian can be written as

$$\mathbf{H} = \begin{pmatrix} \frac{D}{3} - g_e\beta_e B_0\cos\theta & g_e\beta_e\frac{B_0\sin\theta}{\sqrt{2}} & 0 \\ g_e\beta_e\frac{B_0\sin\theta}{\sqrt{2}} & -\frac{2D}{3} & g_e\beta_e\frac{B_0\sin\theta}{\sqrt{2}} \\ 0 & g_e\beta_e\frac{B_0\sin\theta}{\sqrt{2}} & \frac{D}{3} + g_e\beta_e B_0\cos\theta \end{pmatrix} \tag{2.27}$$

By numerically solving the above Hamiltonian as a function of external magnetic field strength at a given angle with respect to the [111] crystal direction, we can find the dependence of energy sub-levels of the ground electron spin states upon magnetic field strength as shown in figure 2.17.

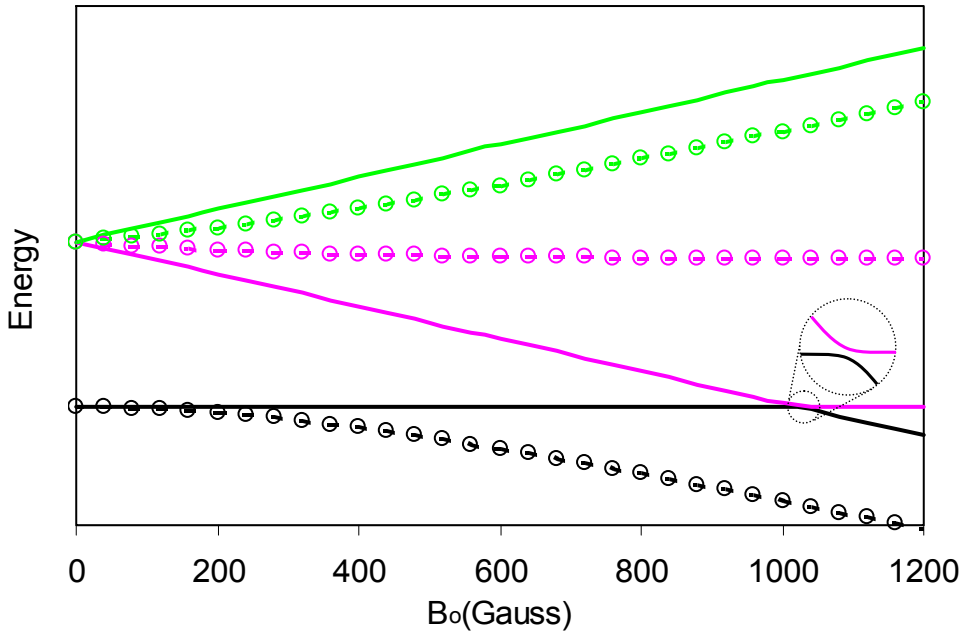

Figure 2.17 Magnetic field dependency of energy sub levels of ground electron spins of NV defects. Green lines are for m_s=+1 state, pink lines for m_s=-1 state, and black lines for m_s=0 state, and solid lines for the case when external magnetic field is parallel to NV quantization axis, and dotted lines with circle for the NV defects oriented at an angle of 109.4 degrees.

When the external magnetic field is parallel to the quantization axis of the electron spins, i.e. [111] direction, the electron Zeeman splitting depends linearly on the magnetic field strength. At about 1030Gauss of magnetic field along the NV quantization axis, a level anti-crossing (LAC) occurs between m_s=-1, and m_s=0 state. In this configuration, the other 3 NV defects are magnetically equivalent oriented at an

angle of 109.4 degrees from the external magnetic field, and these magnetically equivalent NV defects show quadratic dependence on the external magnetic field.

The Fluorescence intensity of NV defects has a strong dependency upon the electron spin states, i.e. optically excited electrons with spin state of m_s=+/-1 go into the metastable state with a probability of 50%, and this metastable state has about 20 times longer lifetime than that of the fluorescence state. Electrons in the metastable state eventually decay almost exclusively to the ground state, i.e. m_s=0 state via non-radiative decay. As a result, the time averaged fluorescence intensity will decrease up to 30% when the electron spins are in m_s=+/-1 state, thereby the electron spin states can be optically detected. Since photon collection efficiency is generally less than a few percent, fluorescence signals are generally averaged over 100,000 to 1000,000 times.

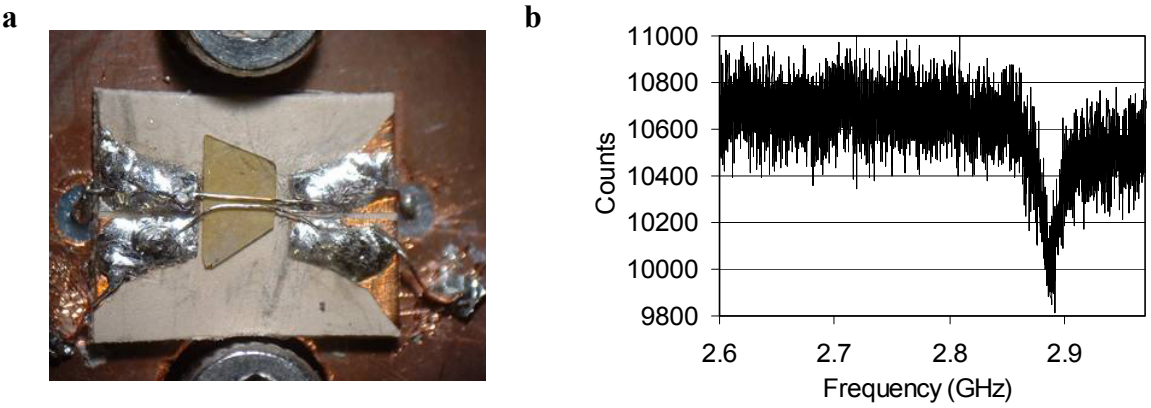

Figure 2.18 **a**, Bulk diamond was mounted on the microwave substrate, and a pair of 50μm bonding wires are used as microwave transmission lines. **b**, CW ESR signal of NV defects in bulk diamond in the absence of external magnetic field was detected.

For preliminary experiments, a bulk diamond sample was mounted on the substrate holder as shown in figure 2.18 (a), and continuous wave electron spin

resonance (CW ESR) signal was detected in the absence of external magnetic field as seen in figure 2.18 (b). In this experiment, the defects were continuously irradiated by optical excitation and the frequency of microwave signal was swept as schematically shown in figure 2.19 (b). At around 2.87GHz, the fluorescence counts dropped by about 6%, due to the mixing of electron spin ground states caused by irradiation with a resonant microwave signal.

By increasing the microwave power, ESR line broadening was observed as seen in figure 2.19 (a). The side lobe for the large microwave power case is also attributed to the power broadening effect. When large microwave power is applied, a slightly off-resonance microwave signal can induce transitions between spin states. In order to get a narrow ESR line with a higher signal contrast, the experimental procedures should be modified, and this will be discussed in the following section.

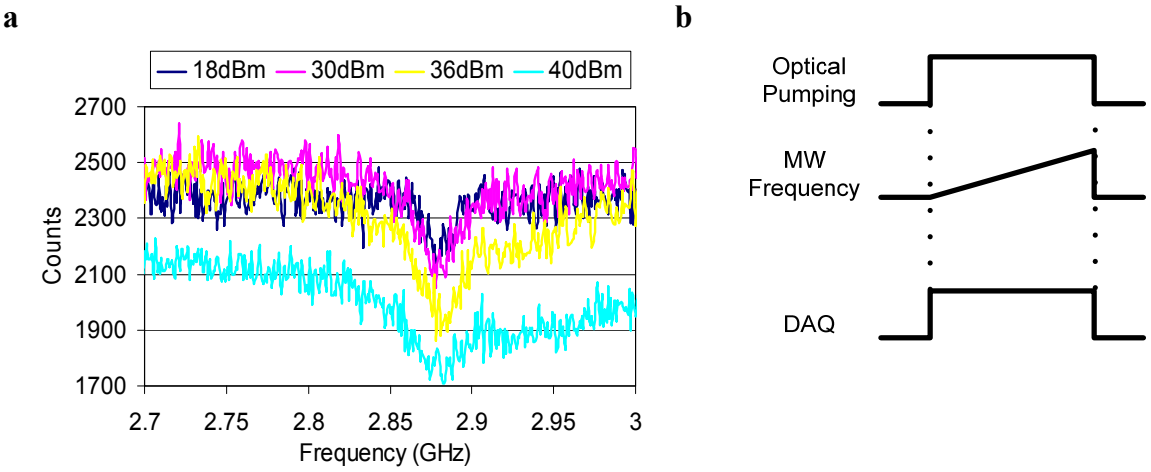

Figure 2.19 **a**, CW ESR experiments with larger microwave power. **b**, Experimental procedure.

When a microwave signal in resonance with the ESR transition frequency is applied, the electron spins coherently interact with the microwave signal, so the probability to find the system in the m_s=0 or m_s=+/-1 states will be periodically modulated. In consequence, the fluorescence intensity is periodically modulated in time with the oscillation frequency that depends on the microwave power.

These Rabi oscillations or nutations of electron spins of NV defects were observed as shown in figure 2.20 (a) with (b) showing a schematic diagram of experimental procedure.

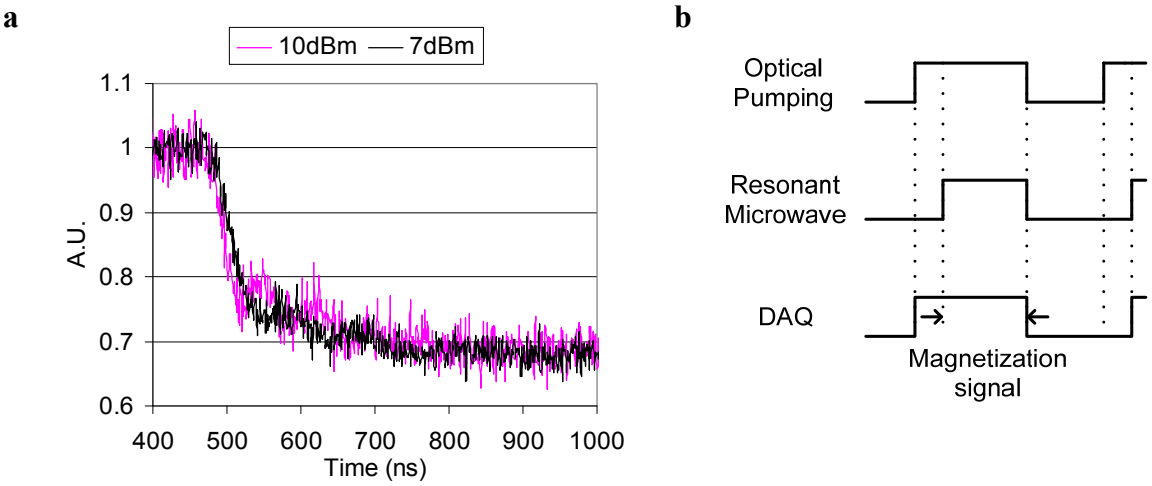

Figure 2.20 **a**, Rabi nutations of electron spin states of NV defects upon irradiation of resonant microwave signal is plotted. **b**, Schematic diagram of experimental procedure.

Upon irradiation with a resonant microwave signal, the fluorescent intensity decreased by up to 30%, which indicates that the time-averaged maximum modulation of the fluorescence signal can be up to 30%. While resonant MW signal is being applied, the electron spins are coherently trapped between m_s=0 and m_s=+/-1 states, so less m_s=0

population is excited by optical excitation laser, which results in a fluorescence signal decrease by 30%.

The Rabi oscillation frequency depends quadratically on the microwave power, i.e. the Rabi frequency increases twice as the microwave power increases four times. The larger the applied microwave power, the faster the Rabi oscillations.

It was reported that optical excitation power affects the Rabi nutation frequency, and the population is re-distributed by the continuous optical excitation during the microwave irradiation. Therefore, it is required to turn off the optical excitation while the microwave signal is being applied in order to remove spin re-distribution caused by optical pumping. Instead, once the electron spins are manipulated by the resonant microwave signal, a short optical probe pulse can be applied for detection of the spin states, after the microwave signal is turned off. In this way, most of the electron spin population will be modulated by the resonant microwave pulse, and resultant spins will be efficiently probed by the optical probe pulse without being affected by the resonant microwave signal. Therefore, pulse mode experiments are necessary, which will be discussed in section 4.

3. Background Theory for Rabi Nutation Experiments and Spin Echo Experiments

Electron spin echo or electron spin Rabi nutation of a NV defect are associated with two electron spin levels, e.g. m_s=0 and m_s=+1 state or m_s=0 and m_s=-1 states.

Therefore, we consider a two-level atomic quantum system, i.e. $|1\rangle$, $|2\rangle$ with a atomic energy $\hat{H}_A$ of $\langle 1|\hat{H}_A|1\rangle = 0$, and $\langle 2|\hat{H}_A|2\rangle = \frac{h}{2\pi}\omega_o$.

Any pure state can be represented by a linear superposition of the two states,

$$|\psi\rangle = c_1|1\rangle + c_2|2\rangle \tag{2.28}$$

with $|c_1|^2 + |c_2|^2 = 1$.

In general, any state of the system can be represented by an atomic density operator[79],

$$\hat{\rho} = \rho_{11}|1\rangle\langle 1| + \rho_{12}|1\rangle\langle 2| + \rho_{21}|2\rangle\langle 1| + \rho_{22}|2\rangle\langle 2| \tag{2.29}$$

where $\rho_{ij} = \langle c_i c_j^* \rangle$, i, j= 1, 2.

The time evolution of the atomic density operator in the Schrödinger picture is governed by the Liouville equation,

$$\frac{\partial\hat{\rho}(t)}{\partial t} = -\frac{i}{(h/2\pi)}\left[\left(\hat{H}_A + \hat{H}_I\right), \hat{\rho}(t)\right] \tag{2.30}$$

where the interaction energy $\hat{H}_I$ is defined by $\hat{H}_I = -\hat{\mu}(t) \bullet \mathbf{E}(t)$, and $\hat{\mu}(t)$ is dipole moment of the atom and $E(t)$ is the electric field. Then, we obtain the following equations,

$$\begin{aligned}
\frac{\partial \rho_{11}}{\partial t} &= \frac{1}{i(h/2\pi)}\left[\langle 1|\hat{H}_I|2\rangle \rho_{21} - c.c.\right] \\
\frac{\partial \rho_{22}}{\partial t} &= -\frac{1}{i(h/2\pi)}\left[\langle 1|\hat{H}_I|2\rangle \rho_{21} - c.c.\right] \\
\frac{\partial \rho_{12}}{\partial t} &= \frac{1}{i(h/2\pi)}\left[-(h/2\pi)\omega_o \rho_{12} + \langle 1|\hat{H}_I|2\rangle(\rho_{22} - \rho_{11})\right] \\
\frac{\partial \rho_{21}}{\partial t} &= \frac{1}{i(h/2\pi)}\left[(h/2\pi)\omega_o \rho_{21} + \langle 2|\hat{H}_I|1\rangle(\rho_{11} - \rho_{22})\right]
\end{aligned} \tag{2.31}$$

It can be simply represented by a three-dimensional vector **r** with components of r_1 , r_2 and r_3 , which is known as the Bloch-representation. The Bloch-vector components, which is representing the state in the Schrödinger picture are defined by

$$\begin{aligned}
r_1 &= 2\,\mathrm{Re}(\rho_{12}) \\
r_2 &= 2\,\mathrm{Im}(\rho_{12}) \\
r_3 &= \rho_{22} - \rho_{11}
\end{aligned} \tag{2.32}$$

with $r_o = \rho_{11} + \rho_{22}$.

By using the equation (2.31), and (2.32), three components of the Bloch-vector **r** can be re-written as,

$$\begin{aligned}
\frac{\partial r_1}{\partial t} &= \frac{2}{(h/2\pi)}\mathrm{Im}\left[\langle 1|\hat{H}_I|2\rangle\right] r_3 - \omega_o r_2 \\
\frac{\partial r_2}{\partial t} &= -\frac{2}{(h/2\pi)}\mathrm{Re}\left[\langle 1|\hat{H}_I|2\rangle\right] r_3 + \omega_o r_1 \\
\frac{\partial r_3}{\partial t} &= -\frac{2}{(h/2\pi)}\mathrm{Im}\left[\langle 1|\hat{H}_I|2\rangle\right] r_1 + \frac{2}{(h/2\pi)}\mathrm{Re}\left[\langle 1|\hat{H}_I|2\rangle\right] r_2
\end{aligned} \tag{2.33}$$

This is known as the Bloch equations, which describes the time evolution of the atom in the presence of the interaction $\hat{H}_I$.

Suppose a time-varying electric field at a frequency of ω_1, $\mathbf{E}(t) = \hat{\varepsilon} E(t) e^{-i\omega_1 t} + c.c.$, interacts with the atom, then matrix element $\langle 1 | \hat{H}_I | 2 \rangle$ can be written as,

$$\begin{aligned} \langle 1 | \hat{H}_I | 2 \rangle &= -\mu_{12} \bullet \mathbf{E}(t) \\ &= -|E(t)| \mu_{12} \bullet \left[\hat{\varepsilon} e^{-i\omega_1 t} + c.c. \right] \end{aligned} \tag{2.34}$$

where $\hat{\varepsilon}$ is the unit polarization vector.

If we deal with an atomic $\Delta m = \pm 1$ transition, the dipole moment can be set $\mu_{12} = |\mu_{12}| (\hat{x} + i\hat{y}) / \sqrt{2}$, and if the external electric field is circularly polarized and propagating in the z-direction, polarization vector is expressed as $\hat{\varepsilon} = (\hat{x} + i\hat{y}) / \sqrt{2}$. After substituting (2.34) in (2.33), the Bloch equation can be re-written as

$$\begin{aligned} \frac{\partial r_1}{\partial t} &= -\Omega(t) r_3 Sin(\omega_1 t) - \omega_o r_2 \\ \frac{\partial r_2}{\partial t} &= \Omega(t) r_3 Cos(\omega_1 t) + \omega_o r_1 \\ \frac{\partial r_3}{\partial t} &= \Omega(t) r_1 Sin(\omega_1 t) - \Omega(t) r_2 Cos(\omega_1 t) \end{aligned} \tag{2.35}$$

where Rabi nutation frequency, $\Omega(t) \equiv 2\mu_{12} \bullet \hat{\varepsilon}^* |E(t)| / (h/2\pi)$. Equations (2.35) are known as the Bloch equation in the stationary frame.

If the frame rotates at the frequency ω_1, the Bloch equations can be written as

$$\begin{aligned} \frac{\partial r_1'}{\partial t} &= -(\omega_o - \omega_1) r_2' \\ \frac{\partial r_2'}{\partial t} &= (\omega_o - \omega_1) r_1' + \Omega r_3' \\ \frac{\partial r_3'}{\partial t} &= -\Omega r_2' \end{aligned} \tag{2.36}$$

The analytical solution can be obtained as,

$$
\begin{aligned}
r_1^{'} &= \frac{1}{\Omega^2+\Delta\omega^2}\left\{\begin{array}{c}\Omega\left(\Omega\cdot r_{1o}-\Delta\omega\cdot r_{3o}\right)+\Delta\omega\left(\Delta\omega\cdot r_{1o}+\Omega\cdot r_{3o}\right)Cos\left[\left(\sqrt{\Omega^2+\Delta\omega^2}\right)t\right]\\ -\Delta\omega\cdot\sqrt{\Omega^2+\Delta\omega^2}\cdot r_{2o}Sin\left[\left(\sqrt{\Omega^2+\Delta\omega^2}\right)t\right]\end{array}\right\}\\
r_2^{'} &= \frac{1}{\Omega^2+\Delta\omega^2}\left\{\begin{array}{c}r_{2o}\cdot\left(\Omega^2+\Delta\omega^2\right)Cos\left[\left(\sqrt{\Omega^2+\Delta\omega^2}\right)t\right]\\ +\left(\Delta\omega\cdot r_{1o}+\Omega\cdot r_{3o}\right)\sqrt{\Omega^2+\Delta\omega^2}\,Sin\left[\left(\sqrt{\Omega^2+\Delta\omega^2}\right)t\right]\end{array}\right\}\\
r_3^{'} &= \frac{1}{\Omega^2+\Delta\omega^2}\left\{\begin{array}{c}\Delta\omega\left(\Delta\omega\cdot r_{3o}-\Omega\cdot r_{1o}\right)+\Omega\left(\Delta\omega\cdot r_{1o}+\Omega\cdot r_{3o}\right)Cos\left[\left(\sqrt{\Omega^2+\Delta\omega^2}\right)t\right]\\ -\Omega\cdot\sqrt{\Omega^2+\Delta\omega^2}\cdot r_{2o}Sin\left[\left(\sqrt{\Omega^2+\Delta\omega^2}\right)t\right]\end{array}\right\}
\end{aligned}
\tag{2.37}
$$

where the initial conditions are $r_1^{'}(t)=r_{1o}$, $r_2^{'}(t)=r_{2o}$ and $r_3^{'}(t)=r_{3o}$, and detuning $\Delta\omega=\omega_o-\omega_1$. Using the equations (2.37) with the equation (2.32), time evolution of the density matrix in the rotating frame can be calculated.

In the experiments with NV defects in diamond, electron spin states are optically detected by applying an optical pumping power, and the fluorescence signal represents the population difference between m_s=0 and m_s=+1 states or between m_s=0 and m_s=-1 states, i.e. $s(t)=\rho_{11}-\rho_{22}=-r_3^{'}$. Therefore, the equation (2.37) can be used to simulate experiments, if we define the variables properly with initial conditions according to the experimental conditions. Note that for spin systems, the Rabi frequency comes from interaction with the magnetic field instead of the electric field and equation (2.37) must first be so modified.

4. Pulse Mode Experiments

As examined in the section 2, continuous wave ESR experiments are not efficient in terms of spin manipulation and detection. In this section, modified experimental procedures are discussed.

4.1. Modified ESR Experiments for CW ESR Experiments

In order to avoid electron spin re-distribution by the optical excitation pulse, and to achieve higher signal contrast between spin states, the experimental procedure for CW ESR experiments was modified as schematically shown in figure 2.21. In order to sweep the microwave frequency of the voltage controlled oscillator (VCO), a home-built ramp generator circuit was used to convert each trigger signal into a ramp signal (0~10Volts).

While the frequency of the microwave signal is swept from a start frequency to a stop frequency, it is also modulated by pulse sequences with pre-determined pulse width, i.e. a microwave π-pulse. Therefore, the output of the microwave signal will be train of pulses with different center frequency, which is swept across the sweep range, i.e. from a start frequency to a stop frequency during the trigger signal.

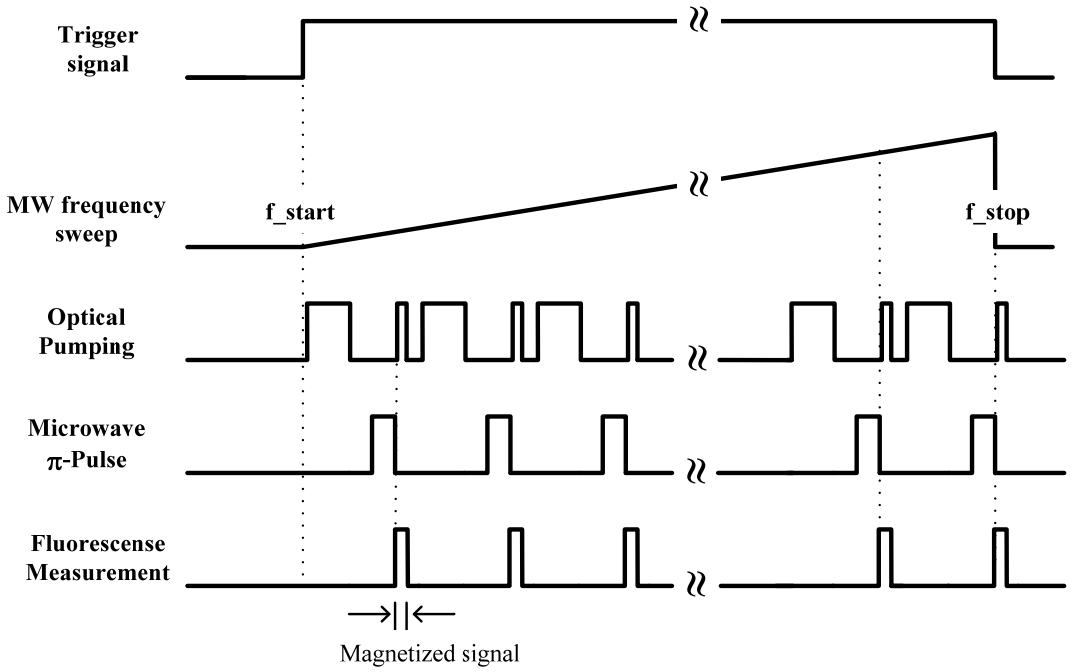

Figure 2.21 Schematic diagram of pulse mode ESR experiment.

In this configuration, the optical excitation pulses consist of a pair with a wide preparation pulse (typically 2-3μs) and a short probe pulse (typically 300ns). Once the electron spin states are prepared to m_s=0 state by the preparation pulse, they are brought into m_s=-1 or +1 state by the resonant microwave π-pulse in the absence of optical excitation, and then the final electron spin states are probed by the short probe pulse.

Since NV defects have a high polarization rate to the m_s=0 state upon optical excitation, the wide optical preparation pulse completely polarizes the electron spins into m_s=0 state. After the optical preparation pulse, a relaxation time of 1μs was given so that any optically excited electron spins, or any electron spins in the meta-stable states are relaxed to ground state via fluorescence decay, or non-radiative decay, respectively.

Electron spins, which are initialized to m_s=0 states by the optical excitation pulse, will be coherently manipulated by the microwave π-pulse, if the frequency of the microwave pulse is in resonance with the ESR transition frequency. Otherwise they remain in m_s=0 states.

Once the exact ESR transition frequency at a given external magnetic field strength was identified by the CW ESR experiments, Rabi nutation experiments with a resonant microwave frequency at a given microwave power should be performed in order to determine the pulse width for the microwave π-pulse. Detailed experimental procedures will be discussed in the following section.

A microwave π-pulse is the minimum microwave pulse duration at a given power that can completely flip the electron spin state from m_s=0 to m_s=+/-1 or visa versa. Therefore, electron spins, which are initialized to m_s=0 by the optical excitation pulse, will be flipped into m_s=+/-1 states by the subsequent microwave π-pulse, when the frequency of the microwave π-pulse is in resonance with ESR transition frequency.

Pulse mode ESR experiments on 2 NV defects were carried out according to the modified ESR experimental procedures with a microwave π-pulse of 110ns at 3dBm, and the experimental data is shown in figure 2.22.

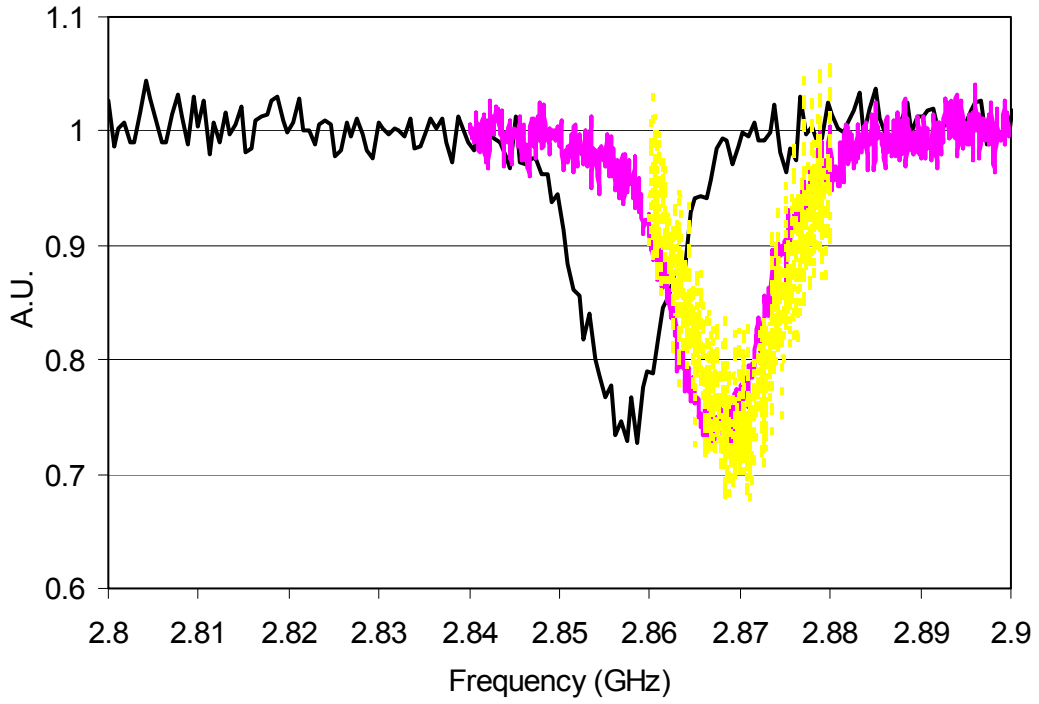

Figure 2.22 Experimental data of pulse mode ESR experiment on 2 NV defects in the absence of external magnetic field is plotted. A microwave π-pulse of 110ns was used in these experiments. Detected ESR frequency was changed while full sweep range was adjusted. Black lines are for the sweep range of 300MHz, pink for 60MHz, and yellow for 20MHz.

The signal contrast between electron spin states was increased to 26% of the total counts, which is more than 4 times larger than that shown in figure 2.18 (b). A remaining spin polarization of 4% was detected by the next optical preparation pulse, which followed the short optical probe pulse.

In this plot, ESR frequencies were observed to be 2.858GHz, 2.867GHz, and 2.87GHz with a full sweep range of 300MHz, 60MHz, and 20MHz, respectively. The ESR transition frequency of NV defects with zero magnetic fields was reported to be 2.87GHz at room temperature. The observed shift in ESR transition frequencies with a

wider sweep range were due to errors (~ 5%) due to the non-linearity of the sweep frequency of the VCO (voltage controlled oscillator) caused by the non-linearity of the ramp signal. As the range of the sweep frequency decreased, the observed ESR transition frequency matched better to what it was supposed to be, i.e. 2.87GHz. Therefore, when exact ESR transition frequency is required to know, a smaller frequency sweep range is preferred, i.e. less than 60MHz.

Since the electron spins are manipulated in the absence of optical pumping, ESR line broadening due to the optical Rabi nutations was avoided in this experiment. But any other broadening due to the large microwave power, broad bandwidth of the microwave π-pulse, and the properties of the NV molecules still remains. If a longer microwave π-pulse is employed, the microwave power requirement decreases, and broadening due to large microwave power and broad pulse bandwidth can also be avoided. Therefore, narrower ESR line can be obtained.

If microwave power is further reduced, electron spin transition lines become narrower than the nuclear spin splitting, so that hyperfine structure of the NV defect can be resolved as shown in figure 2.23. In this plot, hyperfine structures are from the interactions of electron spins with nitrogen nuclear spins. In this experiment, a much smaller microwave input power of -15dBm with corresponding π-pulse width of about 1μs was applied. Each transition line width was about 1.5~2.4MHz, and splitting between lines is about 2.3MHz, which well agrees with the hyperfine coupling coefficient i.e. $A_{\|}$=2.3MHz. Due to the splitting of the hyperfine structures, signal contrast generally decreases. In order to achieve higher signal contrast in the ESR

experiments, relatively larger microwave power will be used in the rest of the experiments.

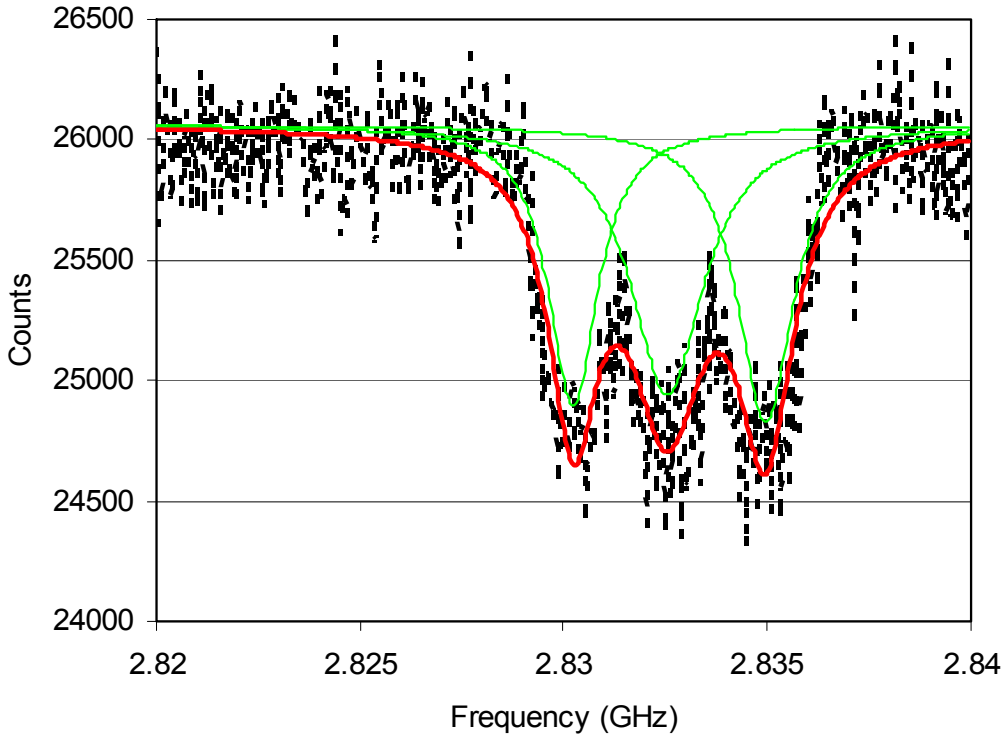

Figure 2.23 Hyperfine structures of NV defect center in diamond is plotted. MW input power was -15dBm with corresponding π-pulse width of about 1μs. Bo field of ~18Gauss was applied in order to split between m_s=-1 and m_s=+1 states. Splitting was about 2.3MHz. Solid lines are from curve fitting using 3 lorentzians model.

4.2. Modified Rabi Nutation Experiments

As previously mentioned, a resonant microwave signal at the ESR transition frequency coherently interacts with electron spins, so the probability to find the system in the m_s=0 or m_s=+/-1 states will be periodically modulated. Suppose electron spins of NV defects are in ground state, i.e. m_s=0 state. Then $\rho_{11} = 1$, and $\rho_{22} = \rho_{12} = \rho_{21} = 0$, and corresponding initial conditions will be $r_{1o} = 0$, $r_{2o} = 0$ and $r_{3o} = -1$. From the

equation (2.37) with these initial conditions, probability difference between the m_s=0 vs. the m_s=+/-1 states can be expressed as,

$$s(t) = -r_3^{'}(t) = \frac{1}{\Omega^2 + \Delta\omega^2}\left(\Delta\omega^2 + \Omega^2 Cos\left[\left(\sqrt{\Omega^2 + \Delta\omega^2}\right)\cdot t\right]\right) \qquad (2.38)$$

where $\Delta\omega$ is the detuning frequency between the microwave frequency and the ESR transition frequency, i.e. $\Delta\omega = \omega_o - \omega_1$ and Ω is the microwave Rabi nutations frequency.

A width of the microwave π-pulse at a given power can be determined by the Rabi nutations experiments. When a longer duration of the resonant microwave signal at a given microwave power is applied such that all electron spins with m_s=0 are again brought into the ms=+/-1 states, the microwave pulse duration can be expressed as odd integer multiples of a π-pulse. Therefore, the exact time duration needed for a microwave π-pulse at a given microwave power can be determined by the Rabi nutation experiments.

Once the exact ESR transition frequency at a given external magnetic field strength was identified by the CW ESR experiments, Rabi nutation experiments with a resonant microwave frequency at given microwave power were then performed according to the experimental procedures shown in figure 2.24. In this experimental configuration, the microwave frequency should be fixed at the ESR transition frequency, e.g. transition frequency between m_s=0 and m_s=+1 states, and a constant microwave power modulated by various pulse widths is applied.

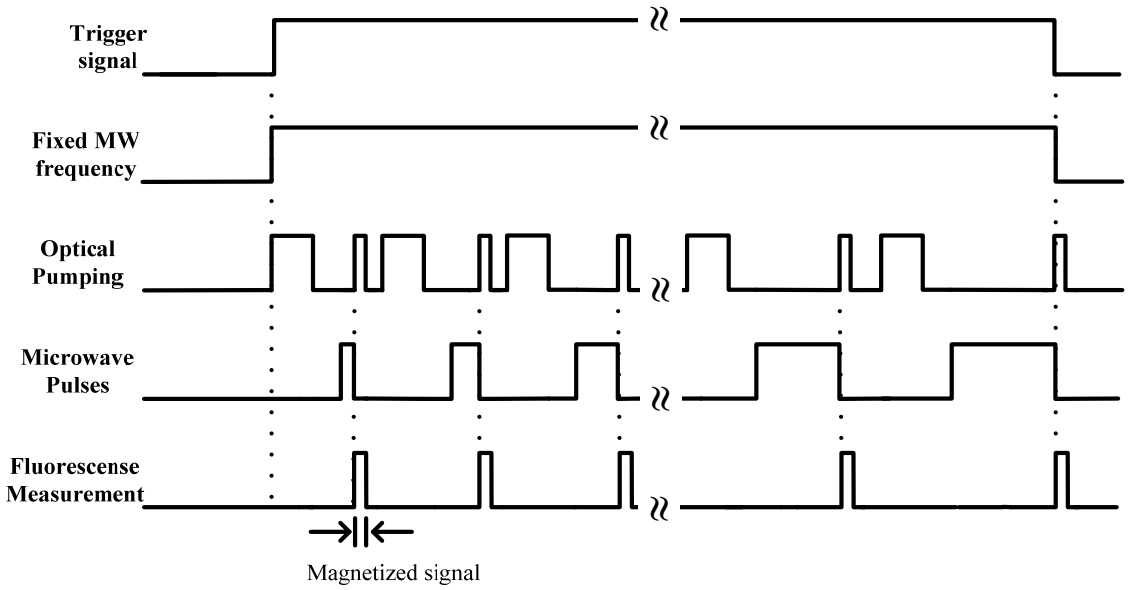

Figure 2.24 Schematic diagram for Rabi nutation experiments for electron spins of NV defects in diamond.

Electron spins are initialized to m_s=0 state by the optical preparation pulse followed by a relaxation time. While the optical excitation is switched off, a resonant microwave pulse with pre-programmed duration, varying from shortest to longest pulse widths is applied to manipulate the electron spins. After each microwave pulse, the fluorescence signal is detected by applying a short optical probe pulse.

By plotting the fluorescence signal as a function of microwave pulse duration, Rabi nutation of electron spin states can be obtained as shown in figure 2.25. Though no external magnetic field was applied in this experiment, the m_s=+1 state may be slightly shifted from the m_s=-1 state due to the residual magnetic field from the optic table or from the Earth's magnetic field. This may not be resolved in the wide ESR line due to the power broadening, but it can be manifested in the Rabi nutation experiments as a beating of the two frequency components with different amplitudes.

Therefore equation (2.38) for Rabi nutation was modified in order to include different oscillation frequency components as,

$$r(t) = r_o + \left(A_1 Cos\left(2\pi \frac{t}{p_1} \right) + A_2 Cos\left(2\pi \frac{t}{p_2} \right) \right) e^{-t/T_1} \qquad (2.39)$$

where T_1 is the decaying time.

In this experiment, a pair of bonding wires is used as a microwave transmission line. Microwave Rabi nutation periods of 78ns for an input power of 10dBm, and 116ns for an input power of 7dBm, and 320ns for 0dBm were obtained.

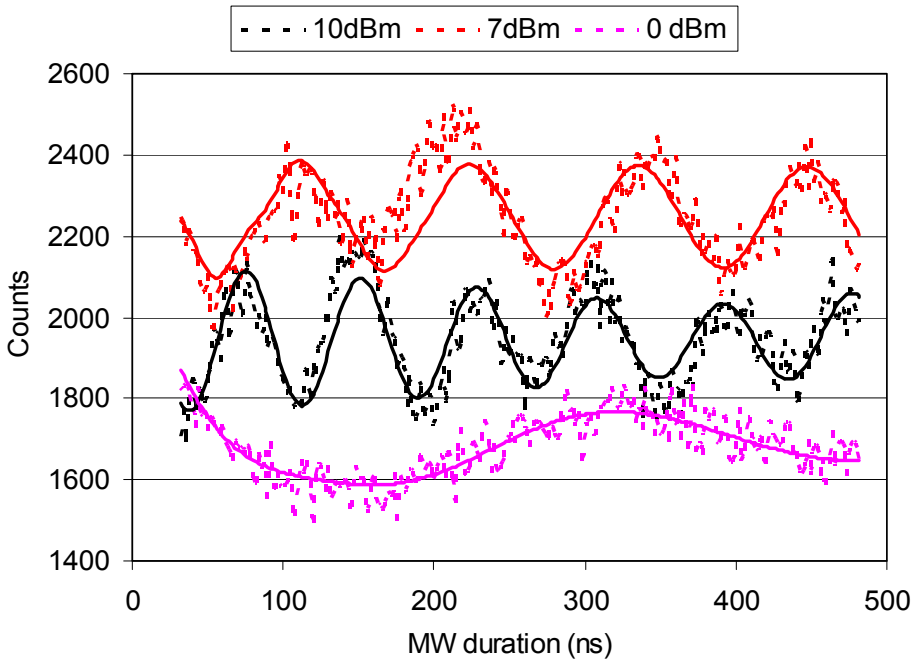

Figure 2.25 Rabi nutations of electron spin states of NV defects in diamond with microwave input power of 10dBm, 7dBm, and 0dBm were plotted. Dotted lines are experimental data, and solid lines are best curve fits with equation (2.39).

Since larger microwave power gives faster Rabi nutations as seen in the figure 2.25, properly designed microwave strip-lines can produce very high field, thereby ultra fast Rabi nutations can be obtained. This will be discussed in the next chapter.

4.3. Electron Spin Echo Experiments

Electron spin echo experiments can be carried out with the experimental procedures as schematically shown in figure 2.26. In this configuration, the duration of the microwave π-pulse at a given microwave power at the ESR transition frequency should be determined by Rabi nutation experiments as described previously. The well known Hahn echo pulse sequence can be modified as $\pi/2$-τ_1-π-τ_2-$\pi/2$ for optically detected spin echo experiments.

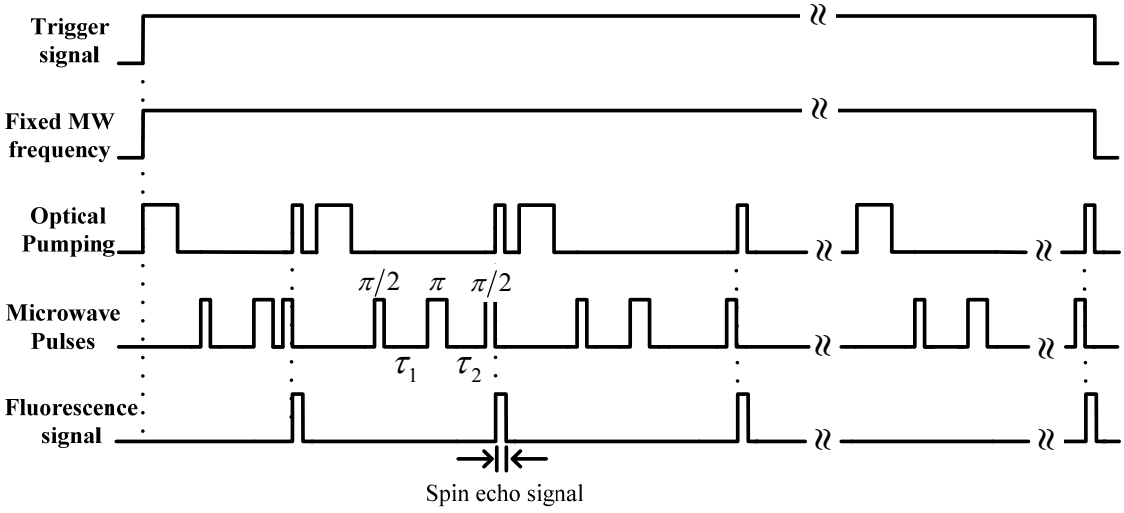

Figure 2.26 Schematic diagram of the electron spin Hahn echo experiments. Duration of microwave π-pulse is determined by Rabi nutation experiment as described previously. First waiting time (τ_1) for dephasing is fixed, but second waiting time (τ_2) for re-phasing is varying from shortest to longest according to the pre-programmed durations.

The microwave signal at a fixed frequency is kept at constant power, but is modulated by the pulse sequences of $\pi/2$-τ_1-π-τ_2-$\pi/2$, where π indicates a microwave π-pulse, which was determined by the Rabi nutations experiments, and τ_1, τ_2 are the first and second waiting times between the microwave pulses, respectively. The pulse sequences are pre-programmed, such that the second waiting time is varying from shortest to longest waiting time.

Time evolution of the electron spins upon resonant microwave irradiation by a modified Hahn echo pulse sequence is schematically is shown in figure 2.27. First, it is assumed that the optical preparation pulse followed by a relaxation time polarizes the electron spins into $m_s=0$ along the z-axis. Then, irradiation by the first microwave $\pi/2$-pulse along the x-axis rotates the magnetization of the electron spins by 90 degrees to the y-axis. During the first waiting time (τ_1), the electron spins evolve freely. The y components of the magnetized spins are inverted by the second microwave π-pulse, and then re-phased after the second waiting time (τ_2), if $\tau_1=\tau_2$.

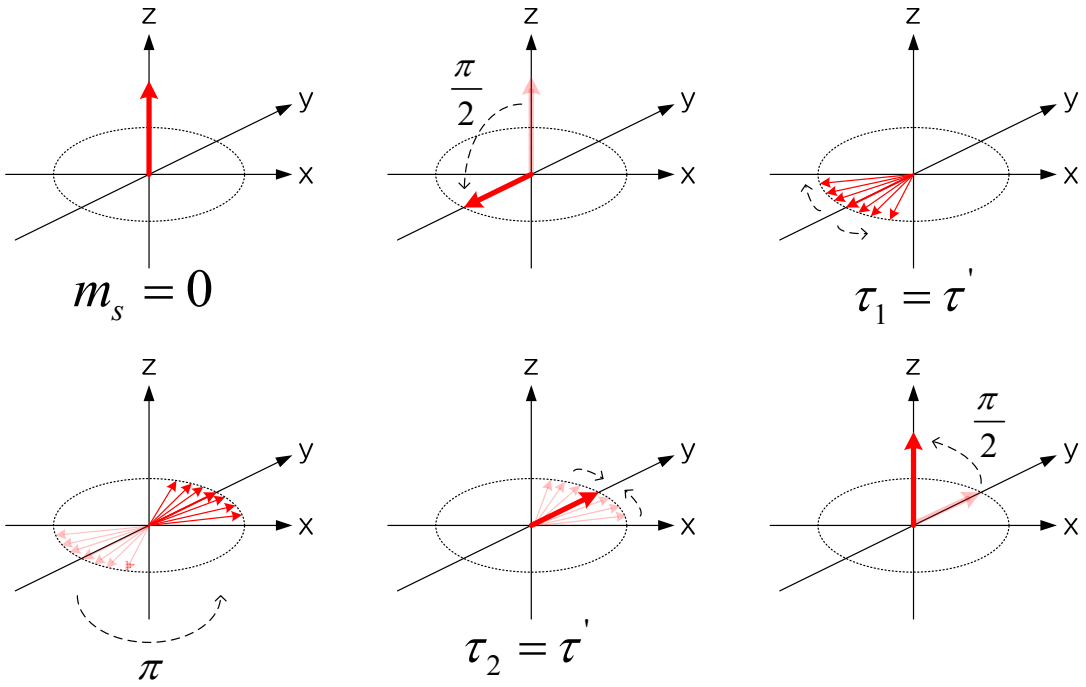

Figure 2.27 Schematic diagram of time evolution of the electron spin upon irradiation of modified Hahn echo microwave pulses are shown in the rotating frame when $\tau_1 = \tau_2 = \tau'$.

The rephrased y components of the spins are rotated back to the z-axis by the third microwave π/2-pulse along the x-axis, and then detected by the short optical probe pulse.

By using this Hahn echo pulse sequence, any spin dephasing caused by inhomogeneous external magnetic fields or the local environments can be decoupled, if the external fields and local environments do not change in the time scale of experiments. When this is done, the resulting spin-dephasing is due only to the T_2 relaxation.

Experimental data for the Hahn echo experiments in the absence of an external magnetic field are shown in Figure 2.28. Here a microwave π-pulse of 120ns at a microwave power of 7dBm was used. A first waiting time (τ_1) of 0.5μs was used for de-phasing. The fluorescence intensity reaches a maximum, when the second waiting time (τ_2) was also 0.5μs. When longer dephasing time of 1.0μs was used for the first waiting time (τ_1), the fluorescence intensity reaches maximum when the second waiting time (τ_2) is also 1.0μs. This verifies that the spins can be re-phased within the spin relaxation time.

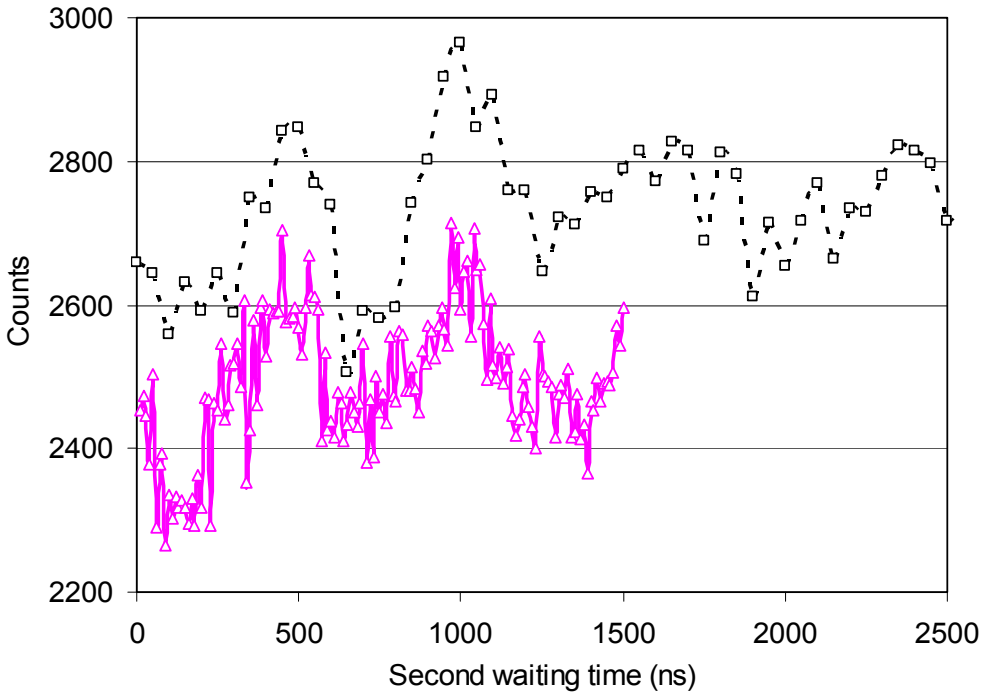

Figure 2.28 Experimental data for the Hahn echo experiments on a single NV defects in diamond with τ_1=0.5μs for solid line with triangles, and τ_1=1.0μs for the dotted line with squares. External magnetic field was not used, and microwave π-pulse of 120ns with microwave power of 7dBm at 2.87GHz was applied.

The T_2 relaxation time of the electron spins in NV defects created in the ultra pure type IIa diamond, was reported to be about 350μs at room temperature.

In summary, pulse mode ESR techniques, Rabi nutation experiments, and Hahn echo experiments were discussed in this section with detailed experimental procedures with preliminary results. These experiments together with photon antibunching experiments will be used to perform one dimensional ESR imaging with a magnetic field gradient using a micro gradient wire, and ultra fast electron spin manipulation with microwave striplines fabricated on the same substrates.

C. Device Fabrications

In this section, design of gradient coils for production of a DC magnetic field gradient, and microwave transmission lines for ultra fast Rabi nutations is discussed. Device fabrication processes include metal evaporation for thin metal film layers on a substrate, optical lithography for device patterning, electroplating for thick metal depositing, and etching of un-wanted metal layer. Devices are fabricated on diamond substrates, or other substrates, such as quartz microscope slides, and thin quartz cover slips with thicknesses of 150~200μm.

1. Design of Microwave Strip-lines and Magnetic Field Gradient Coil

In order to resolve multiple defects present in the small focal volume of a microscope objective lens, it is necessary to design a gradient coil that can provide a high magnetic field gradient within this focal volume. Though large permanent

magnets or superconducting magnets can provide a high magnetic field strength, their field gradient in micrometer or sub-micrometer scale is generally very small. Conversely, small permanent magnets can provide high field gradients but only very close to the magnet. Superconducting magnets can also be made very small but are complex to fabricate and require ultra-cold temperatures to operate. Recently, it was also reported that a non-superconducting gradient coil in micrometer size fabricated on a sapphire substrate can provide high magnetic gradient field at liquid helium temperature in vacuum.

As briefly mentioned in the previous section, properly designed microwave transmission lines can support a very high magnetic field strength at limited microwave power, so that ultra-fast spin manipulation will be feasible. Small gradient coils together with microwave striplines may allow us to resolve and address individual NV defects, even those located close enough that they cannot be optically resolved by the small focal volume of the confocal microscope. This will be useful to selectively address nearby spin quantum bits in a solid state quantum computing.

Since the microwave Rabi nutation frequency depends linearly on the microwave magnetic field intensity, a high microwave magnetic field intensity is desired. In general, the wave impedance, the ratio of transverse electric field to transverse magnetic field, should be small to achieve higher magnetic field intensity. But in the case of transverse electric magnetic (TEM) wave, the wave impedance is equal to the intrinsic impedance, which is determined by the electrical properties of the medium in which electromagnetic wave propagates. The fundamental propagating mode of transmission

lines, such as microstrip lines, is a quasi-TEM mode. The wave impedance of the quasi-TEM mode is mostly determined by the electrical properties of the surrounding materials and the geometrical structure of the transmission lines, but dimensional changes of the metal conductors affect wave impedance very little. Therefore, once the substrate and structure of the transmission lines are determined, wave impedance is assumed to be constant.

Since the input impedance of microwave equipments, e.g. microwave source, are typically terminated to 50Ohm, transmission lines with a characteristic impedance of 50Ohm and small ohmic loss will provide the highest current on the signal wire, so that magnetic field intensity will be largest.

The wavelength of the microwave signal at around 3GHz is couple of centimeters in the transmission lines, which is comparable to the overall size of the fabricated devices. Therefore, devices should be designed to be 50Ohm except for the very short narrow wires. The narrow wires for the gradient coil or microwave striplines are a few hundred micrometers long, so they are assumed to be a lumped element, in which voltage and current can be assumed constant.

Electromagnetic simulations were carried out using commercially available software (IE3D, Zeland). A schematic diagram of the 50Ohm transmission lines for coplanar microstriplines is shown in figure 2.29. Quartz substrates were chosen since they have low fluorescence, and copper was chosen due to the high DC conductivity. A surrounding medium of air was assumed. The input impedances of port 1 and port 2

are defined to be 50Ohm. Therefore, reflection loss and transmission loss of the designed co-planar micro strip-lines can be estimated as shown in figure 2.30.

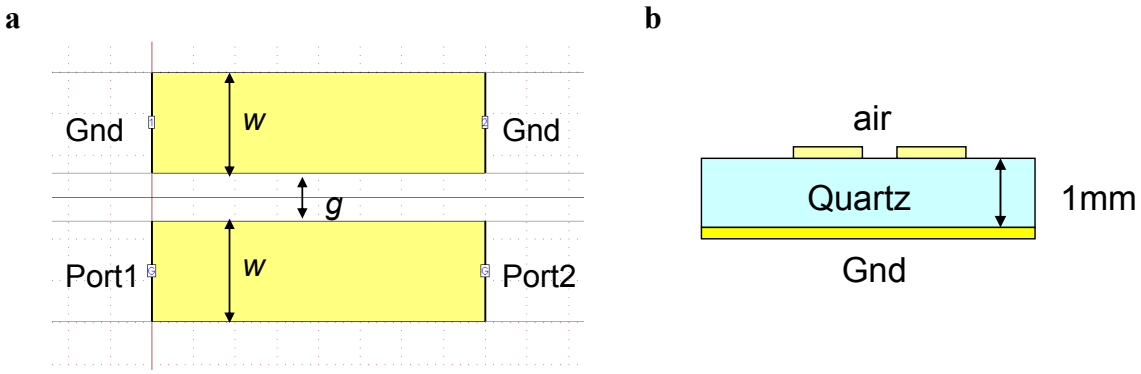

Figure 2.29 **a**, Top view of the simulation structure for the 50Ohm coplanar microwave striplines. **b**, Cross-section view. Metal conductors shown in yellow color are 2μm thick 300μm width copper strips with ground plane on the other side of the substrate. Separation or gap is 104μm. Thickness of quartz substrate is 1mm, and relative dielectric constant of 4 is assumed.

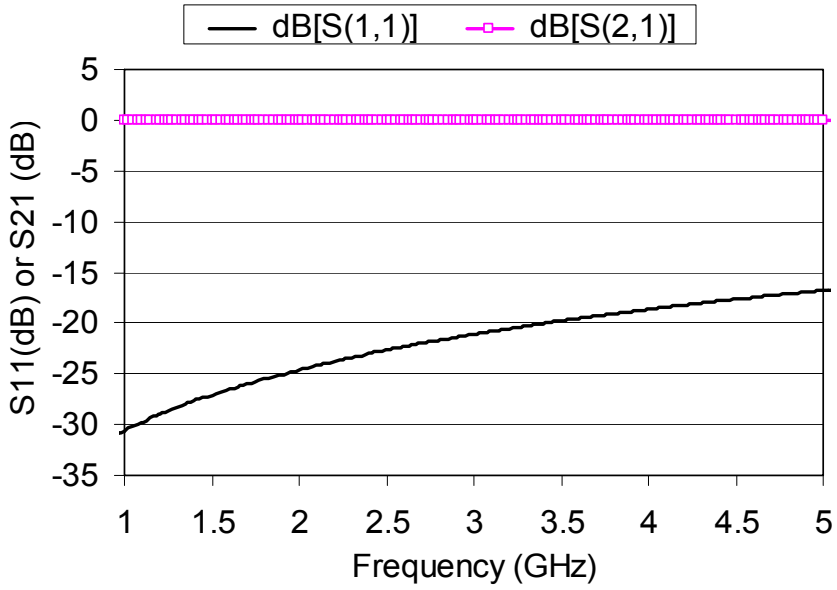

Figure 2.30 Simulation results of 50ohm coplanar striplines with dimensions as described in figure 2.29.

At around 3GHz, S11 is less than -20dB, which indicates that less than 1% of input power will be reflected, and S21 is greater than -0.04dB, which indicates that transmission loss will be less than 1%. Therefore, this 50Ohm co-planar microwave stripline will be used for transmission lines between the narrow wires and the microstriplines of the microwave circuit board.

Since the length of the narrow wires is small in terms of the wavelength, any reflection loss due to the impedance mismatch between narrow wires of 2-10μm width and the 50Ohm lines is expected to be negligible. In order to estimate the transmission loss, the narrow wire transmission lines are simulated as schematically shown in figure 2.31.

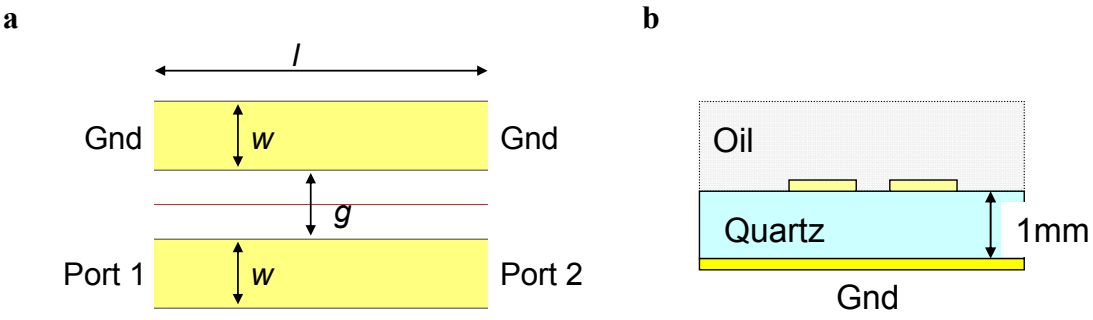

Figure 2.31 Schematic drawings of narrow microwave striplines are shown. **a**, Top view. **b**, Cross-section view. Width (*w*) of the wires are the same as gap (*g*), varying from 2-10μm, thickness of metal is 2μm. Length (*l*) of the wires is 400μm. Dielectric constant of immersion oil is 2.3.

Input impedances of the port 1 and port 2 are again 50Ohms, and immersion oil with dielectric constant of 2.3 was assumed above the devices, corresponding to the experimental configuration. As expected, reflection loss at 3GHz was less than -23dB regardless of the wire width. As the width of the wire decreased, transmission loss

slightly increased, but it is still acceptable, since more than 93% of the microwave power is transmitted as shown in figure 2.32 (a). More importantly, the maximum current density increased, as the width of the wire decrease. In consequence, a much higher magnetic field intensity can be induced near the narrower wires as shown in figure 2.32 (b).

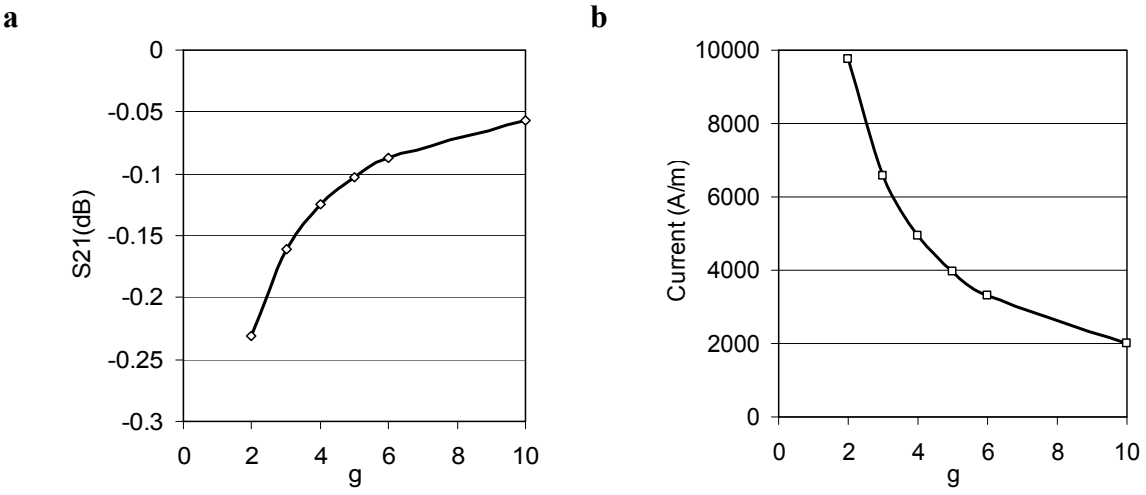

Figure 2.32 Simulation results of narrow microstriplines seen in figure 2.31 are shown. **a**, S21 is plotted as a function gaps in micrometers. **b**, Maximum current density on the signal wire is plotted as a function gaps in micrometers.

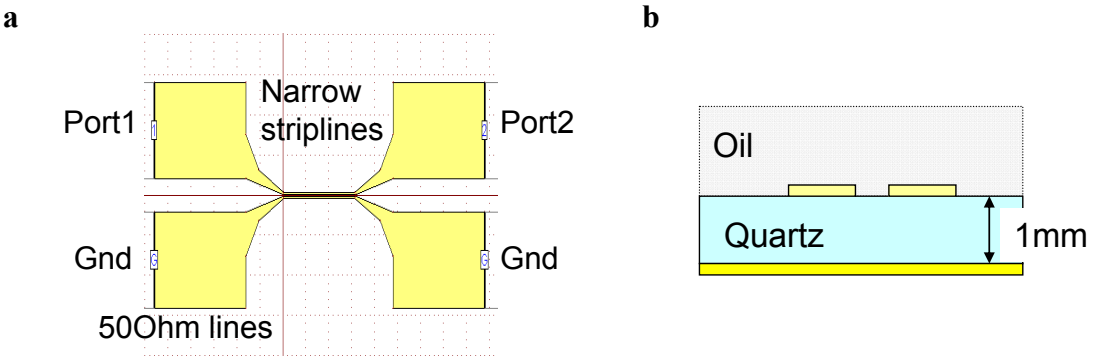

Figure 2.33 Simulation structure of narrow wires with 50Ohm coplanar microstriplines. **a**, Top view. **b**, Cross-section view. Gap and width of the narrow wires are 6μm, and 50Ohm transmission lines have the same dimension as described in figure 2.29. Metal thickness is 2μm and width is 6μm.

Narrow wires with a gap and a width of 6μm were combined with 50Ohm coplanar microwave striplines as schematically shown in figure 2.33.

However, as the cross section of a wire becomes smaller, DC resistance increases, which results in higher transmission loss for the microwave signal, and higher power dissipation for the DC current. Power dissipation is critical issue since micrometer size wires can easily be heated up in milliseconds, and quickly oxidized. Therefore, too narrow wires should be avoided.

Again, port 1 and port 2 have input impedance of 50Ohm, and the taper sections were adopted in order to reduce any reflection loss and to enhance the uniformity of the electroplating rate. Simulation results are shown in figure 2.34. At 3GHz, S11 is smaller than -20dB, i.e. reflection loss is smaller than 1%, and S21 is larger than -0.1dB, i.e. more than 97% of the power is transmitted.

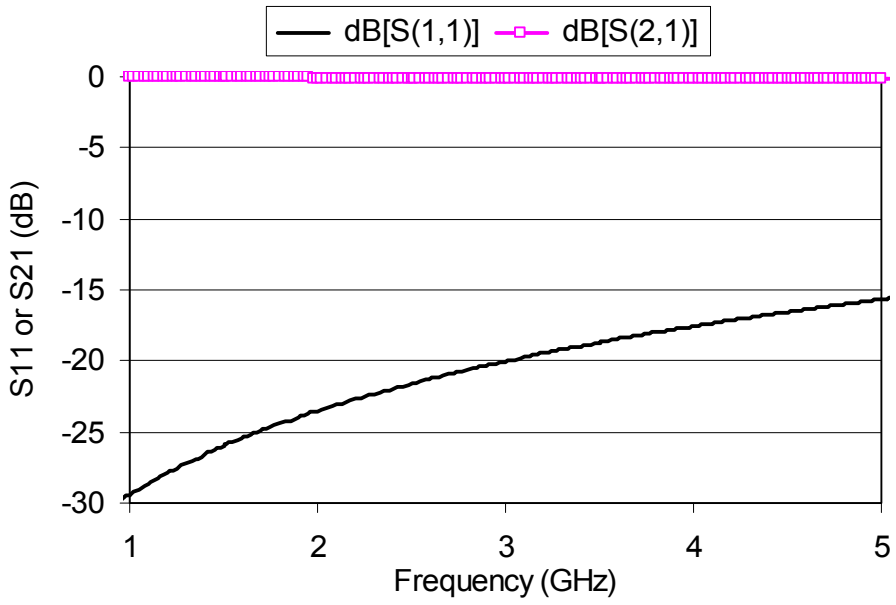

Figure 2.34 Simulation results of 6μm microstriplines with 50Ohm transmission lines.

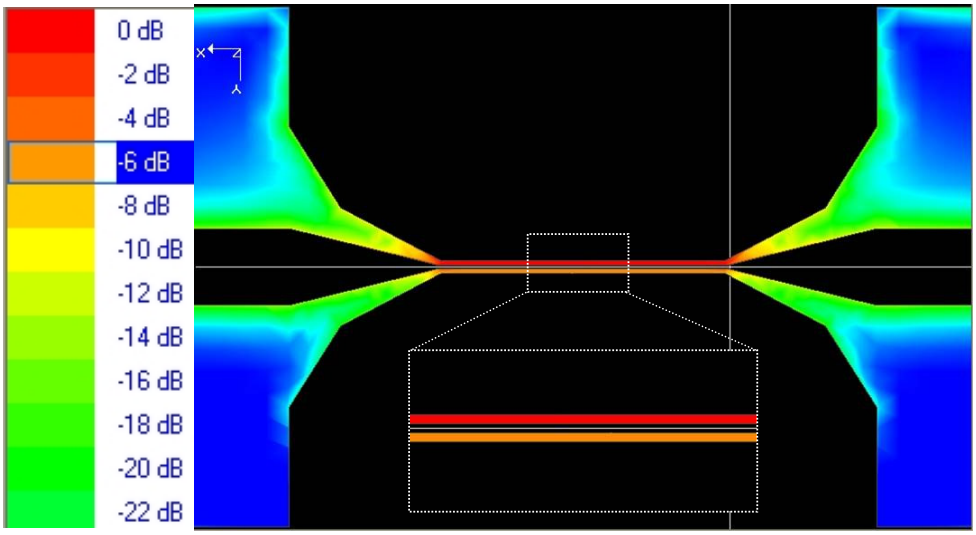

Figure 2.35 Maximum current density of the 6μm microstriplines with 50Ohm coplanar transmission lines is plotted on the surface of the metal conductors.

The surface current density on the metal conductor surface was plotted in figure 2.35. Since the current density is almost 100 times larger in narrow wires than in the wider 50Ohm co-planar microstriplines, NV defects near the narrow wires could experience 100 times higher magnetic field intensity and 10,000 time higher field gradient than those near the wide 50Ohm pads.

In an attempt to achieve a 2 dimensional field gradient, a structure consisting of coplanar microstriplines with 4 DC gradient coils was designed, and simulated as shown in figure 2.36. At 3GHz, S11 was less than -15dB and S21 was larger than -0.5dB, therefore less than 4% of the input power is reflected, and more than 89% of the power will be transmitted. The estimated DC resistance for a 400μm long copper wire of 6μm width by 2μm thick is about 0.57Ohm.

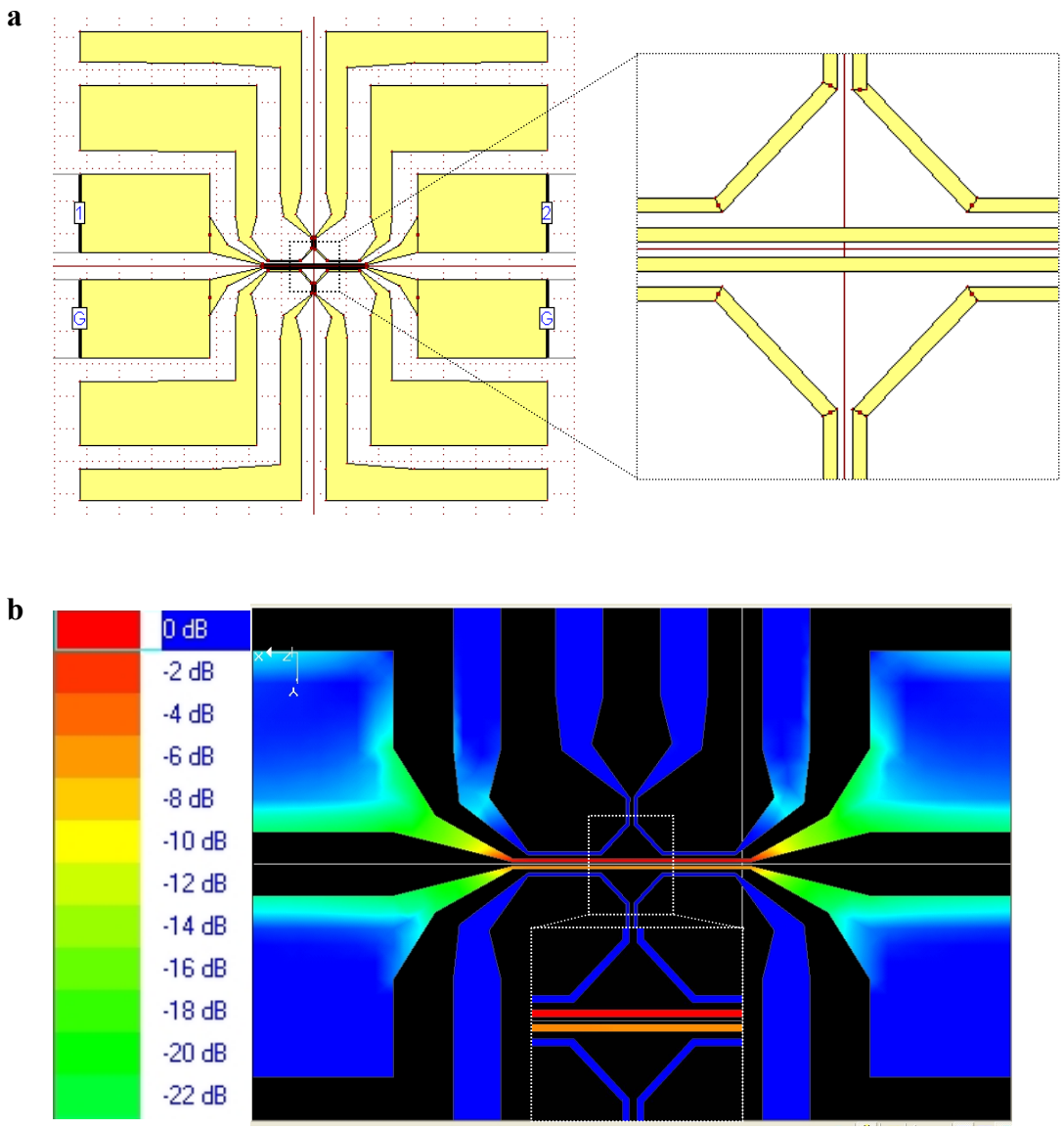

Figure 2.36 **a**, Schematic drawing of 4 DC gradient coils with 50Ohm coplanar transmission lines. **b**, Current density of 6μm microstriplines is plotted on the metal surface.

Based on the simulation results discussed above, microwave striplines with 4 DC gradient coils of 6μm, and 10μm were designed. Others patterns including high voltage electrodes for Stark shift experiments, and grid marks to register the locations of specific NV defects of interest were also designed. In order to fabricate the designed devices by

optical lithography, 4 inch photo masks with a spot size of 0.25μm were manufactured by a company (Microtronics, Inc.). Structure fabrication processes will be discussed in the following subsection.

2. Fabrication Process Including Optical Lithography, Electroplating and Etching

Devices fabricated by optical lithography should be placed directly on the diamond substrates, if possible. But it is a challenge to fabricate 1~2μm thick devices with a resolution of a few micrometers on diamond substrates, since the diamonds are small, and inconvenient to handle (c.f. typically diamond is a few millimeters by a few millimeters). Also, the photoresist may not survive during the metal deposition at the required high temperature of about 350degrees C.

An alternative is to fabricate shadow masks first, and then fabricated shadow mask is placed on top of the diamond substrate followed by metal deposition through the apertures of the shadow mask. Another way is to fabricate devices on low fluorescence substrates, and then bulk diamond samples or nano diamond crystals are placed on top of the fabricated devices for the experiments.

Fabrication process using a shadow mask technique will be discussed first, and then the second fabrication process, i.e. fabricating devices on quartz substrates will be discussed.

2.1. Device Fabrication on Diamond Substrates Using Shadow Masks

In order to fabricate shadow masks, we should first start with thin metal layers. Although we can use electro-plating to get thick metal layers, devices can not be fabricated directly on the thick metal layer, unless anisotropic etchants are used. Isotropic etchants attack at a uniform etch rate in all directions, and so undercut can be a serious problem for small features on thick metal layers. UV activated anisotripic etchants are recently reported, but are not available at this time. Therefore, the devices were patterned on the photo-resist spun onto thin metal layers, then electro-plating was applied to make the patterns thicker, e.g. 10~15μm for a shadow mask.

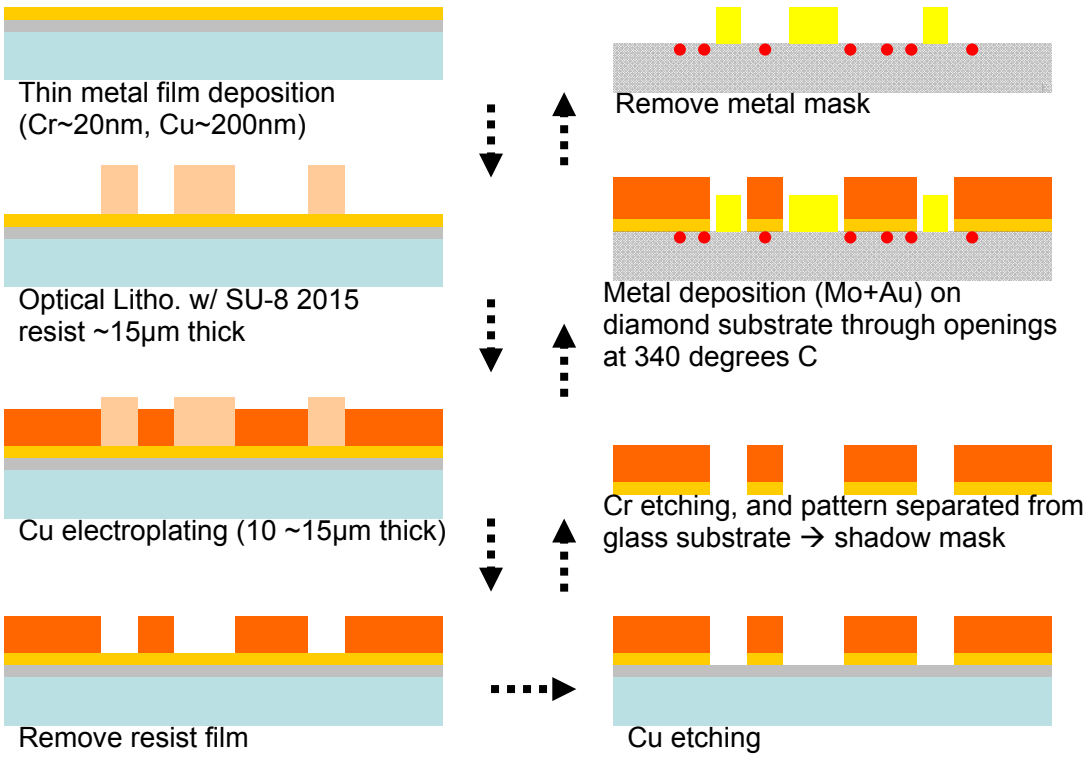

Figure 2.37 Schematic diagram of device fabrication processes using shadow masks.

A schematic diagram to fabricate a device on a diamond substrate is shown in figure 2.37. Initial metal layers of chromium and copper of 20nm, 200nm, respectively, were deposited on the glass substrate. Then, the substrates were spin-coated with Su8-2015 photoresist at 3000rpm for 30sec. After pre-baking, patterns were printed by the contact printing method followed by post-baking and a development processes. Once the patterns were fabricated on the glass substrates, a thick copper layer of about 10~15μm was electro-plated through the openings of the pattern. After removal of the photo-resist, a short copper etching time was applied to remove the thin copper layer in the un-wanted area. Then, the sample was placed in the strong Cr etchant (e.g. CR-473, Transene Company Inc.). Once the Cr layer was completely etched-off, the shadow masks could be separated from the glass substrate. In order to improve the etching process, the Cr etchant can be heated up at 70 degrees C.

a **b**

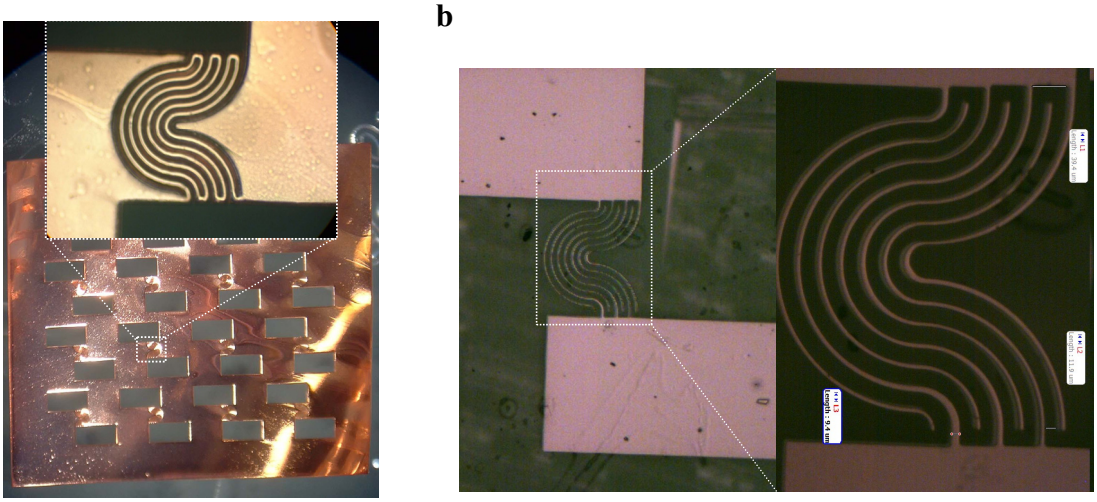

Figure 2.38 **a**, Image of fabricated shadow mask for high voltage electrodes. **b**, Image of fabricated device on diamond using fabricated shadow mask.

After the shadow mask was fabricated, it was placed on top of the diamond substrate, and thin molybdenum and gold layers of total thickness of ~200-300nm were deposited by electron-beam evaporation. Photo images of the fabricated shadow mask and high voltage electrodes fabricated on diamond are shown in figure 2.38.

Though some patterns were successfully fabricated in this way as shown in figure 2.38 (b), there are some issues. One is that thin deposited devices peeled off when high voltage was applied in the microscope immersion oil. The other issue was imperfections in the shadow masks. Though copper was electro-plated to about 10~15μm thick, some of the suspended structures of the shadow mask for microwave striplines or DC gradient coils were displaced since the shadow mask was not always in good contact with the glass substrate, and this caused photoresist residues to remain in the small gaps.

Therefore, this fabrication process using shadow masks may not be efficient to fabricate the very small devices, shown in figure 2.39, on the diamond.

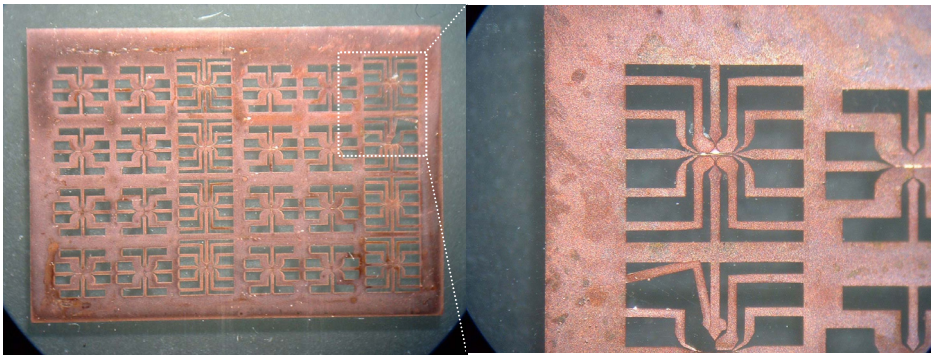

Figure 2.39 Fabricated shadow mask for microwave striplines with DC gradient coils.

2.2. Device Fabrication on Low Fluorescence Quartz Substrates

Another fabrication process is fabricating devices directly on low fluorescence substrates, such as quartz substrates, and then the diamond samples can be placed close to the device. These fabrication procedures are schematically shown in figure 2.40.

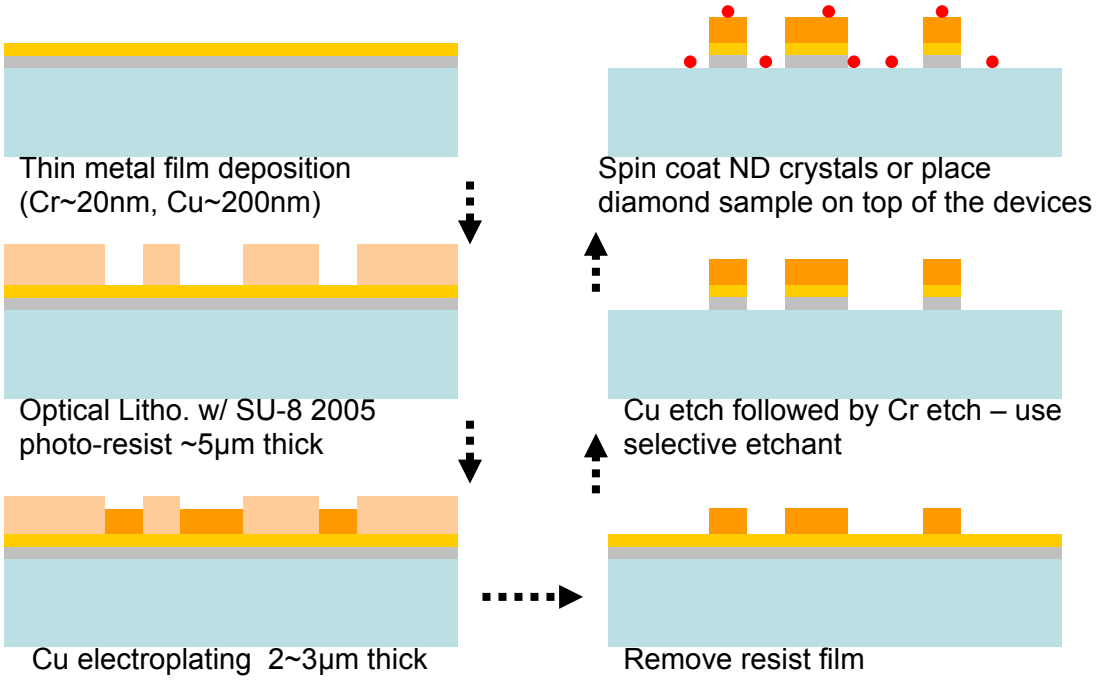

Figure 2.40 Alternative fabrication processes are shown schematically.

Once devices are fabricated on the low fluorescence substrate, NV embedded nano-diamond crystals can be spin-coated or a bulk diamond sample can be placed on top of the device. Due to the short working distance of a high numerical aperture microscope objective, thin substrates of 150~200μm thick should be used for the later configuration. The working distance of the oil immersion microscope objective in our setup is 130μm with a cover glass thickness of 170μm, a bulk diamond sample can be placed on top of the thin quartz cover glass next to the devices, while the microscope

objective for the optical excitation and fluorescence signal detection can be placed to the other side, i.e. back-side illumination technique.

Though thin substrates may be trickier in terms of fabrication due to the difficulties of handling thin fragile substrates, it would be more favorable in terms of experiments. The reason is that spin-coated nano diamond crystal films on the substrate can be dissolved by the immersion oil as time elapses and so having the oil on the back side of the substrate is important.

Thin sample substrates were prepared as follows. First, thin quartz substrates of 150~200μm thick were attached to thick glass microscope slides using double sided Kapton tape. Substrates were cleaned by acetone, rinsed by isopropanol and then blow-dried with nitrogen gas. Next, dehydration baking was performed at 200degrees C for less than 5 minutes. Then, oxygen plasma cleaning was used with an RF power of 150 Watts for 40 seconds.

Metal layers of chromium and copper were deposited by a thermal evaporator (Auto 306 Metal Evaporation Chamber, BOC Edwards). In order to improve surface adhesion of the copper layer to the substrate, the thin chromium layer was deposited first.

Once the pressure inside of the deposition chamber reached 1.1×10^{-6} Torr, a deposition current was applied and increased slowly up to 1.8~2A. At this current, the tungsten rod with chromium coating is heated up, and out-gassing from the Cr increases the pressure inside of the chamber. After out-gassing, we decrease current in order to recover the vacuum pressure, and then increase the current slowly up to about 4A.

Once piezo-crystal thickness sensor started reading the deposition, the shutter was closed for 10-30sec to dispose of the initial Cr vapor. In order to improve the quality of the deposited film, the Cr layer was deposited slowly at a rate of 0.06-0.1nm/s. It took about 5-6 minutes to get 20nm Cr layer. During the deposition, pressure and temperature usually increased to 6.0×10^{-6} Torr and 63degrees C, respectively. Once Cr deposition was done, the current was slowly decreased to zero, and we waited for 5-10 minutes to recover the pressure, and lower the temperature. After that, the copper layer was deposited using the same procedures. If the vacuum pressure and temperature went up too much, i.e. more than 1.2×10^{-5} Torr, and 130degrees C, respectively during the deposition, the current was reduced to zero in order to recover the vacuum and lower the temperature. After about 10 minutes of waiting time, deposition was continued, and finally stopped after total thickness of 200nm was deposited. Typically, the deposition rate of copper was 0.1~0.2nm/second.

After metal deposition, the devices were fabricated by optical lithography as follows; first the substrates were spin-coated with Omnicoat at 3000rpm for 30seconds, and baked on the hotplate at 200degrees C for 1 minute. After the substrate was cooled down, it was spin-coated with Su8-2005 photo-resist at 3000rpm for 30seconds, and then pre-baked for 150seconds while the temperature increased from 82 to 93degrees C. After it was cooled, the photo-resist film was masked and exposed by UV light of the mask aligner (Q-4000, Quintel company), so that the mask patterns were printed on the resist. The UV intensity was about 10.35mW/cm^2, and the exposure time was 9seconds. Then, the sample was baked (post exposure bake) on a hot plate for 105 seconds while

the temperature was increased from 82 to 93degrees C. After cool down, the exposed photo-resist patterns on the substrate were developed for 1 min in the Su-8 developer. During the development, gentle agitation may be applied in order to improve mass transfer rate in the narrow channels.

Though many devices were fabricated in the same batch, the quality of the individual fabricated patterns could be slightly different due to the un-known effects. Photo images of fabricated patterns are shown in figure 2.41.

a **b**

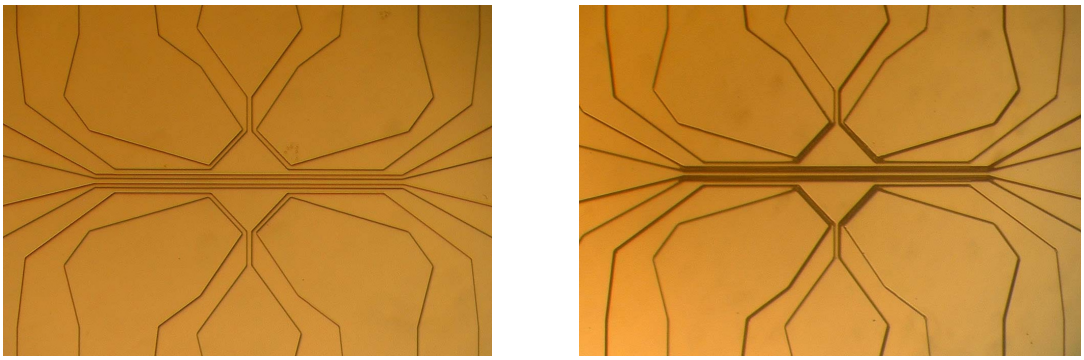

Figure 2.41 **a**, Photo-images of developed photo-resisted patterns with clean channels. **b**, Clogged channels. Channel width was 6μm in these images.

After samples were blow-dried, oxygen plasma cleaning (de-scumming) was applied with an RF power of 350Watts, and oxygen flow rate of 35sccm. If the channels were clean, the plasma was applied for only 20secnds to remove thin omni-coat film in the un-covered area, but if channels were seriously clogged by the photoresist residue, then it was applied for up to 150seconds depending on the photoresist residue in the channels.

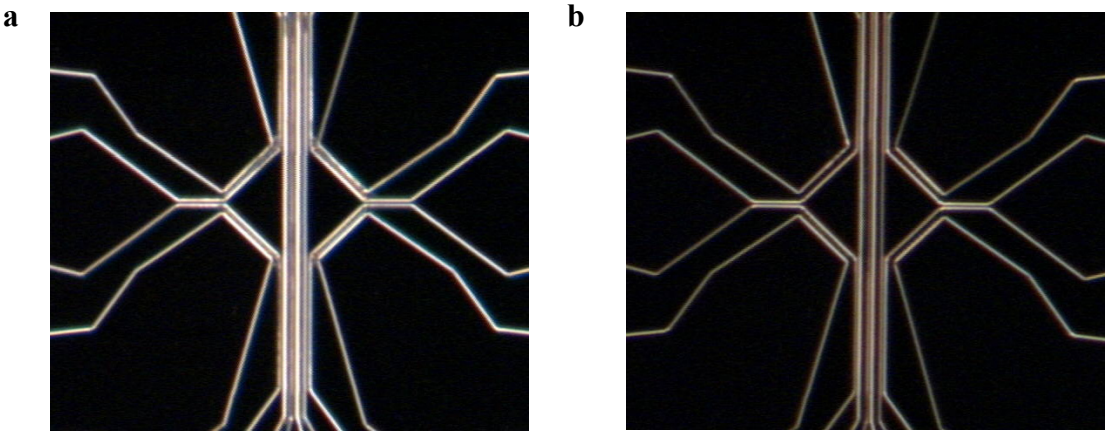

Figure 2.42 Photo images of developed photo-resist pattern. **a**, Channels are clogged with photo-resist residue. **b**, Channels are cleaned by oxygen plasma etching for 70 seconds with RF power of 350Watts, oxygen flow rate of 35sccm.

Oxygen plasma cleaning etches off exposed and un-exposed photo-resist, but the un-exposed area has a faster etching rate. Therefore, clogged channels could be cleaned as seen in figure 2.42. The profile of the developed photo-resist patterns, measured by the profile-meter (Dektak 3 Stylus Profilometer, Veeco), are shown in figure 2.43 for various oxygen plasma etching times.

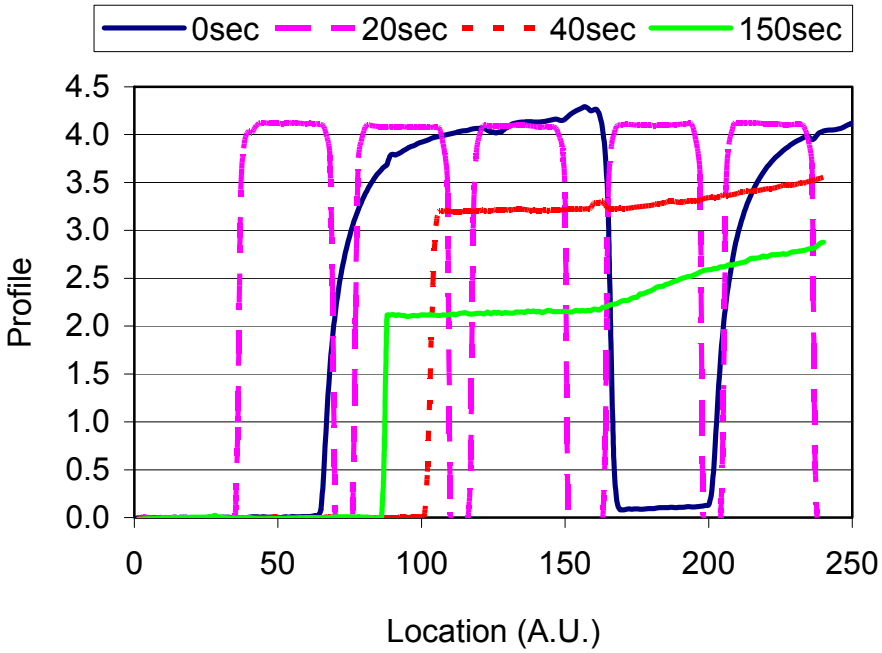

Figure 2.43 Profiles(μm) of the developed photo-resist patterns after oxygen plasma etching for various oxygen plasma etching time are plotted.

The initial photo-resist thickness was about 4.1μm. After oxygen plasma etching for 20, 40, and 150 seconds, it was measured to be 4.0μm, 3.3μm, and 2.16μm, respectively.

As previously shown in the simulation results, the impedance mismatch for the microstriplines is negligible. But transmission loss or power dissipation issues of the DC gradient coils due to a large DC resistance can be more serious. In order to reduce the DC resistance of the narrow wires for microwave signal or for the DC current, the wires should be thicker, at least thicker than skin depth of the microwave signal, which is about 1μm at 3GHz. After examining photo-resist patterns under the microscope to see if channels are clean, the patterns were electro-plated in order to make the un-covered metal pattern thicker.

Electroplating deposits metal layers on a metallic object in a chemical solution by applying a negative charge onto the object. A schematic diagram is shown in figure 2.44.

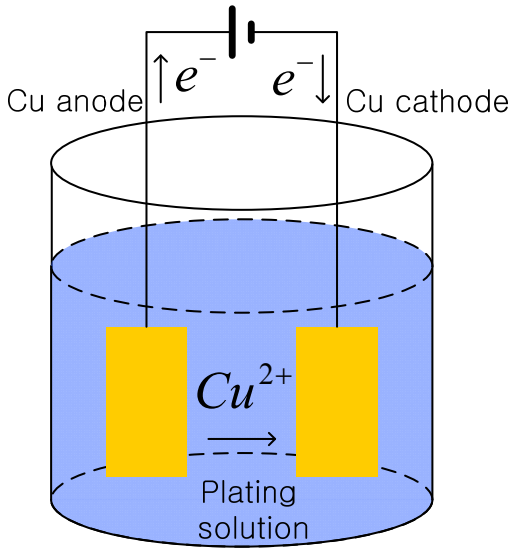

Figure 2.44 Schematic diagram for copper electroplating setup.

Due to the electric field, copper ions in the plating solution migrate to the cathode, and deposit as elemental copper according to the half-reaction: $2e^- + Cu^{2+} \rightarrow Cu$, and copper from the anode is oxidized, and goes into solution according to the half-reaction: $Cu \rightarrow Cu^{2+} + 2e^-$. The total amount of deposited copper on the cathode is equal to the weight loss of the anode. Some additives can be added in order to improve the throughput or the quality.

In the fabrication, commercially available plating solution (Techni Copper U, Technic Inc.) with a phosphorized copper piece for the anode was used. The surface area of the anode size was roughly matched to the total open area (e.g. 5.51cm^2) of the

fabricated photo-resist patterns. In order to get a uniform deposition rate over the area, a small current of 60mA was applied for 10 ~15 minutes depending on the sample. The experimentally estimated deposition rate was about 300 ~ 400nm/minute. No agitation was applied, since agitation may produce air bubbles or currents of the solution. Air bubbles can prevent copper from depositing in that area, and currents can make faster deposition in some areas, but much slower deposition in others. Figure 2.45 shows a photo image of an electroplated sample.

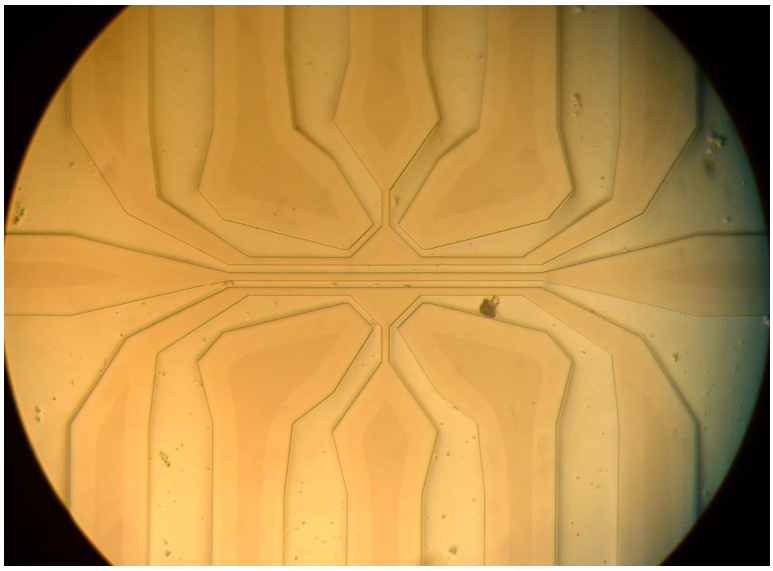

Figure 2.45 Photo-image of electroplated samples.

Once copper electroplating was done, the photo-resist was removed by placing the samples in the solvent (Microposit Remover 1165, Shipley) for 10 minutes, which was heated up to 78 degrees C, and then rinsed with DI water and acetone. Most of the photo-resist in the larger areas was removed, but residues of photo-resist in the narrow channel area remained as shown in figure 2.46.

a **b**

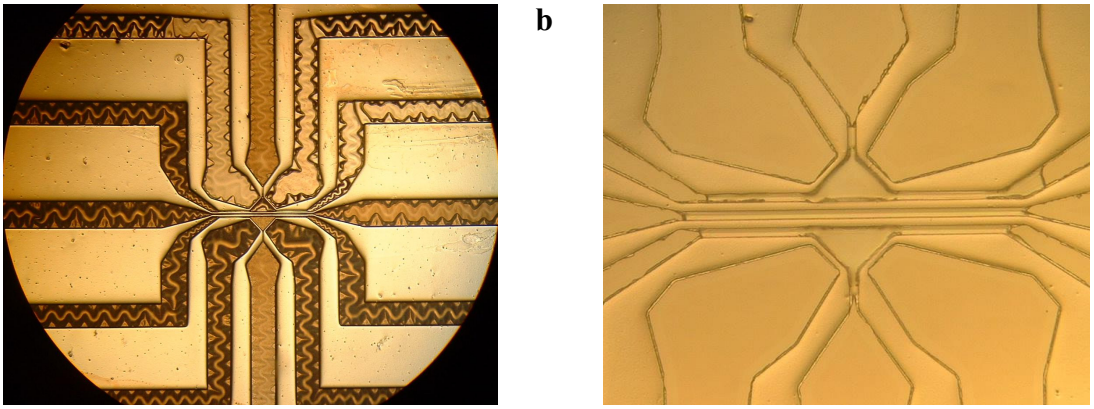

Figure 2.46 Photo-images of the fabricated sample after removal process with remover 1165. **a**, Photo-resist is softened by the remover. **b**, Some residues of photo-resist remained in the narrow channels.

In order to clean the photo-resist residues in the narrow channels, plasma etching was applied for 90seconds with an RF power of 350Watts, an oxygen flow rate of 80sccm, and a carbontetrafluoride (CF_4) flow rate of 8sccm. When plasma cleaning is applied to substrates with metal layers, the metal should be properly grounded, since otherwise the strong RF power may induce large charge concentrations on the metal layer and damage the substrates by arcing.

Once the photo-resist was completely removed, the thin copper layer was etched off for 70seconds by a custom made etching solution (Acetic acid: Hydrogen peroxide: DI water = 1:1:10). This etchant selectively attacks copper only. The measured etch rate was about 450nm/minute at room temperature. It was a little over etched intentionally, since the etch rate in the narrow channel was slower than in the wide area due to the slower mass transfer rate in the narrow channel. After copper etching, the samples were examined under a microscope to confirm that copper in the channel area was completely removed. After that, the un-covered thin chromium layer was etched

off for 4minutes by a commercially available etching solution (CR-100, Cyantek) with an etching rate of 10nm/minute. It was also a little over-etched intentionally in order to prevent any short circuits. In the chromium etching process, a slow etching rate is crucial. If etching rate is too fast, sidewall attack in the narrow wires may cause serious undercut, and thereby the narrows wires will be lost.

Devices were successfully fabricated, and photo-images of the fabricated devices are shown in figure 2.47.

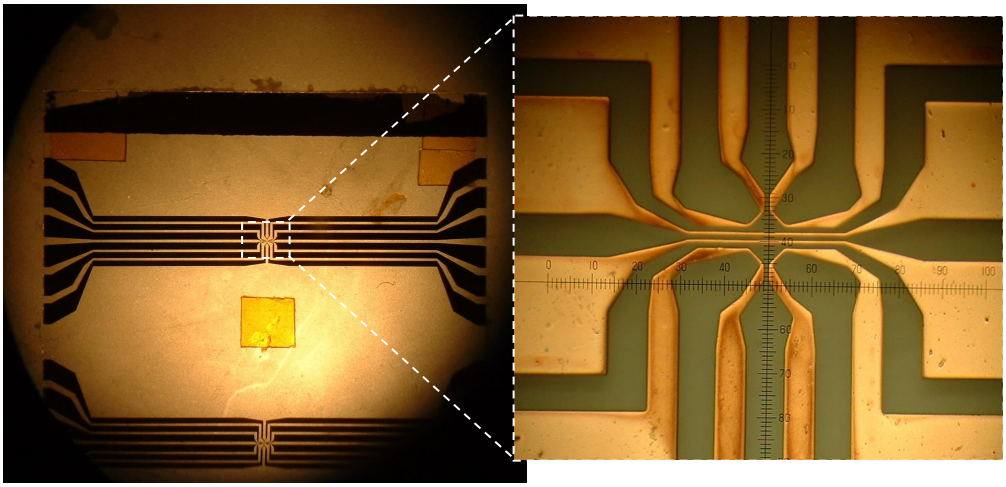

Figure 2.47 Photo-images of fabricated devices on quartz cover-slip.

3. Characterization of Fabricated Devices

A diamond sample, in which NV defects are embedded, was placed on top of the device fabricated on a low fluorescence quartz cover slip substrate, and the cover slip with a fabricated device was mounted on a custom made microwave circuit board as shown in figure 2.48 (a), and it was connectorized using SMA connectors as shown in figure 2.48 (b).

a

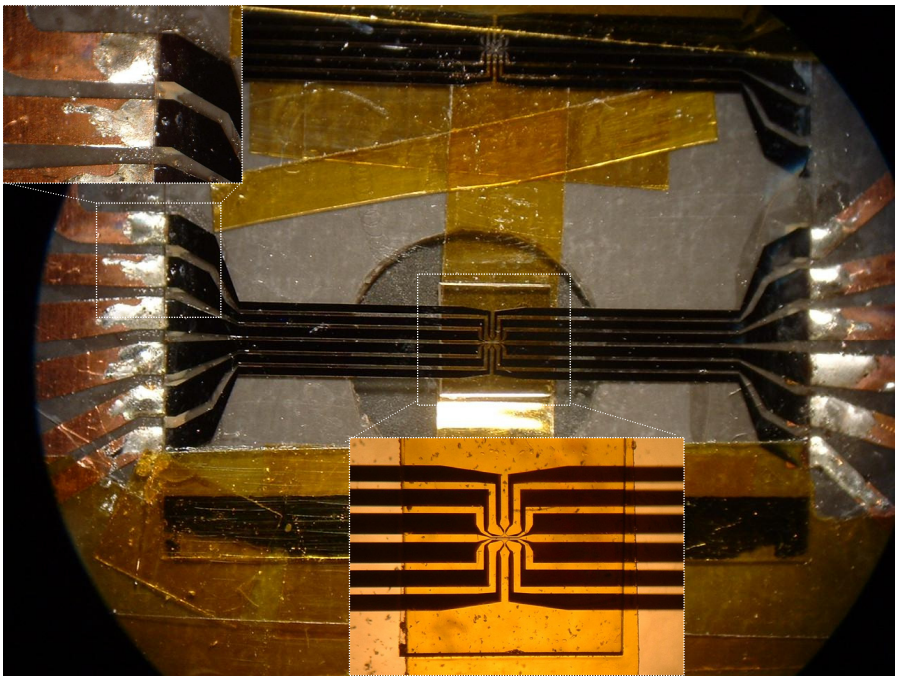

b

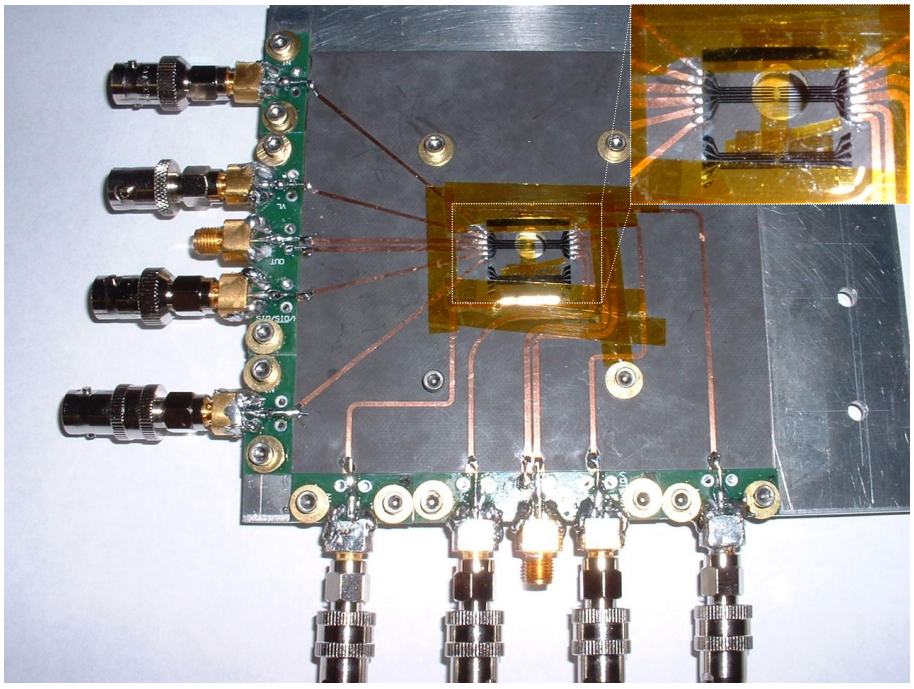

Figure 2.48 Device with a bulk diamond sample is mounted on a microwave PCB board. **a**, Contact was made by a solder-it. **b**, Microwave circuit board is connectorized using SMA connector.

Kapton tape was used to secure the bulk diamond onto the fabricated device, and the fabricated device was soldered to the microwave circuit board using a solder-it (Solder-It, Inc.), which is a mixture of soldering flux with silver-bearing small metal pieces.

The mounted sample was tested for DC power dissipation, and microwave characteristics as follows. First, the DC resistance of the gradient coil was measured to be 0.8~1.5 Ohm depending on the sample, and then it was connected to DC power supply through an ampere meter. Continuous DC current was slowly increased until the coil became an open circuit. The DC resistances of a mounted device for the experiments were 1.1Ohms, 1.5Ohms for the gradient coil, and the co-planar microstipline, respectively. The gradient coil was stable up to 300mA, but it was unstable at higher current. At around 400mA, it became open circuit as shown in figure 2.49. From this we concluded that the gradient coil can dissipate a DC power of about 100mW without any problem.

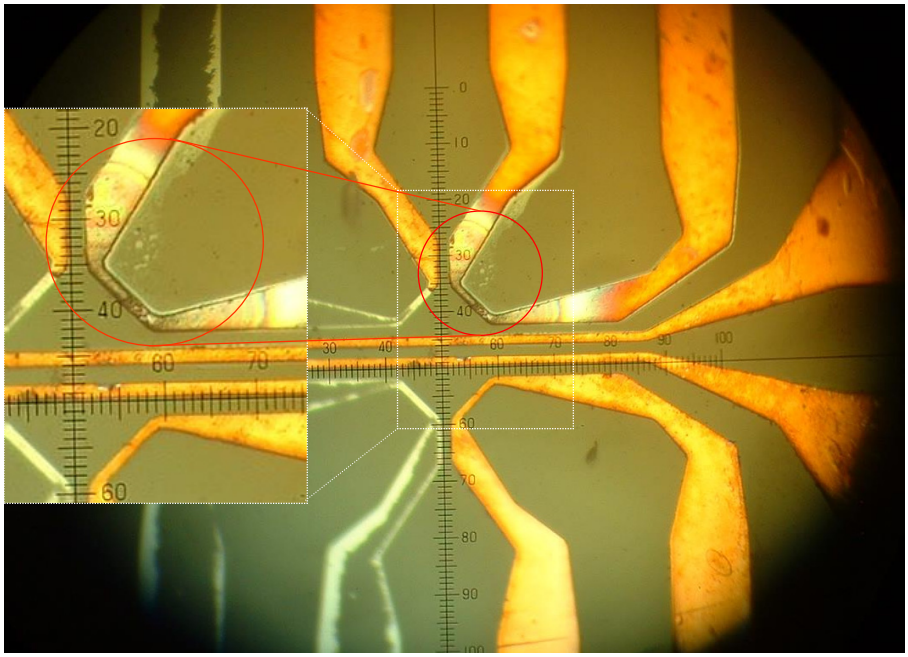

Figure 2.49 Photo image of damaged gradient coil after a test for the maximum power dissipation with DC current. This test was made in the absence of bulk diamond sample.

In order to apply a higher current, the duty cycle of the gradient pulse, which will be couple of hundred nano seconds in the experiments, is adjusted so that time-averaged power dissipation is under 100mW. For example, with 1% duty cycle, about 3A can be applied to the gradient coil.

Microwave characteristics of the devices were measured using a vector network analyzer (HP8510B, Hewlett Packard). First, the measurement system was calibrated with a standard calibration set. Then scattering parameters at the SMA connectors of the mounted device shown in 2.48 (b) were measured as a function of the frequency as shown in figure 2.50. Here any effects of other equipment including ultra-fast microwave switch, attenuators, cables, and the TWT amplifier were excluded by proper calibration procedures. For these microwave measurements, the bulk diamond sample

was in place on top of the device. In order to match the refractive index between the air and the quartz cover slip substrate, small amount of immersion oil was applied as well.

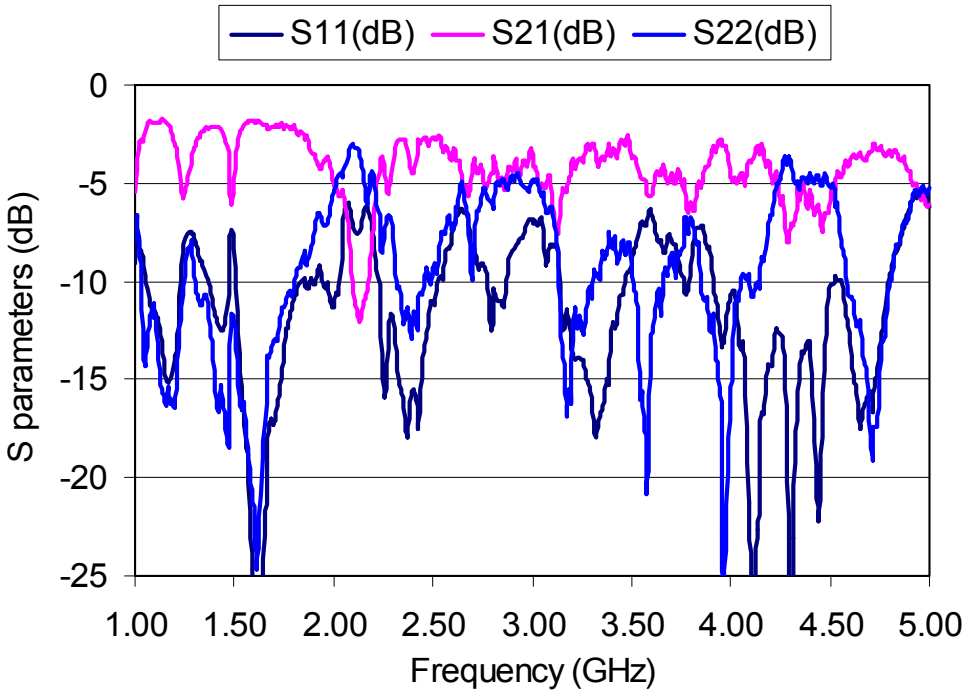

Figure 2.50 Measured scattering parameters of mounted devices using a vector network analyzer were plotted.

At around 3GHz, S11 is about -6.7dB, and S21 is about -4.6dB, so that about 22% of the applied power to the port 1 would be reflected, and about 65% of the inserted power, would be consumed by the device. The reflection loss was higher than that of the simulation, which may be attributed to the impedance mismatch at the contacts or connectors. Transmission loss was also much higher than in the simulation. This may be attributed to the larger DC resistance (~3 times larger than that of simulation structure), or some other loss, which could not be efficiently included in the simulation.

In summary of this section, co-planar microstriplines with narrow wires and gradient coils were designed, fabricated and tested for further experiments. Fabricated co-planar microstriplines will be used to achieve fast spin manipulations of NV defects in diamond, and gradient coils together with microstirplines will be used to spectrally resolve single electron spins of NV defects located within the same focal volume of the high numerical aperture objective lens.

CHAPTER III

ONE DIMENSIONAL ELECTRON SPIN IMAGING EXPERIMENTS FOR SINGLE SPIN DETECTION AND ULTRA FAST RABI NUTATION EXPERIMENTS FOR FAST SPIN MANIPULATION

A. Single Electron Spin Resonance Imaging Using a Magnetic Field Gradient

As discussed in the previous chapter, a high magnetic field gradient can be produced by the current flowing through the fabricated copper wires of micrometer size. This non-uniform magnetic field can induce non-uniform Zeeman splitting in the magnetically equivalent spins, if they are separated in radial distance from the wire center.

In this section modified CW ESR experiments using a magnetic field gradient are presented, and results are discussed.

1. Preliminary Experiments

Due to the crystal structure of the diamond as shown in figure 2.8 in chapter II, the quantization axis of the NV defects can be in 4 different orientations with respect to the external magnetic field. Since it was suggested that the diamond sample in the current experimental setup has its surface oriented parallel to the [111] direction, the orientations of the NV defects can be easily identified by using an external magnetic field, whose direction is known. A schematic diagram of the experimental setup is shown in the figure 3.1.

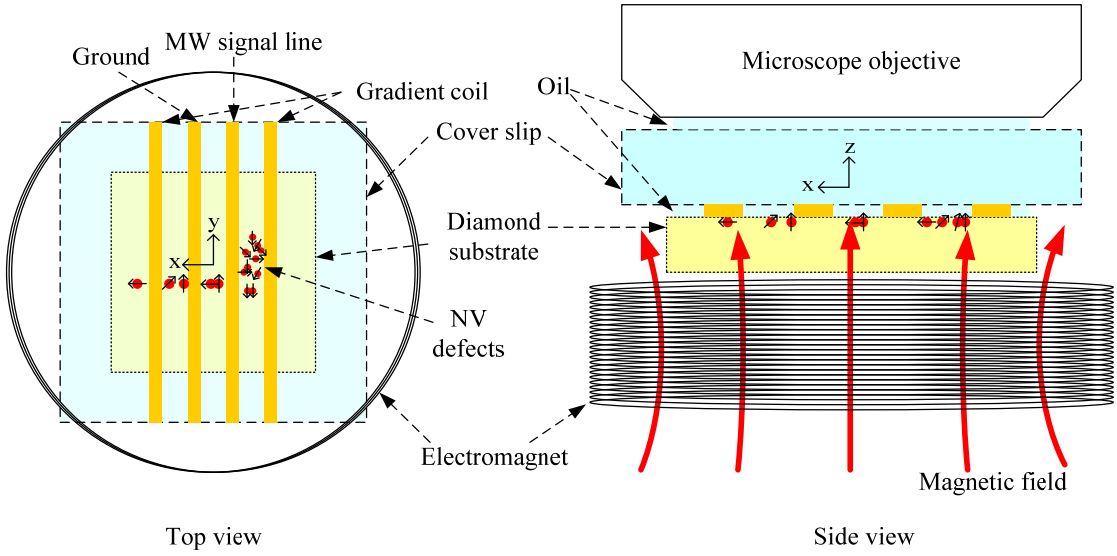

Figure 3.1 Schematic diagram of the experimental setup. External magnetic field is in z axis.

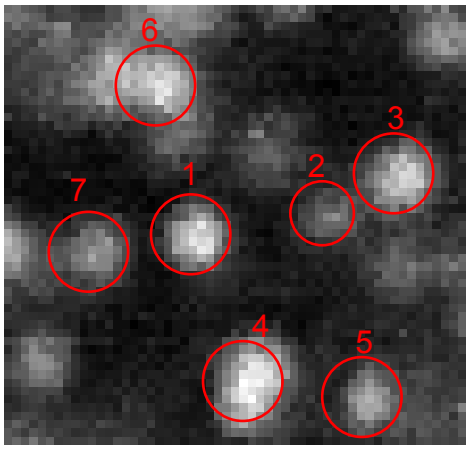

Figure 3.2 Fluorescence image of NV defects in diamond. Defect sites are named NV#1- NV#7 as indicated in the figure. NV#1 is a single defect, and others are multiple defects.

Fluorescence image was obtained by the laser scanning confocal fluorescence microscope as shown in figure 3.2.

Since the effective magnetic field strength along the quantization axis of the NV defects depends on the angle between the NV orientation and the external magnetic

field, the electron Zeeman splitting of the transition energies will also depend on the angle. Pulse mode ESR experiments were performed on the defect sites with a weak external magnetic field of about 18Gauss in the [111] direction and the experimental data is shown in figure 3.3.

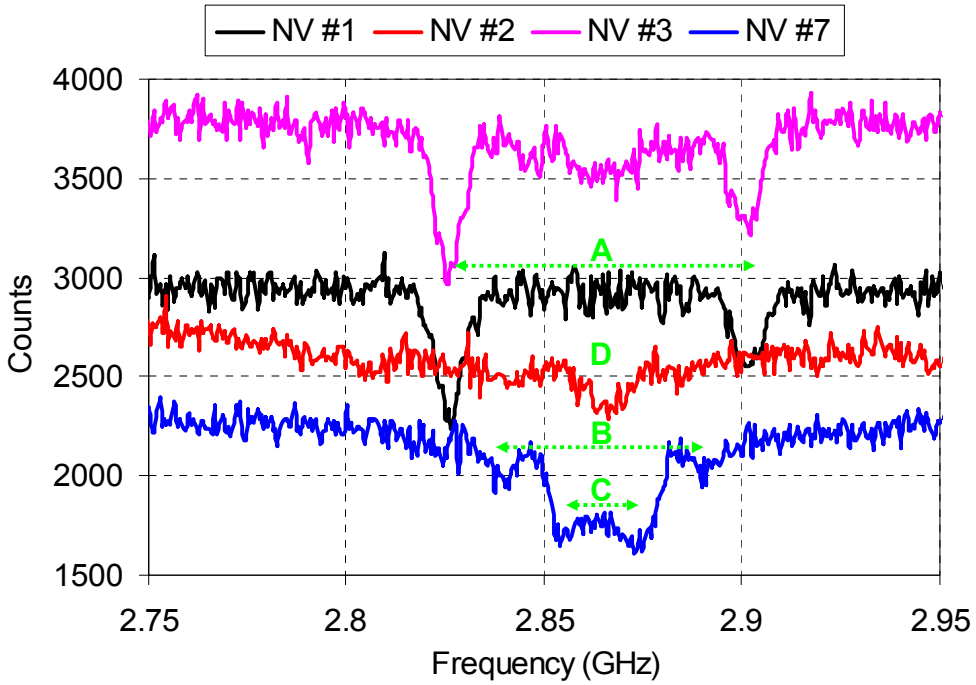

Figure 3.3 ESR spectrum of NV defects sites with external magnetic field of about 18 Gauss was applied along the z axis. Orientations 'A', 'B', 'C' and 'D' are indicated in the plot.

NV defect site #1 shows a splitting of 76MHz, which is named as orientation 'A'. Site #2 shows two different splittings, i.e. zero splitting, named as 'D', and a splitting of 51MHz, named as 'B'. Site #3 shows a splitting of 76MHz, i.e. orientation 'A', and zero splitting, i.e. orientation 'D'. Site #7 shows a splitting of 51MHz, i.e. orientation 'B', and a splitting of 19MHz, named as 'C'. In total 4 different orientations

of the NV defects were identified. NV sites #4, #5 and #6 showed orientations of A and D, A and D, and A, respectively, but data were not shown.

Since the external magnetic field was supposed to be aligned along the [111] direction, all other 3 orientations should be magnetically equivalent. However, all 4 possible NV orientations were observed in the experiments. This was attributed to the fact that external magnetic field could be misaligned at a small angle with respect to [111] direction and/or the fact that small residual magnetic field components in x or y directions could exist.

In order to find the exact transition frequencies at a given magnetic field strength, further experiments on the NV defects with orientation 'A' were carried out with a small frequency sweep range. When a current of 0.53A was applied to the electromagnet, transition frequencies of 2.834GHz and 2.9015GHz were measured. At 1.0A the transition frequencies were 2.80872GHz, and 2.93028GHz. And at 1.5A, 2.77646GHz and 2.96055GHz. As the current on the electromagnet increases linearly from 0.53A to 1.0A and 1.5A, the splitting increases almost linearly from 67.5MHz to 121.6MHz and 184.1MHz, respectively, i.e. the splitting depends almost linearly upon magnetic field intensity.

Using the Hamiltonian discussed in chapter II the angle of orientations, e.g. orientation 'A', with respect to the external magnetic field was calculated as shown in figure 3.4, which shows a good agreement with theory. Therefore, the orientation 'A' is almost parallel to the axis of the external electromagnet, and thereby the diamond

sample is indeed in the (111) plane. The other three magnetically in-equivalent splittings may be due to residual magnetic field components in the x or y directions.

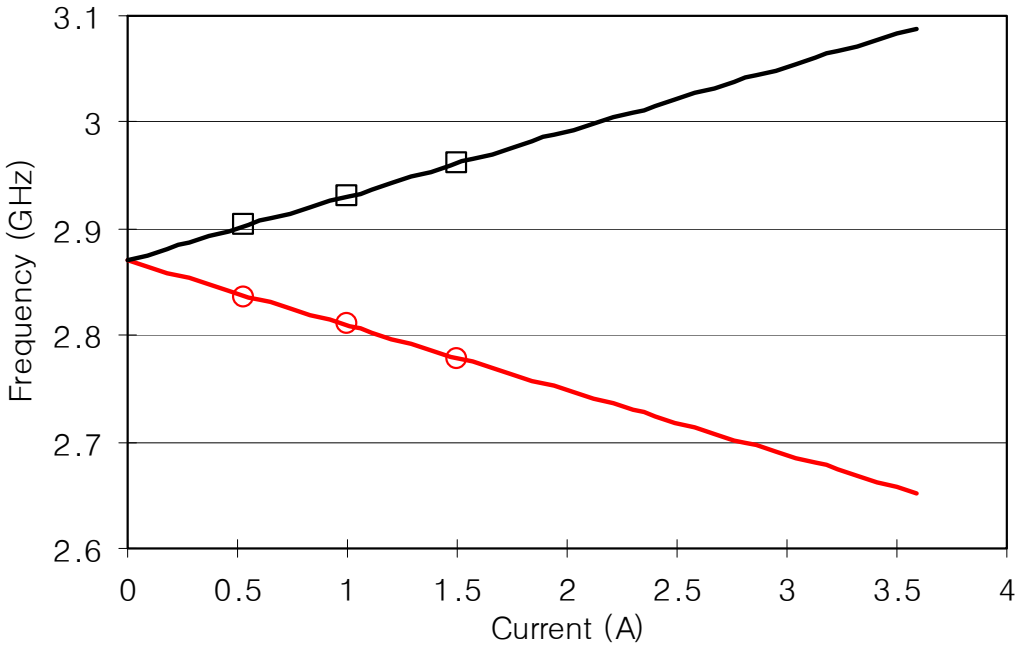

Figure 3.4 ESR transition frequencies as a function of current applied to the external electromagnet. Solid lines are numerical solutions of the Hamiltonian with uniform magnetic field applied at 0 degrees from the NV quantization axis, squares and circles are for the measured frequencies on NV #1 with orientation 'A'.

In order to demonstrate proof of principle experiments for single electron spin imaging using a magnetic field gradient, it would be more favorable to investigate NV defect sites where 2 or 3 defects are present within the focal volume of the diffraction limited spot, preferably with orientations magnetically equivalent with respect to the external magnetic field, e.g. orientation 'A'.

Defect sites of two or three NV defects were selected after the photon antibunching experiments, and then their orientations were identified by the pulse mode

ESR experiments while a uniform magnetic field was applied. Once their orientations were identified, a defect site was selected for the single spin imaging experiments.

A fluorescence image of NV defects located between the microwave signal line and a gradient coil was obtained as seen in figure 3.5

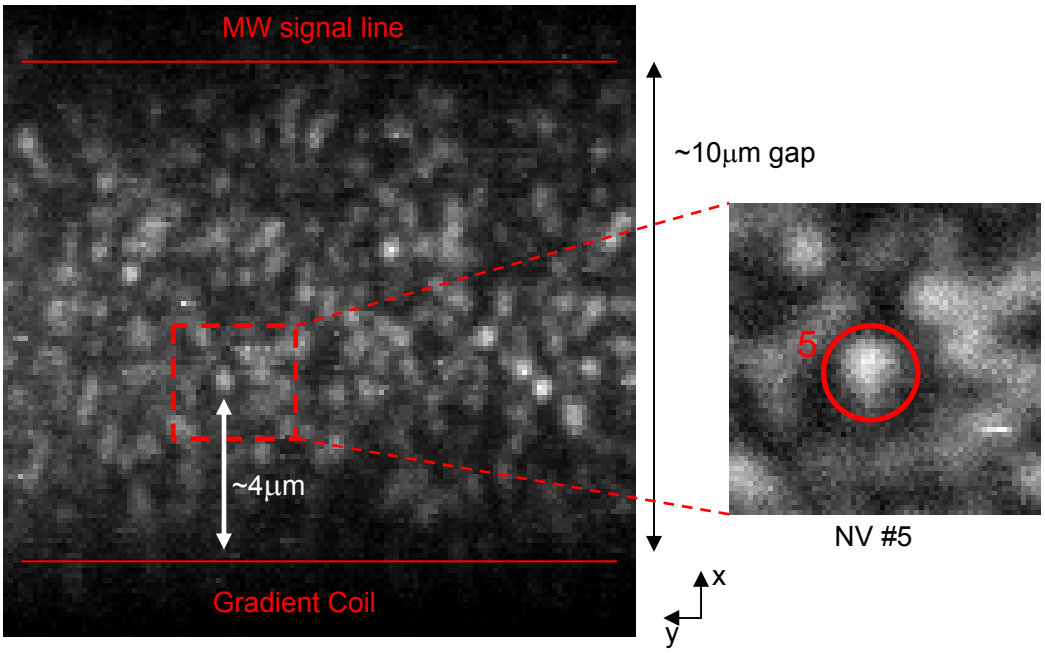

Figure 3.5 Fluorescence image of NV sites between microwave signal line and one of the gradient coil lines. NV #5 was located at x=9.6μm, and z=-2.6μm from the center of the gradient coil. Distance in the x-direction was measured by using the wire dimension as a reference, and distance in the z-direction was measured by optical distance divided by the refractive index of the oil.

After photon antibunching experiments were performed on NV sites in this area, 40 NV sites were pre-selected within the scanned area, whose antibunching dip was between 0.7 and 0.9. The $g^2(\tau)$ measurements on NV site #5 compared to that of a single NV defect was shown in figure 3.6. The antibunching dip for NV site #5 was 0.85, but depending on the measurement conditions, such as optical power or location of

the laser spot, it varies from 0.76 to 0.9. From equation (2.16), it was suggested that there may be three or more defects present in this site.

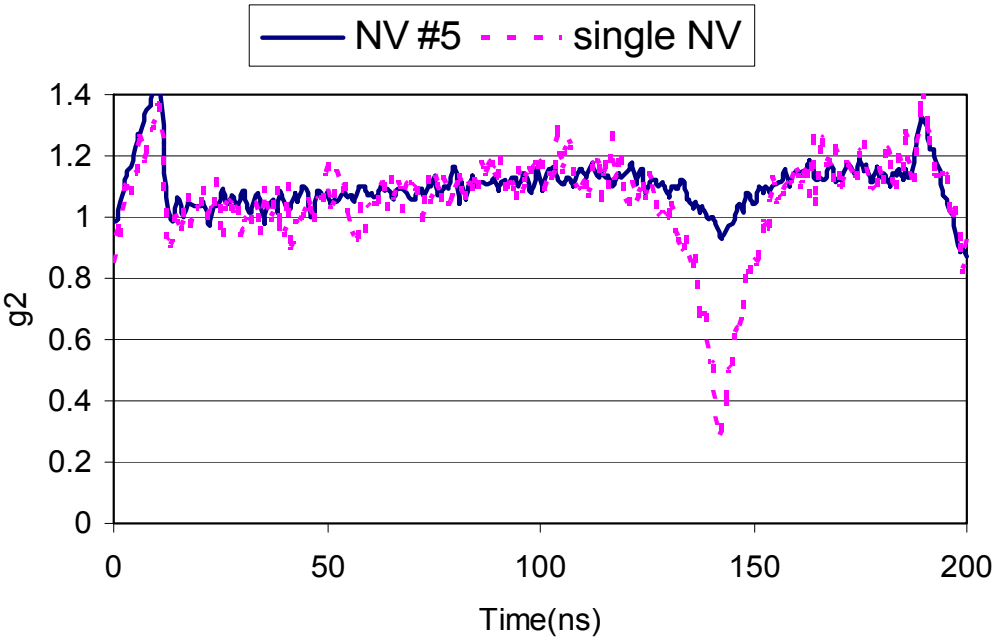

Figure 3.6 Photon antibunching experimental data on NV defect site #5 with comparison of a single NV defect. Background noise level at a given optical pumping power (~0.9mW) is 0.28, and the antibunching dip of NV defects site #5 is 0.85.

Once NV defect sites were selected after photon antibunching experiments, pulse mode ESR experiments with a uniform magnetic field were carried out in order to identify their orientations with respect to the external magnetic field.

Among forty NV defect sites NV site #5 was of particular interest, because it shows linear dependence of the splitting upon uniform magnetic field strength, which is applied along the z axis as shown in figure 3.7. As the uniform external magnetic field strength increases, the splitting in the ESR spectrum increases linearly, but the full width

at half maximum doesn't change. This may strongly suggest that NV defects present in site #5 have magnetically equivalent orientations, i.e. orientation 'A'.

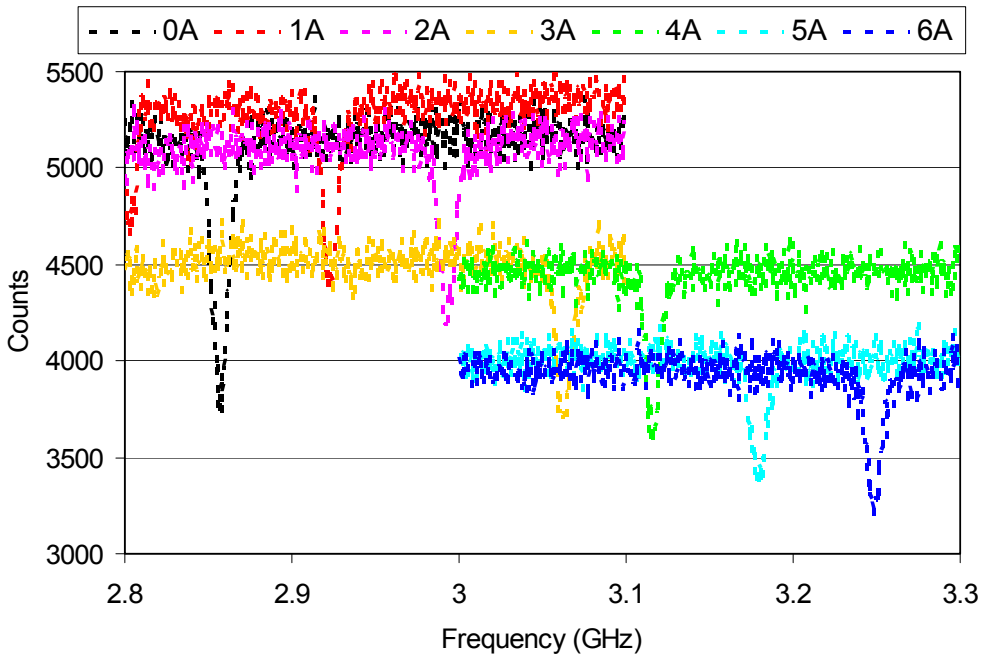

Figure 3.7 ESR spectrum of NV defect site #5 with various external magnetic field strengths, which was indicated as the current flowing in electromagnet coil. MW π-pulse of 110ns was used, FWHM is about 9.5MHz.

There is still a possibility that NV defects oriented in different directions become magnetically equivalent if uniform external magnetic field is applied along the bi-sect angle of the two NV quantization axes. In this case they will show the same splitting even though they are oriented in different directions. In order to remove these orientation ambiguities, further experiments were carried out while the uniform magnetic field was rotated in the y-z plane and x-z plane. This time the electromagnet was replaced by a permanent magnet, which was mounted on the rotational stage. At 0 degrees, the uniform magnetic field was assumed to be along the z axis.

ESR experiments were carried out while a uniform magnetic field was applied at various angles in y-z plane, and the spectrum is shown in figure 3.8. At a given magnetic field at 0 degrees, a weak spectrum with smaller amplitude is present together with a strong spectrum. It appears that the weak center was previously not excited efficiently at smaller optical power (~0.6mW), but at larger optical power of 0.9mW, this weak center became illuminated and gave a weak ESR signal. As the magnetic field angle increases the two distinct splittings becomes close to each other until they were overlapped at about 52 degrees. After that they exchanged their positions as seen in the spectrum of the 62 degree case.

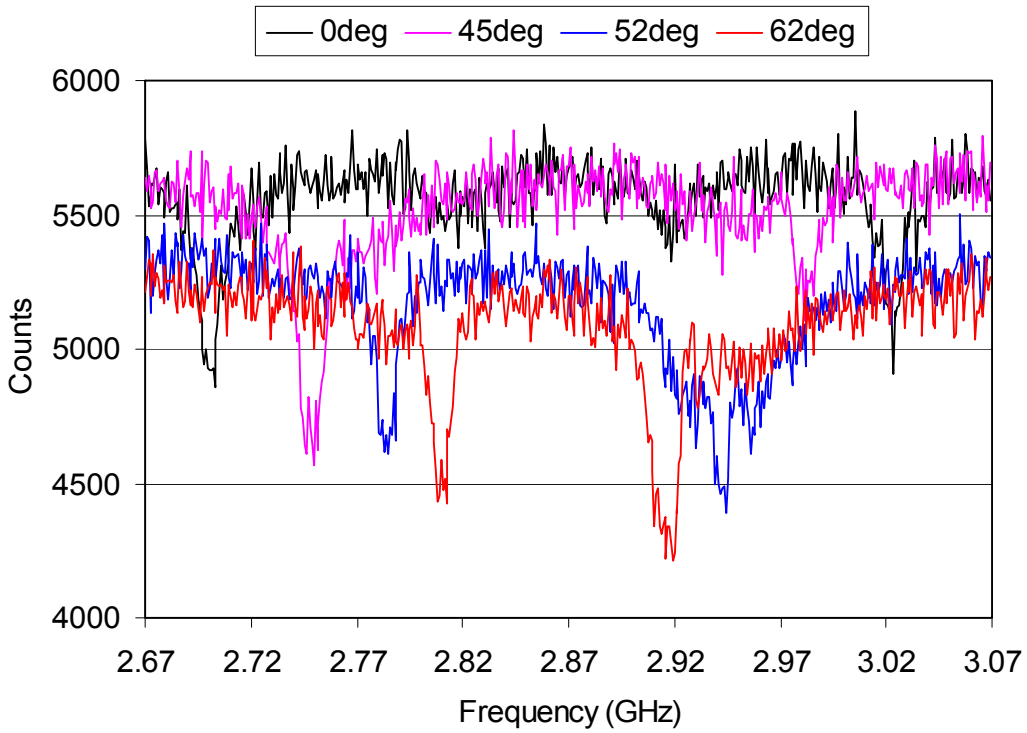

Figure 3.8 ESR spectrum of NV #5 with uniform magnetic field applied at an angle in the y-z plane. Optical power was about 0.9mW.

Next the uniform magnetic field was rotated in the x-z plane, and ESR spectrum is shown in figure 3.9. Due to the configuration of the rotational stage the location of the magnet had to be adjusted to get proper angles. As the angle increases, the two distinct splittings became smaller, but no more than two splittings were observed.

From these experiments it is concluded that NV defect site #5 is composed of a few defects with only two distinct orientations with respect to the external uniform magnetic field.

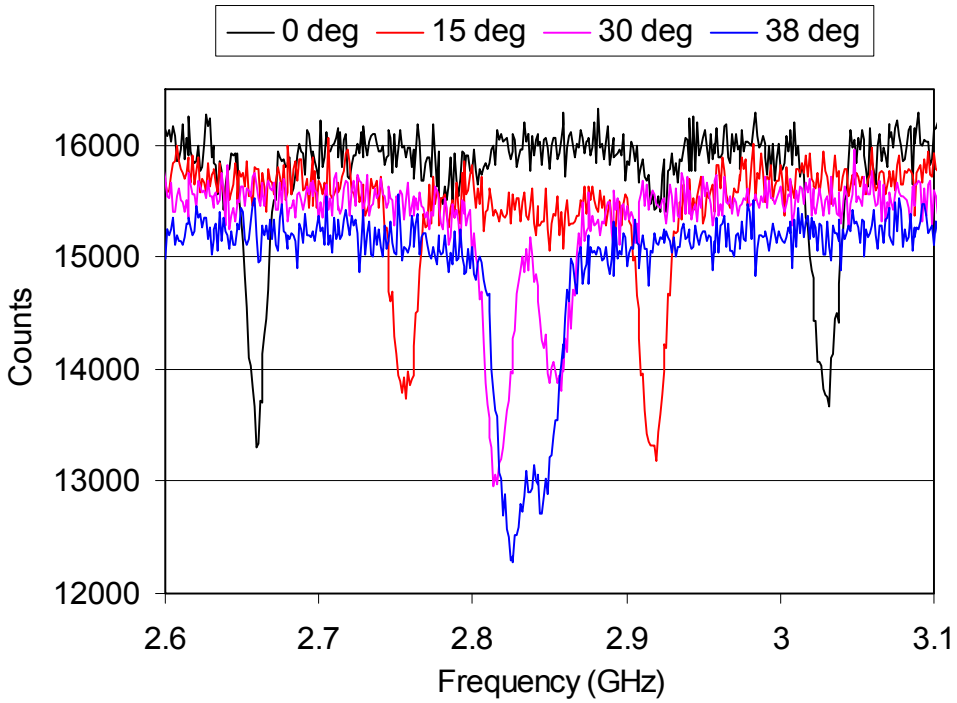

Figure 3.9 ESR spectrum of NV #5 with uniform magnetic field applied at an angle in the x-z plane. Optical power was about 0.9mW.

2. ESR Experiments for Single Spin Imaging Using a Magnetic Field Gradient

As discussed above, if an external magnetic field is applied along the bi-sect angle between two distinct orientations, these orientations become magnetically equivalent, and they can not be distinguished by the external uniform magnetic field.

Since NV site #5 is roughly located at x=9.6μm, z=-2.6μm, the magnetic field induced by a gradient wire may not be orientated in the z axis at this location. Therefore, it is necessary to check the orientations of the NV defects in site #5 with respect to the magnetic gradient field.

Though the magnetic gradient field is a function of the distance from the center of the gradient wire, the resolving power of this gradient may be negligible if the magnetic field is not oriented in the correct direction to give a large Zeeman shift. ESR experiments were carried out with a small current applied to the gradient wire in the absence of the external uniform magnetic field. Exact transition frequencies with respect the current through the gradient wire were measured as shown in table 1.

Table 1. ESR transition frequencies were measured with respect to the applied current along the gradient wire. Current was calculated from the voltage drop across the gradient wire with a resistance of 1.1Ω.

Current (mA)	94.5	218.2	327.3	454.5	563.6
Low frequency (GHz), m_s=-1	2.8483	2.8299	2.8170	2.7959	2.7790
High frequency (GHz), m_s=+1	2.8956	2.9126	2.9284	2.9539	2.9768

In order to find the angle between the NV quantization axis and magnetic gradient-wire field, the spin Hamiltonian was numerically solved as a function of the magnetic field strength at a given angle (θ), and the measured data was plotted together with theoretical data as seen in figure 3.10.

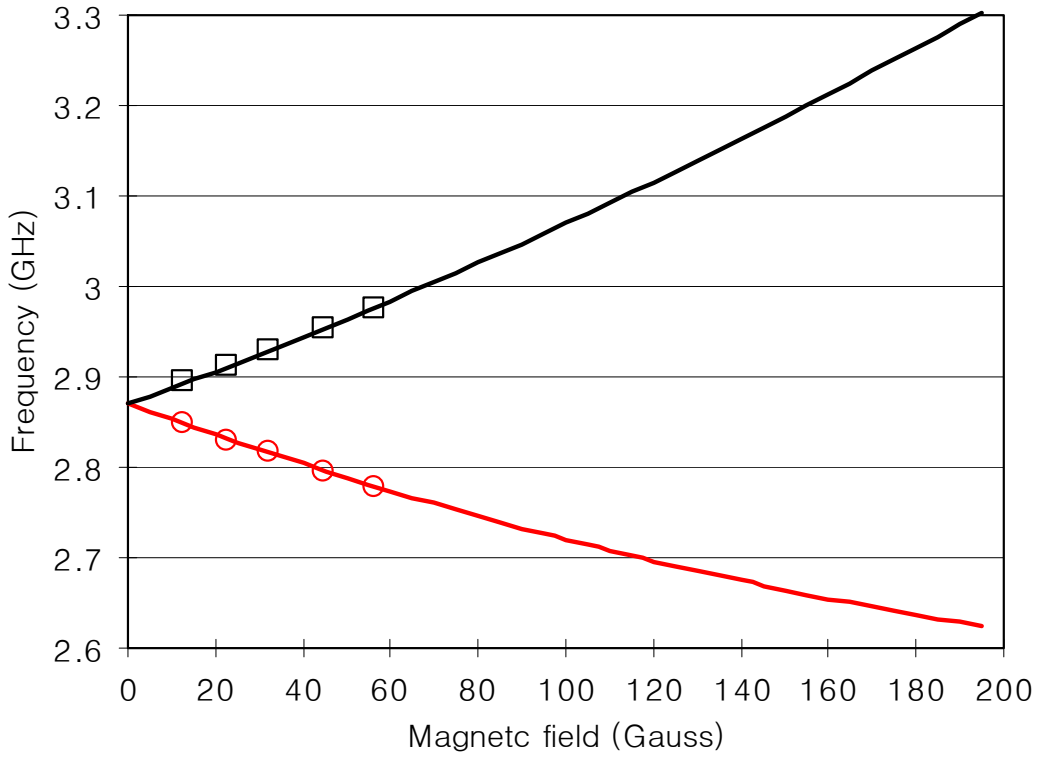

Figure 3.10 ESR transition frequencies as a function of magnetic field. Solid lines are from the theory with an angle (θ) of 51.3 degrees, squares and circles are from the measured data shown in table 1.

In the plot, the angle (θ) between NV quantization axis and the magnetic field was assumed to be 51.3 degrees, and the measured ESR transition frequencies were in good agreement with theory for this angle.

A magneto-static simulation of a thin copper wire was performed by commercially available software (Maxwell 2D, Ansoft Corp.). When 1A of current flows through the copper wire along the y axis, a spatially non-uniform magnetic field is induced around the wire and its distribution is shown in figure 3.11. In order to approximate the fabricated wire dimensions, a copper wire of 12μm by 1μm is assumed in the simulation.

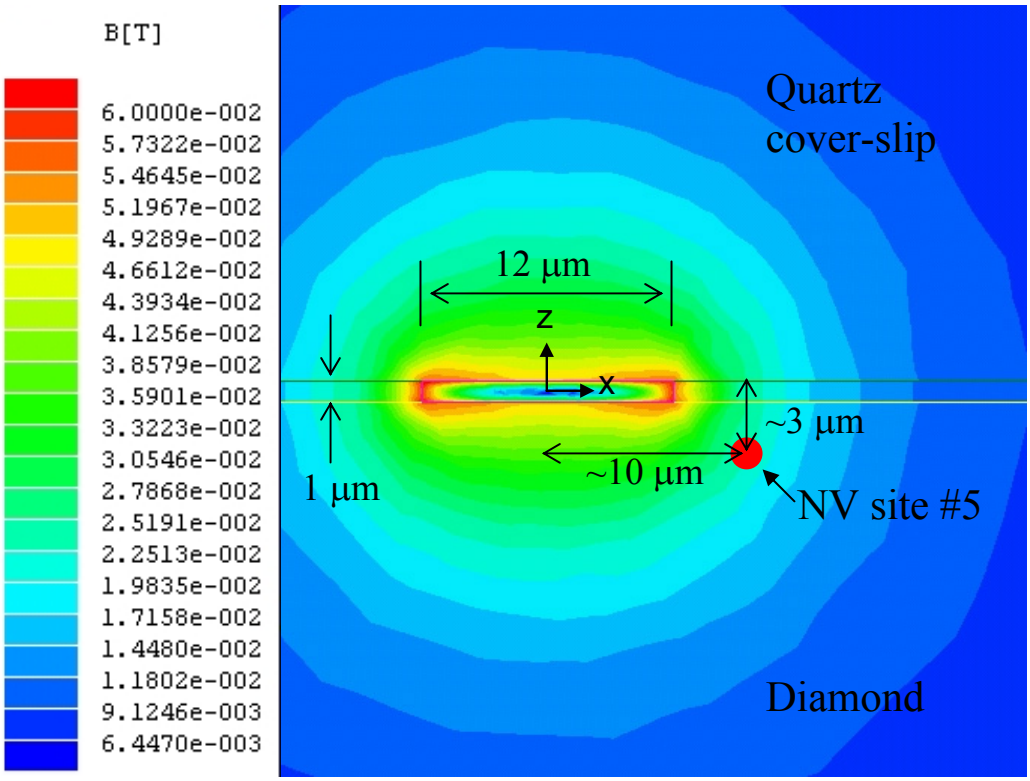

Figure 3.11 Cross-sectional view of the magnetic field distribution around the cross section of the copper wire of 12μm by 1μm. Simulation was performed with the MAXWELL 2D from Ansoft Corporation.

In the simulation quartz glass was assumed above the copper wire, and diamond below the wire. As shown in the plot, at the location of NV site #5, i.e. x=9.6μm, z=-

2.6μm, it is quite possible that the magnetic field has large angle, i.e. 51.3 degrees from the z axis, which is assumed to be the [111] direction of the crystal.

ESR experiments were carried out at higher currents through the gradient wire, and the ESR spectrum is shown in figure 3.12. At lower current, e.g. 0.4A, the ESR spectrum showed one splitting, but as the current increased to 1.2A, the ESR spectrum split into 2 components, and the splitting was about 19MHz.

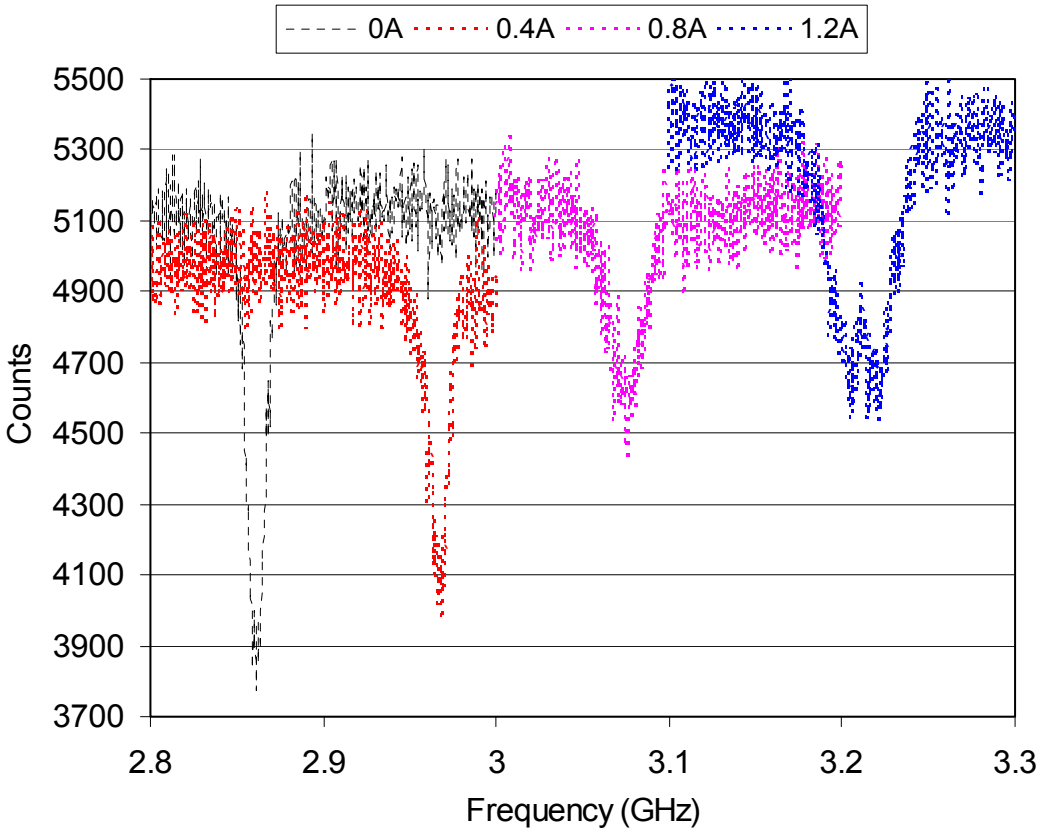

Figure 3.12 ESR spectrum was plotted with various currents applied along the gradient coil in the absence of the uniform external magnetic field.

In this spectrum, it now seems that there exists only one orientation in this site, since the frequency component with a smaller splitting that was found in the presence of

the uniform magnetic field used in figure 3.8 or 3.9 did not show up in this experiment. Therefore, it is not clear if the splitting at the high current of 1.2A originated from a large magnetic field gradient applied to the magnetically equivalent NV defects or from the two different NV orientations, which have a similar angle with respect to the magnetic field produced by the gradient wire.

Therefore, other ESR experiments were carried out with different magnetic field gradients, while a uniform magnetic field was applied along the z axis. In this way the magnetically inequivalent NV defects are always well separated by the uniform magnetic field, and only magnetically equivalent NV defects will be resolved by the high magnetic field gradient.

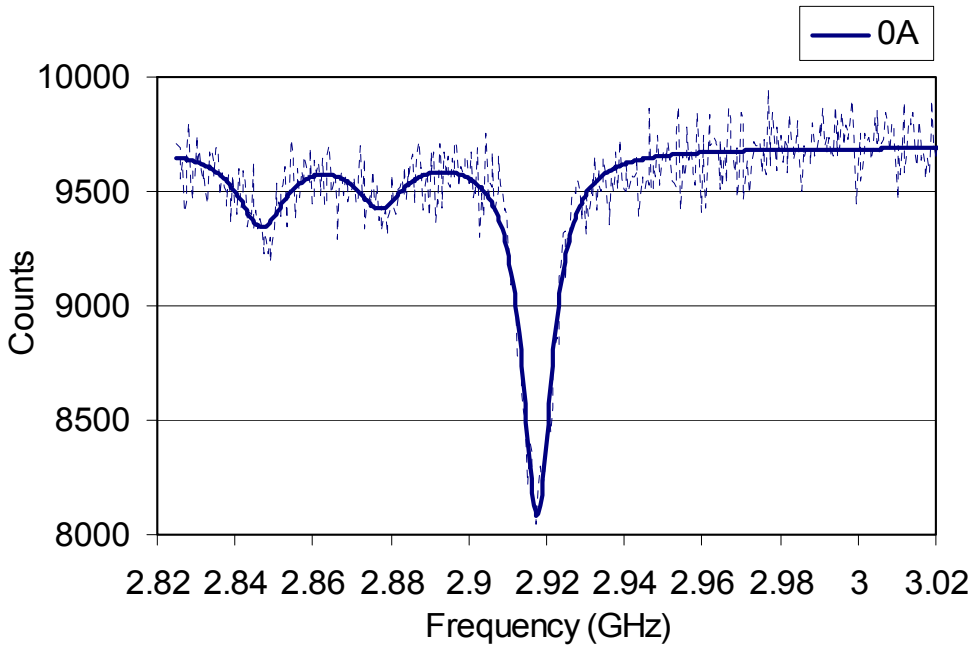

Figure 3.13 ESR spectrum of NV defect #5 with zero magnetic field gradient in the presence of the uniform magnetic field along z axis. Solid lines are fitting with lorentzian peaks model.

The two distinct NV orientations are distinguished by the uniform magnetic field, as seen in figure 3.13. Then, magnetic gradient field induced by the current through the gradient wire is applied in the presence of this uniform magnetic field.

When the current on the gradient wire is increased to 1.4A, the strong ESR spectrum became broadened, and it was no longer fitted with a single lorentz peak model. Instead three lorentz peaks were used to fit the ESR spectrum, as seen in figure 3.14. At 1.4A the frequency difference between neighboring components was about 6.96MHz and 4.23MHz, and the width of three components was about 6.7~7.4MHz.

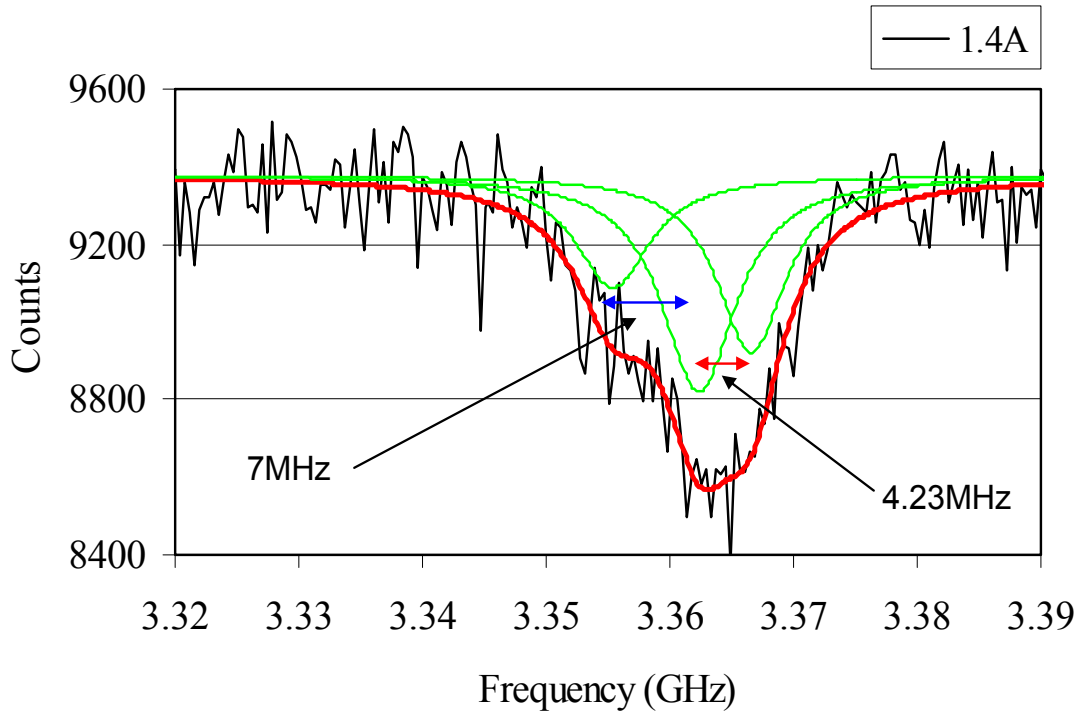

Figure 3.14 ESR spectrum of NV defect #5 with magnetic field gradient in the presence of the uniform magnetic field along z axis. Solid lines are fitting with lorentz peaks model. The current along the gradient coil was 1.4A. The frequency difference between neighboring components was 6.96MHz and 4.23MHz, respectively.

When the current increased to 1.6A, the frequency differences increased to 8.11MHz and 4.78MHz, respectively, as seen in figure 3.15. The width of each lorentz peak also increased to about 7.5~8.5MHz.

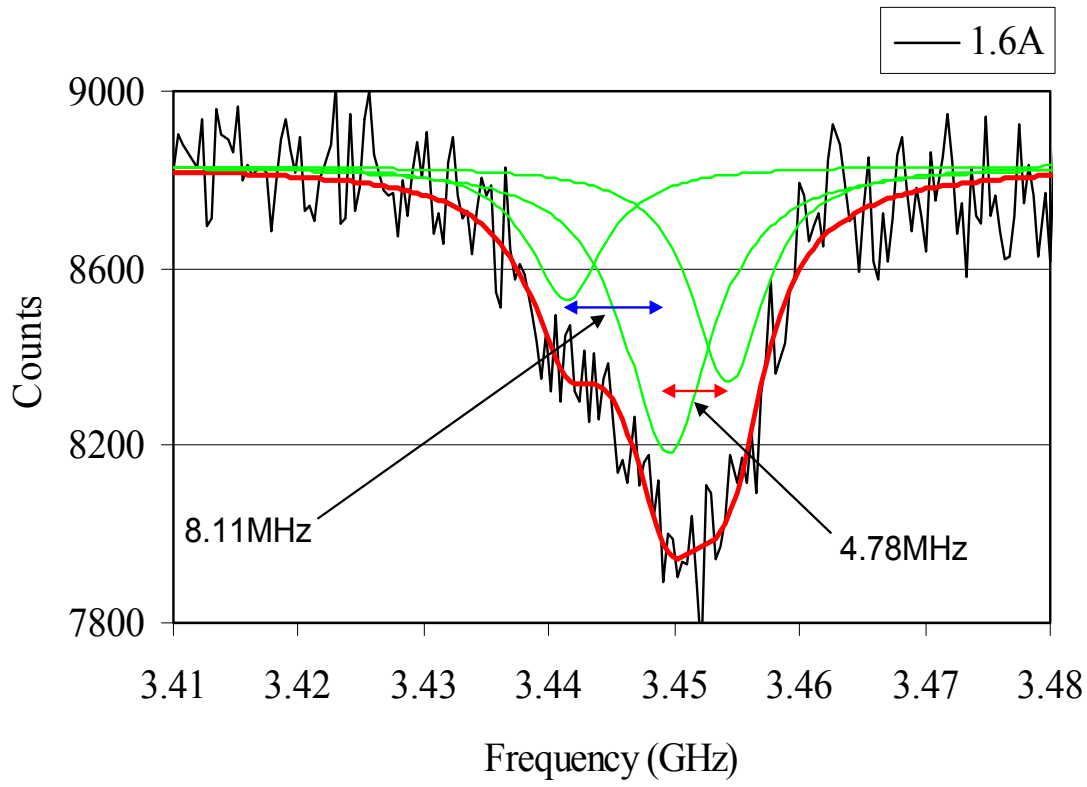

Figure 3.15 ESR spectrum of NV defect #5 with magnetic field gradient in the presence of the uniform magnetic field along z axis. Solid lines are fitting with lorentzian peak models. The current along the gradient coil was 1.6A. The frequency difference between neighboring components was 8.11MHz and 4.78MHz, respectively.

Since the two magnetically inequivalent NV spins are already spectrally resolved by the uniform magnetic field, the splittings observed in the figure 3.14 and 3.15 are certainly originating from the magnetically equivalent NV defects, which experience different magnetic field strengths due to the magnetic field gradient.

3. Results

Since the three NV defects resolved by the magnetic field gradient were not previously resolved by the uniform magnetic field alone, they should be magnetically equivalent. But the magnetic field gradient, which was induced by the current flowing through the gradient wire, split them apart in these experiments. Therefore more currents were tried as the results are summarized as follows:

At a current of 1.2A, the lines are barely split, and a computer fit with three lorentz peaks gave frequency components of 3.2769GHz with a FWHM of 8.18MHz, 3.28306GHz with a FWHM of 8.26MHz, and 3.2867GHz with 6.29MHz. At 1.4A the frequency components were 3.3554GHz with a FWHM of 7.38MHz, 3.3624GHz with a FWHM of 7.33MHz, and 3.3666GHz with 6.75MHz. At 1.6A the frequency components were 3.4414GHz with a FWHM of 7.25MHz, 3.4495GHz with a FWHM of 8.52MHz, and 3.4543GHz with 7.05MHz.

The frequency difference between neighboring components in ESR spectrum vs. the magnetic field gradient, in units of the current applied through the gradient wire was plotted in figure 3.16.

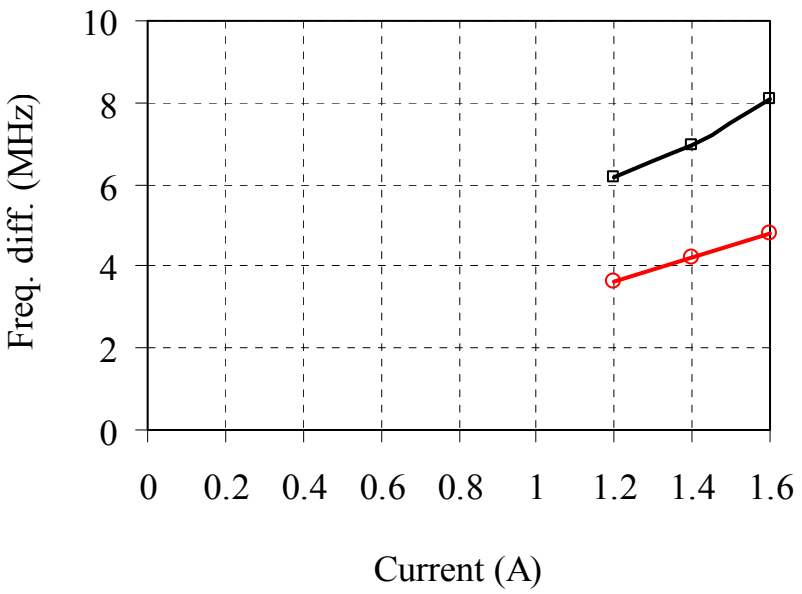

Figure 3.16 Frequency differences between neighboring frequency components in ESR spectrum was plotted as a function of the current, which induced the magnetic field gradient around the gradient coil. Lines with squares are from the lower two frequency components, and lines with circles are from the higher two frequency components.

As seen in the plot, the splitting of the frequency components showed almost linear dependence to the current along the gradient coil. It seems that the current is still small enough that the quadratic term is negligible.

Due to heat dissipation of the gradient coil, higher current was not able to be applied. Instead another experiment, i.e. electron spin echo envelope modulation experiments, were carried out to improve the spin imaging resolution. Generally, a narrow ESR transition line width can be achieved in the spin echo experiments, and so we can achieve higher resolution. This will be discussed in the following section.

B. Electron Spin Echo Envelope Modulation Experiments for Single Spin Imaging Using a Magnetic Field Gradient

As briefly mentioned in the previous chapter, spin echo experiments can de-couple any spin dephasing caused by the imperfect external magnetic field or the local environments, if the external fields and local environments do not change in the time scale of the experiments. Therefore the spectral line width of the spin transition becomes narrower than that of CW ESR, and spin-dephasing is solely due to the T_2 relaxation. Therefore, higher resolution can be achieved.

In this section, electron spin echo envelope modulation experiments using a magnetic field gradient are presented, and the experimental results are discussed together with the results from the CW ESR experiments.

1. Preliminary Experiments

In order to perform spin echo experiments it is necessary to know the exact spin transition frequency at a given magnetic field, and the exact pulse width for the microwave $\pi/2$-pulse and π-pulse at a given microwave power. The electron spin transition frequency can be measured by the CW ESR experiments. The pulse width at a given microwave power can be determined by the Rabi nutations experiments.

ESR experiments were carried out on the NV site #5 in the presence of a uniform magnetic field of about 20Gauss along the z axis, and the spectrum is shown in figure 3.17.

It was concluded in the previous section that there are two distinct NV orientations in site #5 that are split out with uniform magnetic field in the z direction.

Therefore the uniform magnetic field was kept constant, and the frequency component of around 2.92GHz was selected for the rest of the ESEEM experiments. From the ESR spectrum with a narrower frequency sweep range, the transition frequency was determined to be 2.9262GHz at the given uniform magnetic field strength.

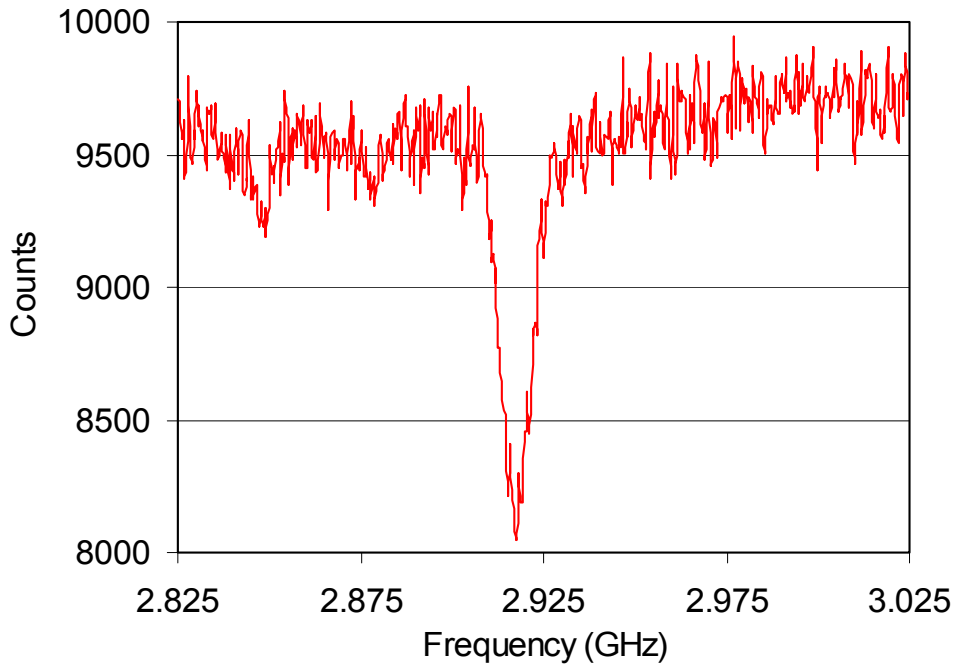

Figure 3.17 ESR spectrum of NV site #5 in the presence of the weak uniform magnetic field of about 20Gauss in the z direction. Two different NV orientations are separated by the uniform magnetic field. ESR transition line of about 2.92GHz was selected for the rest of the experiments.

Once the exact ESR transition frequency was measured, electron spin Rabi nutation experiments were carried out according to the experimental procedures described in figure 2.24, and the experimental data is shown in figure 3.18. The

microwave frequency was fixed at 2.9262GHz, and the microwave power was kept constant at 2dBm, which was measured at the microwave source output. At the given microwave power the Rabi nutation period was about 100ns, and the corresponding microwave π-pulse width was 50ns.

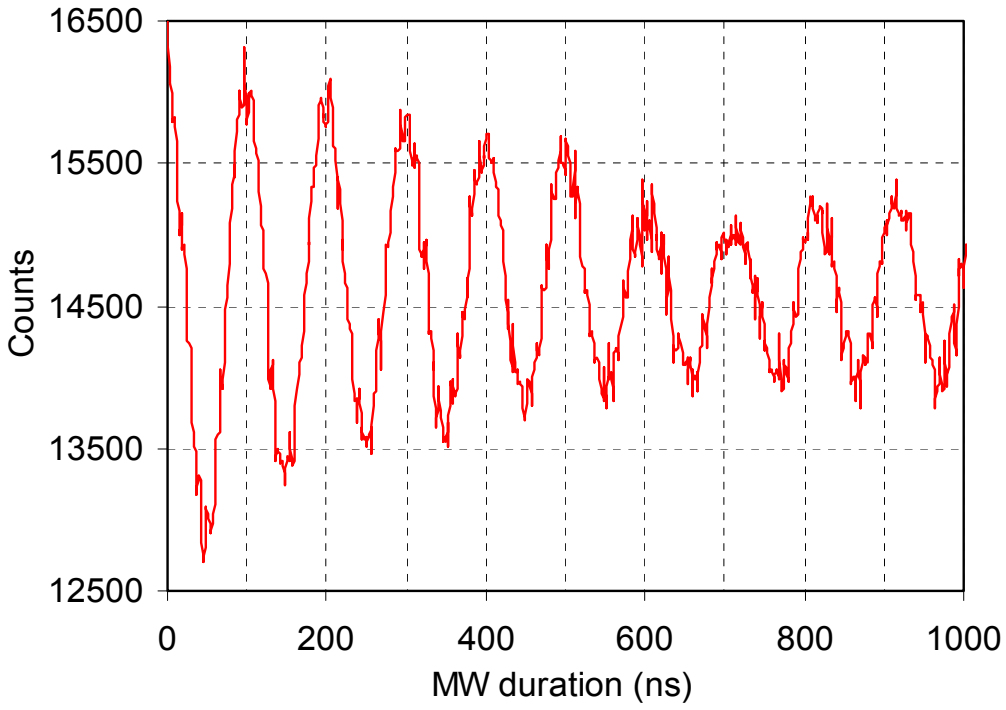

Figure 3.18 Rabi nutations of the electron spin. MW frequency was 2.9262GHz, and microwave power was 2dBm, which was measured at the microwave source output.

Once the Rabi nutations period was measured at a given microwave power, electron spin echo experiments can be carried out according to the experimental procedures described in figure 2.26.

From this data, a Rabi nutation period of 100ns was used to determine the width of the microwave pulses, i.e. π/2-pulse of 25ns and π-pulse of 50ns. The first waiting

time was set to be 250ns, and the second waiting time was varied from 100ns to 400ns with an increment of 1ns. Experimental data for the electron spin echo together with simulation data is shown in figure 3.19.

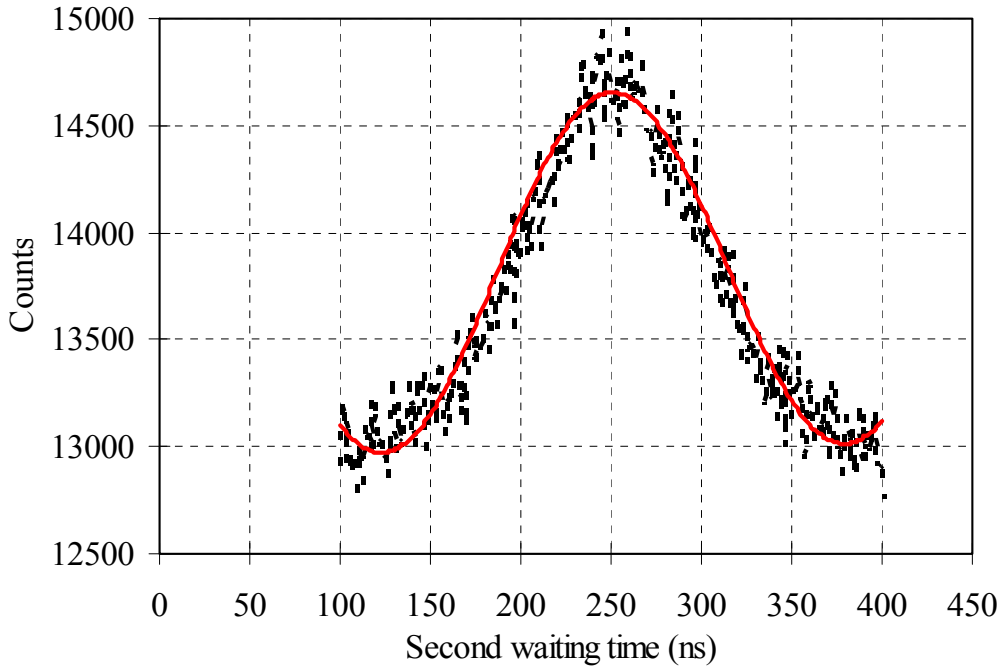

Figure 3.19 Electron spin echo of the NV #5 with Rabi nutation frequency of 10MHz, and first waiting time of 250ns. Dotted line and solid line are for experimental data and simulation data, respectively.

As expected from theory, the spin echo signal has a maximum when the second waiting time was 250ns, which was equal to the first waiting time. Equations (2.32) and (2.37) were used for the simulations. To be consistent with the experimental conditions the Rabi frequency in the simulation was set to be 10MHz when microwave pulses were being applied during the $\pi/2$-pulse and π-pulse, but it was set to be 0MHz during the first waiting time and the second waiting time. The simulation agrees quite well with the

experimental data when a detuning frequency of 3.9MHz was added to the simulation. In order to fit the simulation with experimental data, the amplitude and base-line of the simulation were adjusted.

As shown in the electron spin echo experiments, electron spins were efficiently re-phased when the second waiting time was equal to the first waiting time, since they are both smaller than the spin dephasing time, i.e. T_2. In this way any static local magnetic inhomogeneities can be efficiently de-coupled.

Electron spin echo envelope modulation experiments using a magnetic field gradient were then carried out for single electron spin imaging. The experiments and results are discussed in the following sections.

2. ESEEM Experiments Using a Magnetic Field Gradient

In the spin echo experiments the uniform magnetic field is kept constant. If the first waiting time is set equal to the second waiting time, but they vary simultaneously from the shortest to the longest waiting time, the envelope of the spin echo signal can be measured. In this configuration any phase advances due to the static environments will be canceled.

If the first waiting time is set equal to the second waiting time and another magnetic field is applied to the NV molecules during the first waiting time, but not for the second waiting time, then the spin precession speed during the first waiting time will be different from that of the second waiting time, and so phase advances due only to this added magnetic field will remain. If this magnetic field includes a magnetic field

gradient acting on two magnetically equivalent NV defects in the focal volume of the microscope, they will precess at a different speeds or frequencies, since they experience different magnetic fields due to the field gradient. These two frequency components may be observed as beating in the time domain signal.

Electron spin echo envelope modulation experiments can be carried out according to the following experimental procedures shown in figure 3.20.

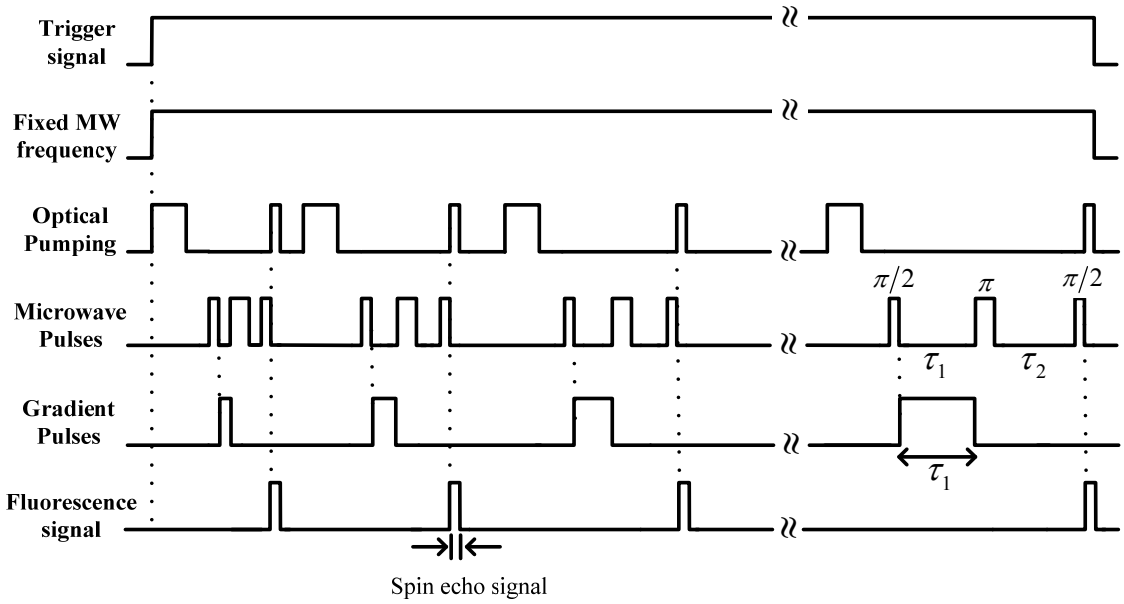

Figure 3.20 A Schematic diagram for the electron spin echo envelope modulation experiments using a magnetic field gradient. The first waiting time is set equal to the second waiting time, i.e. $\tau_1 = \tau_2$. D.C. current is flowing through the gradient wire only during the first waiting time.

In these experiments the first waiting time is always set equal to second waiting time, and the magnetic field gradient produced by the current through the gradient wire is turned on only during the first waiting time.

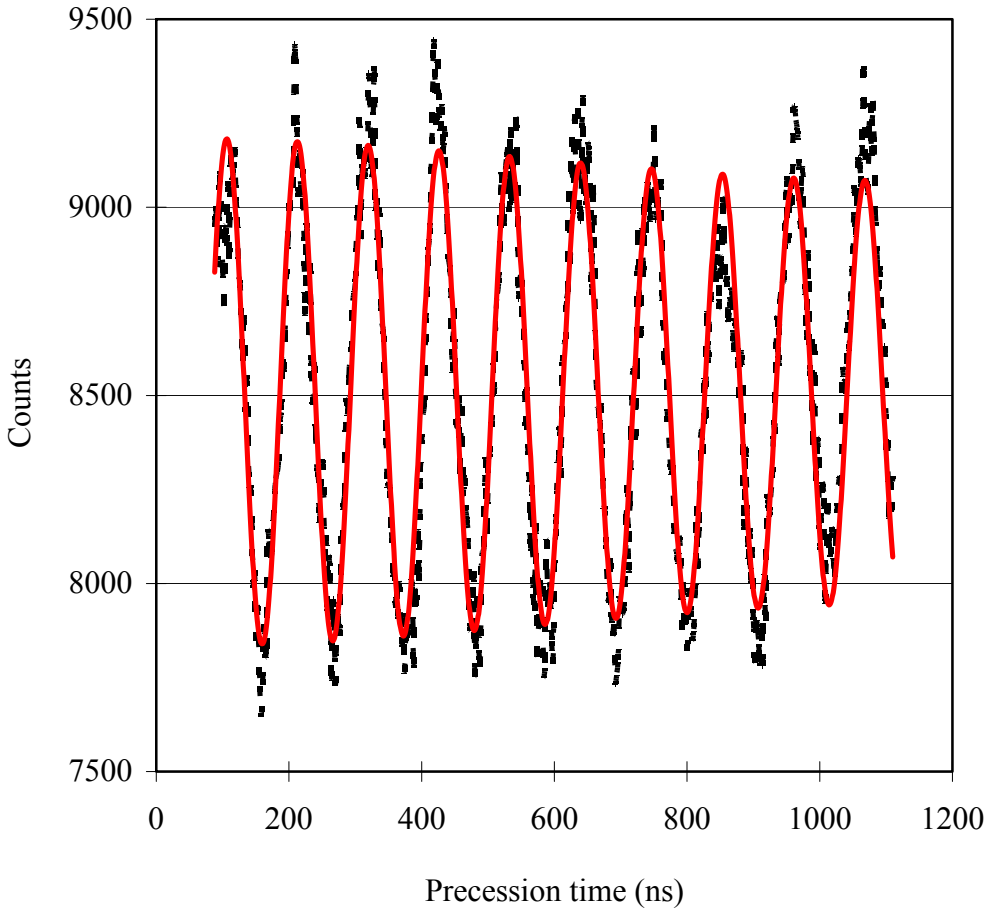

Figure 3.21 ESEEM experiments with a small magnetic field gradient which was induced by a current of 0.04A flowing along a gradient wire. The dashed line is for the experimental data, and the solid line is for the simulation data with two NV defects with a two-level atomic system.

The first ESEEM experiments were carried out while a small current of 0.04A was applied through the gradient wire. The envelope modulations are plotted together with simulation data as a function of the waiting time, i.e. τ_1 or τ_2, in figure 3.21.

For the simulation a two-level atomic system was assumed for each of the two magnetically equivalent NV defects. Equations (2.32) and (2.37) are used for the simulation. To be consistent with the experimental conditions the amplitude and base-

line in the simulation are adjusted. As expected, the current along the gradient coil produced a weak magnetic field with a small gradient. Therefore a beating of frequency components was not observed in this time scale.

When the current along the gradient coil increased to 0.2A the induced magnetic field gradient was large enough so that a beating of frequency components was observed in the time domain, as shown in figure 3.22. Because the ESR spectrum in the previous section suggested that the third component has a smaller amplitude, and so it may not contribute very much to the amplitude modulation, only two frequency components are used in this simulation.

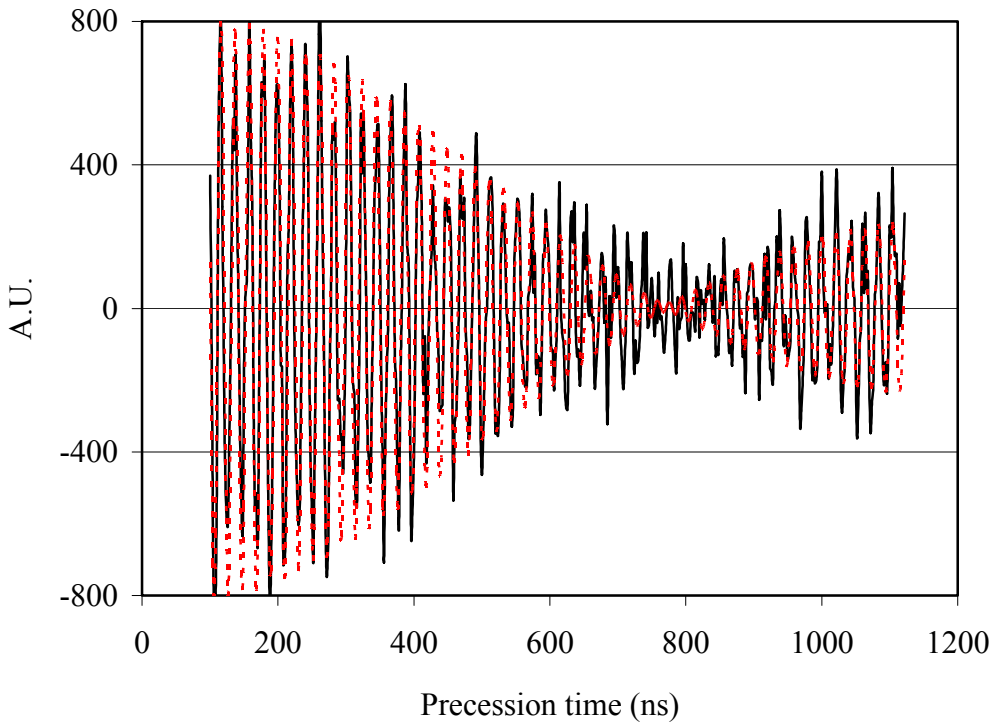

Figure 3.22 Experimental data (solid line) together with simulation data (dashed line) of ESEEM experiments on two defects in NV site #5 is plotted as a function of the waiting time duration. Current along the gradient coil was 0.2A. The first node occurs at around 820ns.

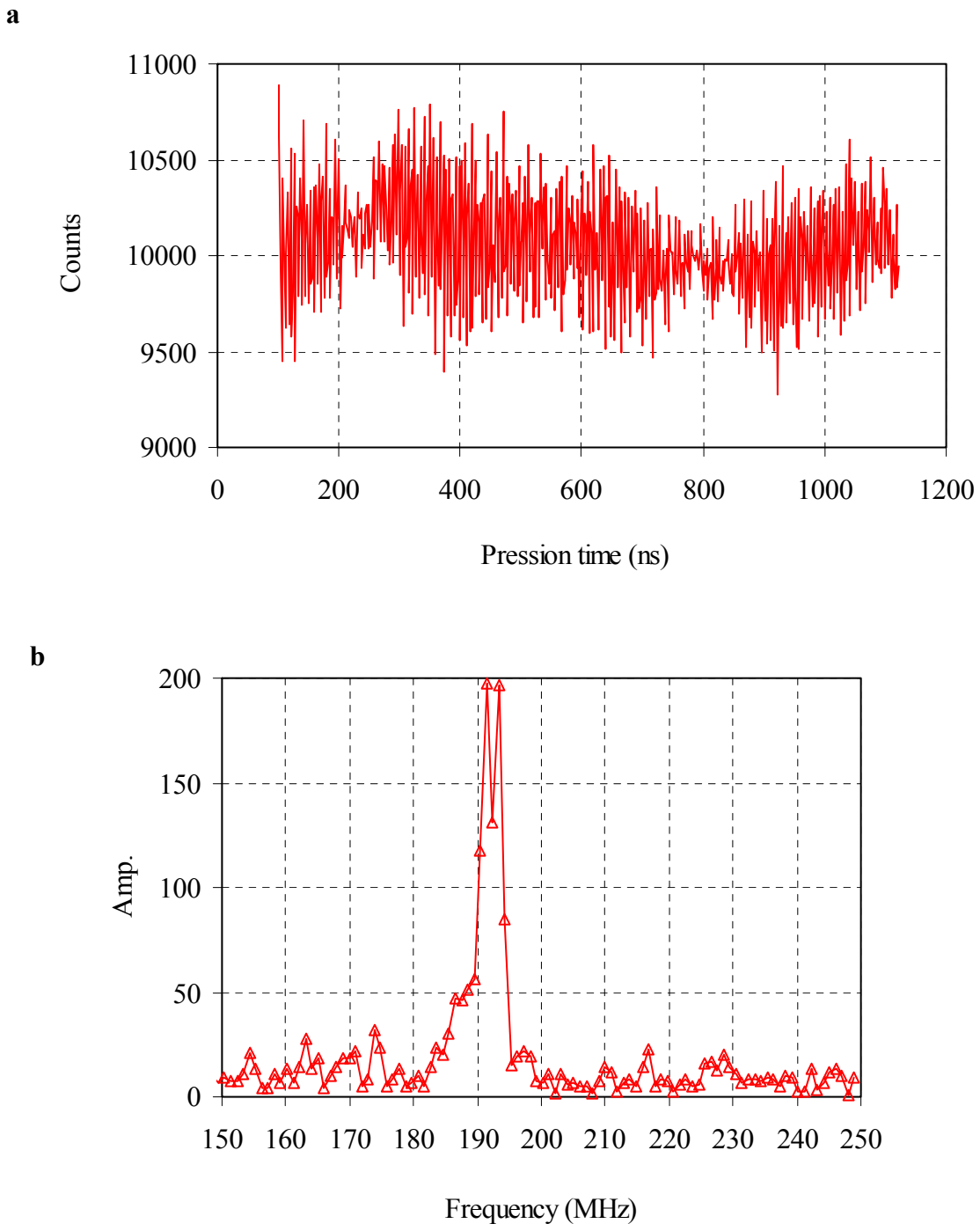

Figure 3.23 ESEEM data at a current of 0.7A applied to the gradient coil (a), and its frequency components of 193.34MHz, 191.43MHz and 187.9MHz obtained by FFT. First node occurs at about 240ns.

When a larger current of 0.7A was applied along the gradient coil, ESEEM shows strong modulations as seen in figure 3.23 (a), and its frequency spectrum verifies that there are three frequency components present in NV site #5 as seen in figure 3.23 (b). The frequency components are 193.34MHz, 191.43MHz and 187.9MHz. The third component has smaller a amplitude of about 25% of the major components, and therefore did not contribute nearly as much to the amplitude modulation.

In order to find the dependence of the beating frequency with respect to the applied current or magnetic field gradient, ESEEM experiments were repeated with various currents through the gradient wire. The experimental data are shown in figures 3.24, 3.25, 3.26, 3.27, 3.28 and 3.29.

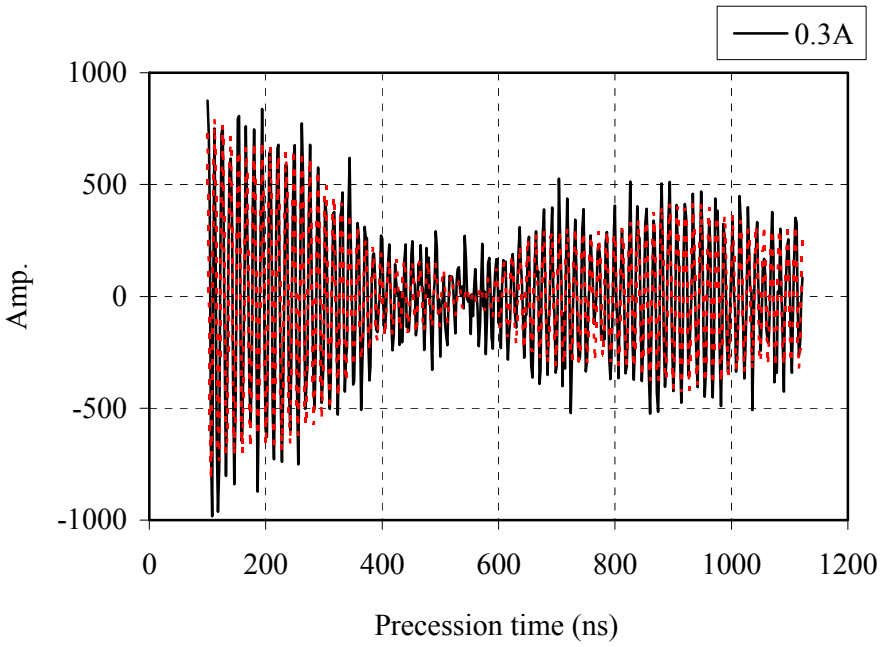

Figure 3.24 ESEEM data at a current of 0.3A applied to the gradient coil. Solid line is for the experimental data and dashed line is for the computer fitting using 3 frequency components. The two major frequency components are 73.656MHz and 72.666MHz. First node occurs at about 547ns.

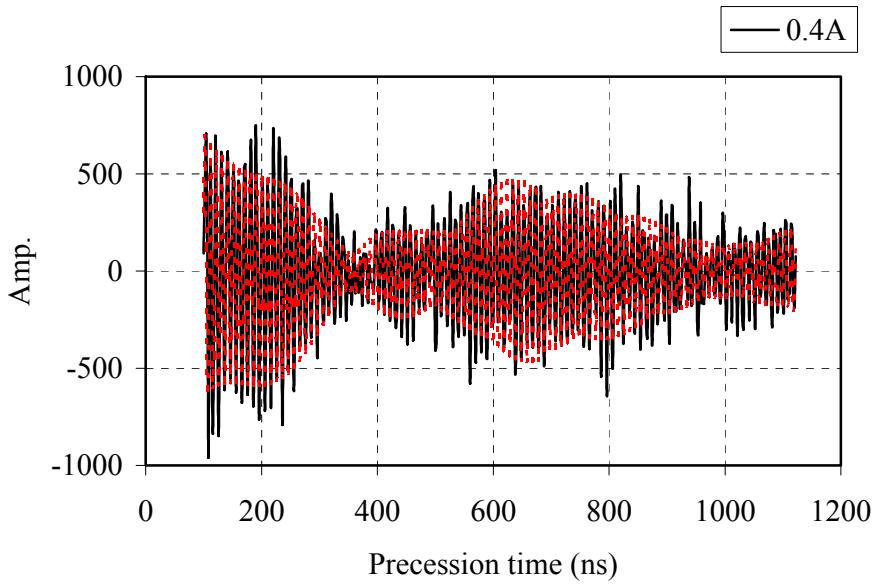

Figure 3.25 ESEEM data at a current of 0.4A applied to the gradient coil. Solid line is for the experimental data and dashed line is for the computer fitting using 3 frequency components. The two major frequency components are 100.479MHz and 99.173MHz. First node occurs at about 386ns.

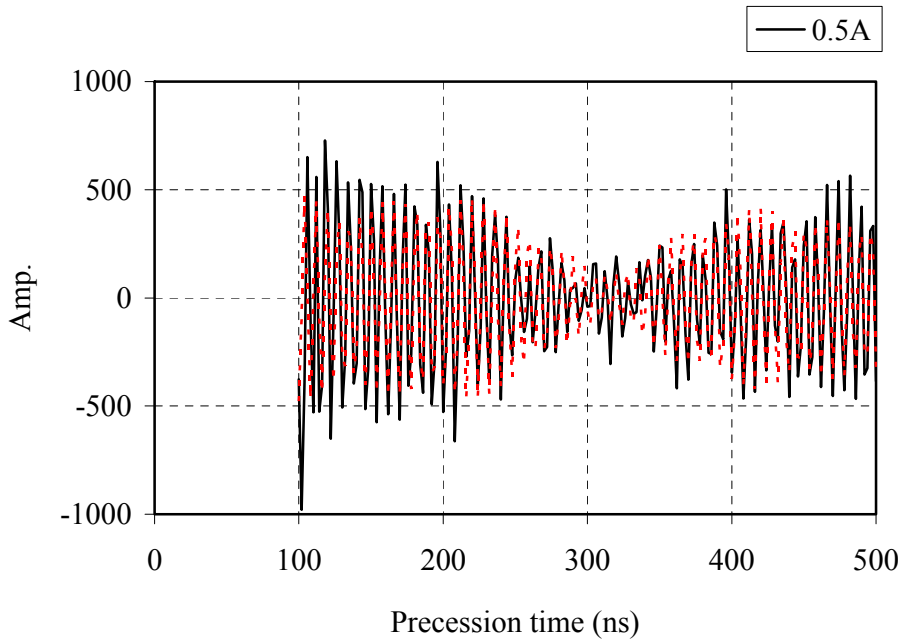

Figure 3.26 ESEEM data at a current of 0.5A applied to the gradient coil. Solid line is for the experimental data and dashed line is for the computer fitting using 3 frequency components. The two major frequency components are 129.058MHz and 127.469MHz. First node occurs at about 335ns.

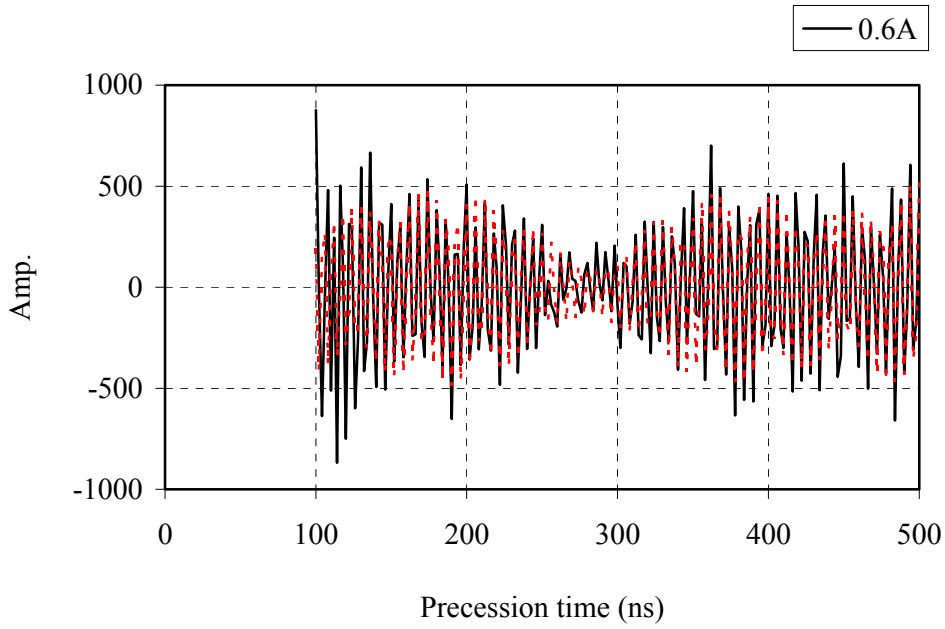

Figure 3.27 ESEEM data at a current of 0.6A applied to the gradient coil. Solid line is for the experimental data and dashed line is for the computer fitting using 3 frequency components. The two major frequency components are 159.002MHz and 157.171MHz. First node occurs at about 277ns.

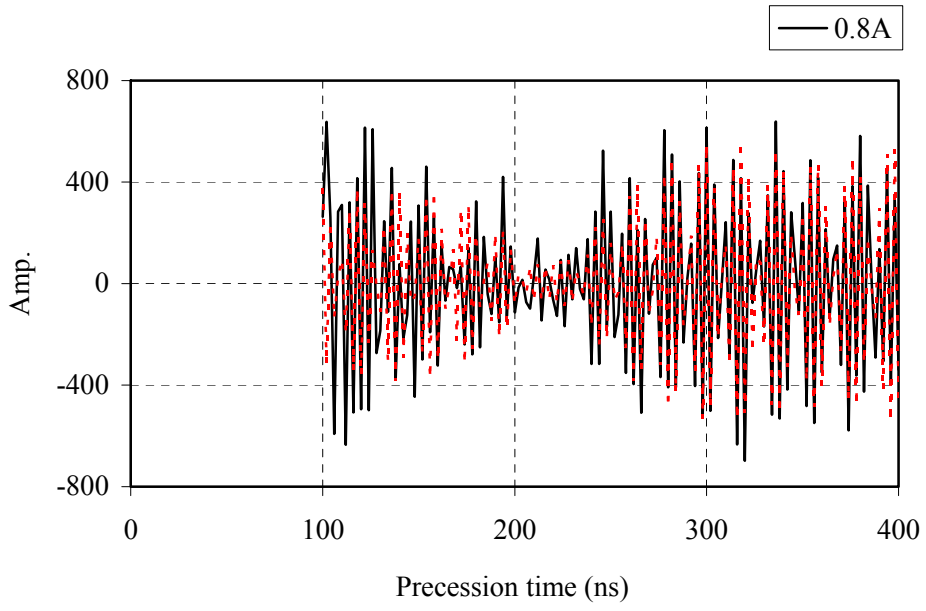

Figure 3.28 ESEEM data at a current of 0.8A applied to the gradient coil. Solid line is for the experimental data and dashed line is for the computer fitting using 3 frequency components. The two major frequency components are 223.921MHz and 221.313MHz. First node occurs at about 205ns.

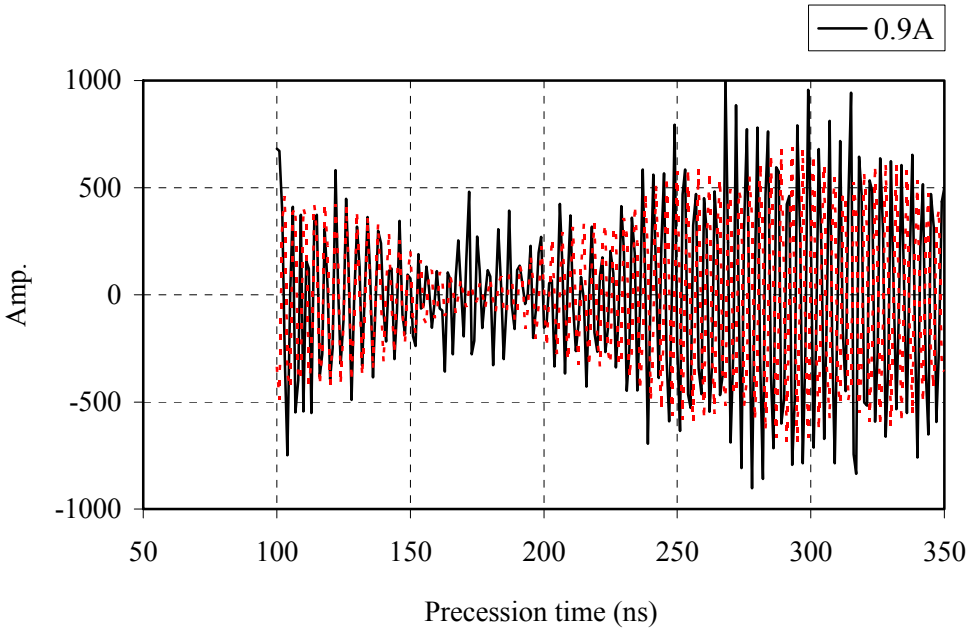

Figure 3.29 ESEEM data at a current of 0.9A applied to the gradient coil. Solid line is for the experimental data and dashed line is for the computer fitting using 3 frequency components. The two major frequency components are 257.8MHz and 260.6MHz. First node occurs at about 179ns.

Any low frequency modulation in the ESEEM signal was filtered out by using a high-pass filter with a cut-off frequency of 10MHz.

Although the third component has relatively small amplitude, it was included in the computer fitting model to fit the smaller amplitude modulation. However, its frequency could not be accurately determined in the fitting because it did not converge well due to the small amplitude modulation, and noise present in the signal.

By directly taking the FFT of the ESEEM signals with current of 0.7A, 0.8A and 0.9A the frequency spectrums were obtained as shown in figure 3.30. As the current increased, the frequency difference between the neighboring frequency components increased. Therefore the third component is now resolved clearly.

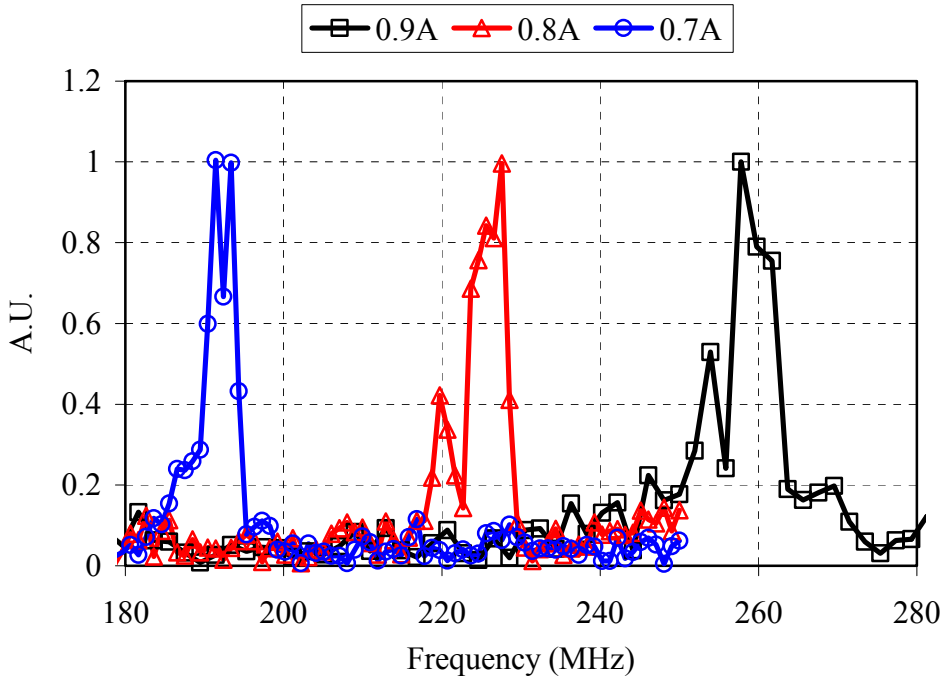

Figure 3.30 Frequency spectrum of the ESEEM signals for the current of 0.7A, 0.8A and 0.9A. The highest frequency component in each spectrum is named NV1, middle one NV2, and the lowest one NV3, in the NV site #5.

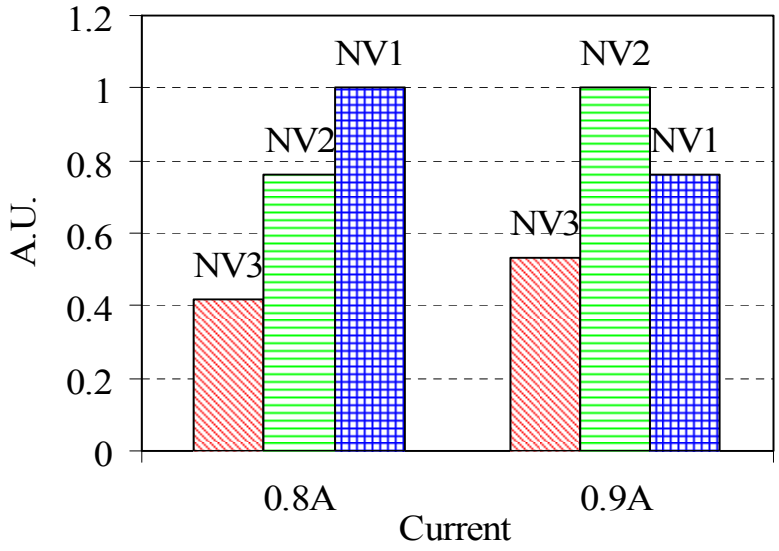

Figure 3.31 Relative amplitude of the three frequency components from the FFT of the ESEEM signal for 0.8A and 0.9A.

As seen in figure 3.31, comparison of the relative amplitude of the weak third frequency component (NV3) for the currents of 0.8A and 0.9A shows that it increased as the amplitude of the neighboring frequency component (NV2) increased.

A possible explanation is drift in the laser focus between data runs corresponding to the two current values. In this case the laser could be focused on the NV defect closest to the gradient coil at the 0.8A current, which is supposed to have the highest frequency (NV1), so that the NV3 will be out of focus, causing the fluorescence signal to become small. But if the laser is focused on the NV2 for the 0.9A current data, the NV3 is now closer to the focal volume of the laser spot resulting in higher fluorescence signal, and so the fluorescence signal becomes larger.

When a higher current was applied, frequency chirping was observed in the experimental data, and this is pronounced for the longer precession time, when larger gradient currents were applied. Due to this frequency chirping the spin precession frequency for shorter precession times is different than for longer precession time. Therefore computer fitting with three constant frequency components becomes invalid. Instead of being constant frequencies, the frequencies are a function of precession time.

In order to extract the chirp rate, the two major frequency components were given a variable chirp rate in the simulation that was used to fit the experimental data as seen in the equation (3.1):

$$\begin{aligned} y(t) = y_o &+ A_1 Cos\left(2\pi\left(f_1 + k\cdot(t-t_o)\right)\cdot(t-t_o)\right)e^{-((t-t_o)/T_2)} \\ &+ A_2 Cos\left(2\pi\left(f_2 + k\cdot(t-t_o)\right)\cdot(t-t_o)\right)e^{-((t-t_o)/T_2)} \end{aligned} \tag{3.1}$$

where k is the frequency chirp rate, T_2 is the spin dephasing time, and t_o compensates any timing errors in the experimental data.

Since only two frequency components were used in the equation there are some errors in the amplitude. But as far as the frequency is concerned the curve fitting with a chirped frequency was well matched over the whole time domain signal with the experimental data, as seen in figure 3.32.

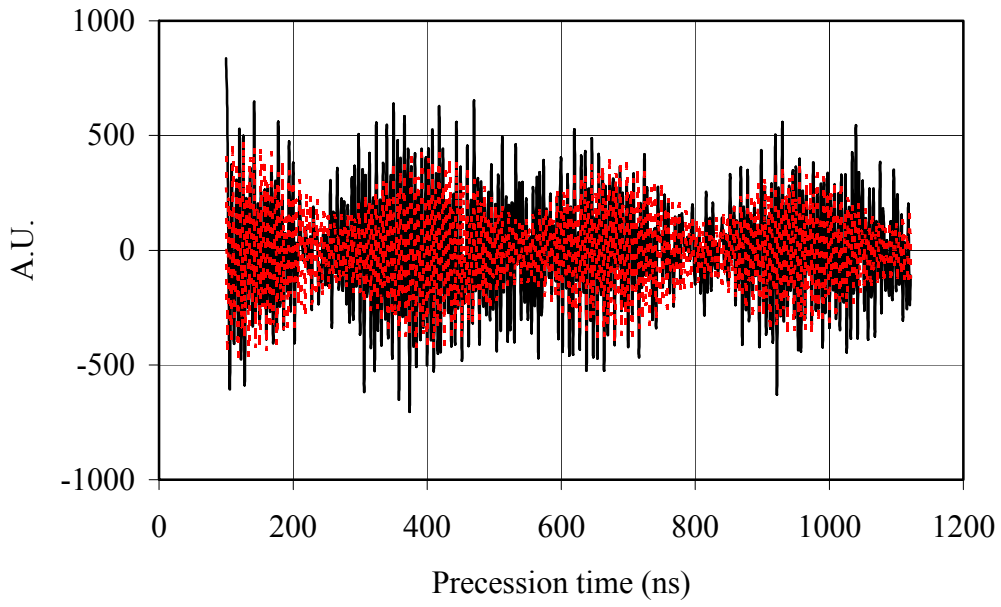

Figure 3.32 Curve fitting of ESEEM data for the current of 0.7A using the equation (3.1). Solid lines are for experimental data, and dashed lines for the fitting.

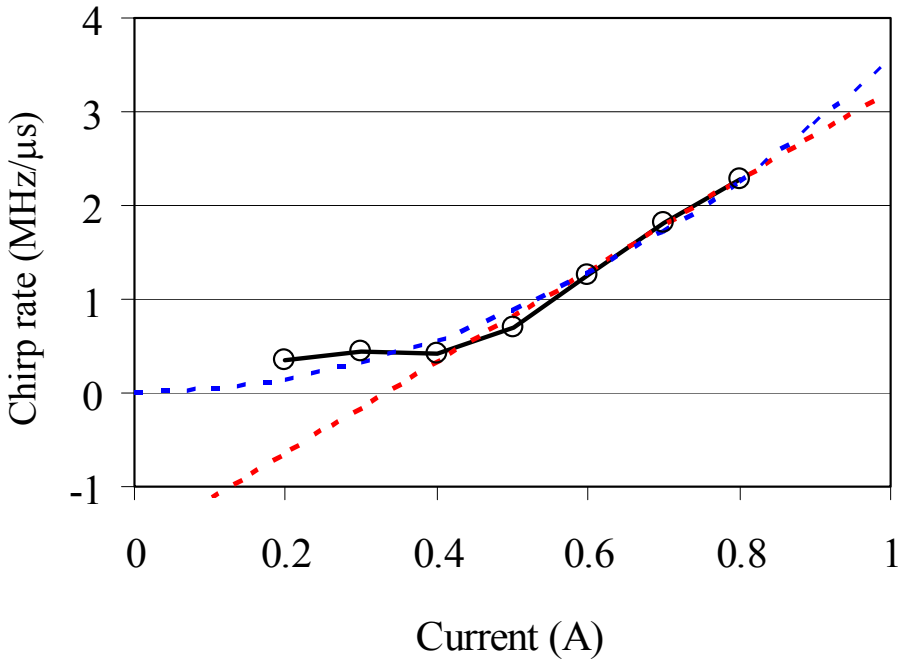

Figure 3.33 Frequency chirp rate (MHz/μs) as a function of the applied current to the gradient coil. Solid line with circles is for the chirp rate, and dotted lines are for the linear fit and quadratic fit.

The chirp rate obtained from the curve fitting is plotted as a function of the applied current along the gradient coil in figure 3.33. At low current, e.g. 0.4A, the chirp frequency was about 0.4MHz for the longest precession time, i.e. ~1μs, but it was more than 2MHz at higher current of 0.8A.

It is unclear if the chirp rate depends quadratically or linearly on the current. If the dependence is quadratic, then it could be originated from the heat produced by the RF pulse. The reason is that the heat pulse generated by a high current pulse may produce ultrasonic waves, and this may move the wire location relative to the NV molecules. The chirp rate would then show a quadratic dependence upon the current, since the heat is related linearly with the power. However, if the dependence is linear

then, the magnetic force induced by the current pulse may move the wire closer to any ferromagnetic material of the stage, and the distance between the gradient wire and NV molecules will decrease. In this case the chirp rate will depend linearly upon the current, due to the relatively large distance between the wire and the stage. However, with the current experimental setup the exact mechanism of the frequency chirping could not be determined.

3. Results and Discussion

In this section results for the ESEEM experiments are discussed together with the results from the CW ESR experiments, allowing the distance between neighboring NV defects to be estimated.

In the ESEEM data two major frequency components were easily identified by the beating of two frequency components, which was calculated by:

$$f_{beat} = \frac{1}{2 \cdot t_{node}} \tag{3.2}$$

where t_{node} is the time that the first node occurs in the ESEEM signal.

The third component was not easily identified in the time domain signal because of its relatively small amplitude and noise such as statistical noise, sampling error, etc. Instead of using the time domain signal directly, the FFT frequency spectrum of the ESEEM signal was used to determine the frequency of the third component. In the frequency spectrum two major frequency components for the high current cases, such as 0.7A, 0.8A or 0.9A are always pronounced. Assuming that two major components have about the same FWHM their average can be determined. Since the peak of the third

component was well resolved in the FFT spectrum, its frequency was easily determined allowing the frequency difference between the second and the third components to be roughly estimated. For the lower current cases the peak of the frequency components are not clearly resolved. Therefore the distance between the neighboring components are roughly estimated by fitting with lorentzians, assuming that they have about the same FWHM.

The frequency difference between neighboring NV defects obtained as described above are plotted as a function of the current applied along the gradient wire in figure 3.34.

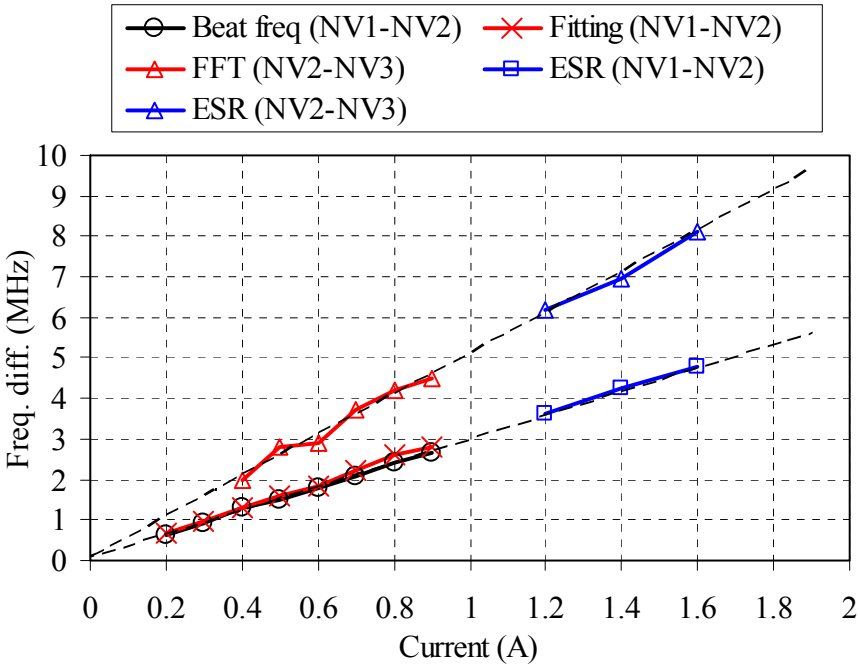

Figure 3.34 Frequency difference between neighboring NV defects, i.e. between NV1-NV2, and NV2-NV3, as a function of the current. Blue lines with triangles or squares are from the CW ESR, red lines with triangles are from the FFT of ESEEM signal, red lines with X marks are from curve fitting of two major components, and black line with circles is from the first node of the ESEEM signal.

In this data, the curve labeled 'Beat freq (NV1-NV2)' indicates the frequency difference between NV1 and NV2, which was calculated from equation (3.2), assuming the two NVs are slightly different distances away from the wire, where this distance is chosen to give the best fit to the experimental points, labeled 'Fitting (NV1-NV2).' These points indicate the observed frequency difference between NV1-NV2, and they were obtained from the curve fitting of the ESEEM signal. 'FFT (NV2-NV3)' indicates the frequency difference between NV2-NV3, estimated from the FFT of the ESEEM signal. 'ESR (NV1-NV2)' and 'ESR (NV2-NV3)' indicate frequency differences between neighboring components, i.e. NV1-NV2 or NV2-NV3, that were obtained from the CW ESR spectra discussed earlier.

In both experiments, i.e. CW ESR and ESEEM, magnetically in-equivalent NV defects were spectrally separated out by the uniform magnetic field applied along the z direction. The magnetically equivalent NV defects were then investigated using the magnetic field gradient induced by a current flowing through the gradient wire. If the frequency differences obtained from the ESEEM experiments originated from the same magnetically equivalent NV defects, they should agree with the results from the ESR experiments. Indeed, the frequency difference between neighboring components from the ESEEM experiments agrees quite well with the results from the ESR spectrum as seen in figure 3.34. Therefore, it is concluded that there are three magnetically equivalent NV defects and one magnetically in-equivalent NV defect present in the NV site #5.

In summary, in our experiments the DC current flowing through the thin copper wire, which was fabricated on a thin quartz cover-slip substrate (~150μm thick), induces a spatially non-uniform magnetic field around the wire. Therefore a spatially non-uniform magnetic field is applied to the NV defects. Under the spatially non-uniform magnetic field the defects experience different magnetic field strengths, since their relative locations from the center of the wire is not the same.

The estimated distance from the wire center to the NV site #5 is about 9.95μm as seen in figure 3.5. At this relatively long distance the induced magnetic field by the current may be considered axially symmetric around the wire, and so we assume that the magnetic field is induced by the current flowing along the infinitesimally thin wire, which is located at the center of the fabricated copper wire.

With the thin wire approximation, the induced non-uniform magnetic field around the copper wire can be described by the Biot-Savart law:[80]

$$\mathbf{B}_{\phi}(r) = a_{\phi}\frac{\mu_o\mu_r I}{2\pi r}(Tesla) \qquad (3.3)$$

As we can see from the equation (3.3), the magnetic field intensity quickly decreases as the distance increases, and its gradient decreases quadratically as the distance increases.

Since the induced magnetic field by the current through the gradient wire is at about 51.3 degrees from the NV quantization axis, equation (3.3) was modified as follows:

$$\left|\mathbf{B}_{\phi}(r)\right| = Cos(\theta)\frac{0.2\cdot I(A)}{r(\mu m)}(Tesla) = 1250.5\frac{I(A)}{r(\mu m)}(Gauss). \qquad (3.4)$$

At the location of the NV site #5, the center frequency of the ESEEM signal is almost linear with the current applied along the gradient coil as seen in figure 3.35. Therefore the quadratic dependence of the spin transition frequency of the NV site #5 at these weak magnetic fields is negligible. Consequently only a linear term is used to estimate the distance between NV defects,

$$\Delta E = \left(\Delta E_{0\leftrightarrow+1}(r_1) - \Delta E_{0\leftrightarrow+1}(r_2)\right) = \left(\left|B_\phi(r_1)\right| - \left|B_\phi(r_2)\right|\right)\cdot(2.8 MHz/Gauss) \quad (3.5)$$

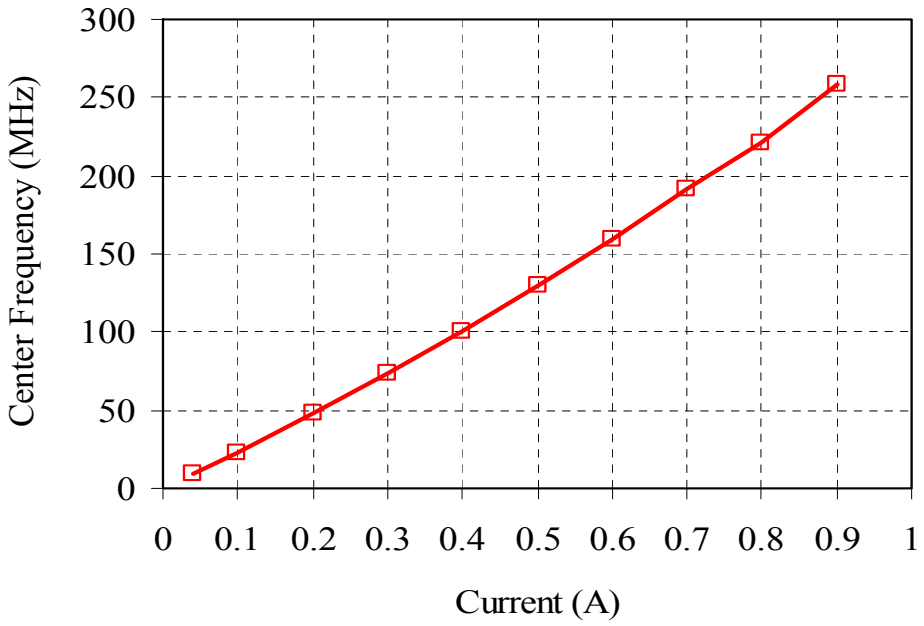

Figure 3.35 Center frequency of the ESEEM signal vs. the current applied along the gradient coil.

Using equations (3.4) and (3.5),

$$\Delta E = \Delta f = 1250.5\cdot(2.8)\cdot\left(\frac{1}{r_1} - \frac{1}{r_2}\right)\cdot I \ \ (MHz). \quad (3.6)$$

By fitting the experimental data shown in figure 3.34 with the above equation, NV locations from the wire center are roughly determined to be: $r_{NV1} = 9.862\mu m$, $r_{NV2} = 9.946\mu m$, and $r_{NV3} = 10.092\mu m$. So the distance between NV1 and NV2 is about 84nm, and the distance between NV2 and NV3 is about 146nm. At this relative distance of each NV defect, NV3 can be easily out of focus if the laser is focused on the NV1, which would explain the small fluorescence signal from the NV3 defect.

In summary of this section, ESEEM experiments with a magnetic field gradient, which was induced by the current through the thin copper wire, were carried out in order to resolve magnetically equivalent NV defects in the excitation laser focal volume. The results show good agreement with the ESR experimental results.

The heat dissipation problem of the thin wire could be solved by reducing the resistance of the thin wire, or improving the heat dissipation capability using high thermal conductive substrates, such as a low fluorescence Sapphire substrate or fabricating the device directly on a diamond substrate. Larger current could then be applied along the wire, which will produce a higher magnetic field gradient around the wire, so that a higher resolution can be obtained.

C. Ultra Fast Rabi Nutation Experiments for Fast Spin Manipulation for Quantum Computing Applications

In this section ultra fast Rabi nutation experiments are presented in an effort to demonstrate that ultra fast spin manipulations may be feasible due to the high microwave magnetic field induced by the micro-meter sized co-planar strip-lines. Fast spin

manipulation may be required to operate as many quantum gates as possible for quantum information processing within a spin coherence time in solid state quantum computing.

A high microwave magnetic field gradient from micro-meter sized co-planar strip-lines can also induce spatially non-uniform Rabi nutation frequencies, which may be used to resolve two spins located within the diffraction limited confocal microscope spot. In this case distance will be coded in the beating frequency of the different Rabi nutation frequencies.

1. Ultra Fast Rabi nutation Experiments Using Co-planar Microstriplines

As shown in the simulation results of the co-planar microstrip lines in figure 2.32, the current density in the narrow wires can be increased by reducing the width of the wires, and thereby enhancing the effective microwave magnetic field intensity on the NV defects close to the wire. In consequence ultra fast Rabi nutations of the electron spins can be achieved.

Fabricated microwave strip-lines were used to carry out Rabi nutation experiments in a weak uniform DC magnetic field, and the experimental data is shown in figure 3.36. In this experiment a microwave power of -13dBm at 2.87GHz, which was measured at the output port of the source, was modulated to produce pulses with a duration varying from 2ns to 1024ns. From this data a Rabi nutation period of 220ns was obtained with microwave power of -13dBm.

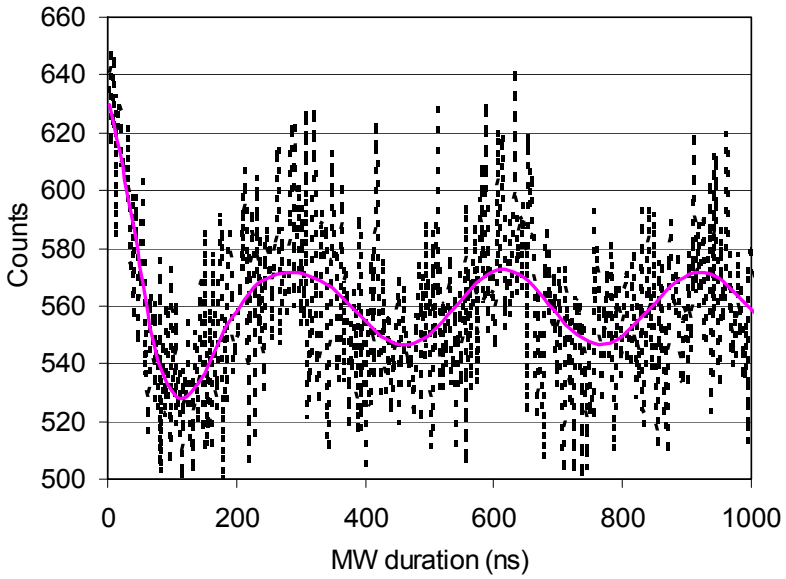

Figure 3.36 Experimental data of Rabi nutations of electron spin states with a fitted curve is shown. The fitted curve is achieved by equation (2.39) with parameters of r_o =559.3, A_1=15.64, p_1=306.6ns, A_2=55.83, p_2=223.8nsT_1=0.00859.

If we compare this result with the previous results shown in figure 2.25, the microwave power was 100 times smaller than for the case of 7dBm, yet the Rabi nutation period was decreased by only a factor of about 2. This indicates that the microwave field strength has been enhanced by a factor of about 25 by the fabricated microwave strip-lines.

Rabi nutation experiments at various microwave powers were carried out on NV defect site #5 and the results are shown in figure 3.35.

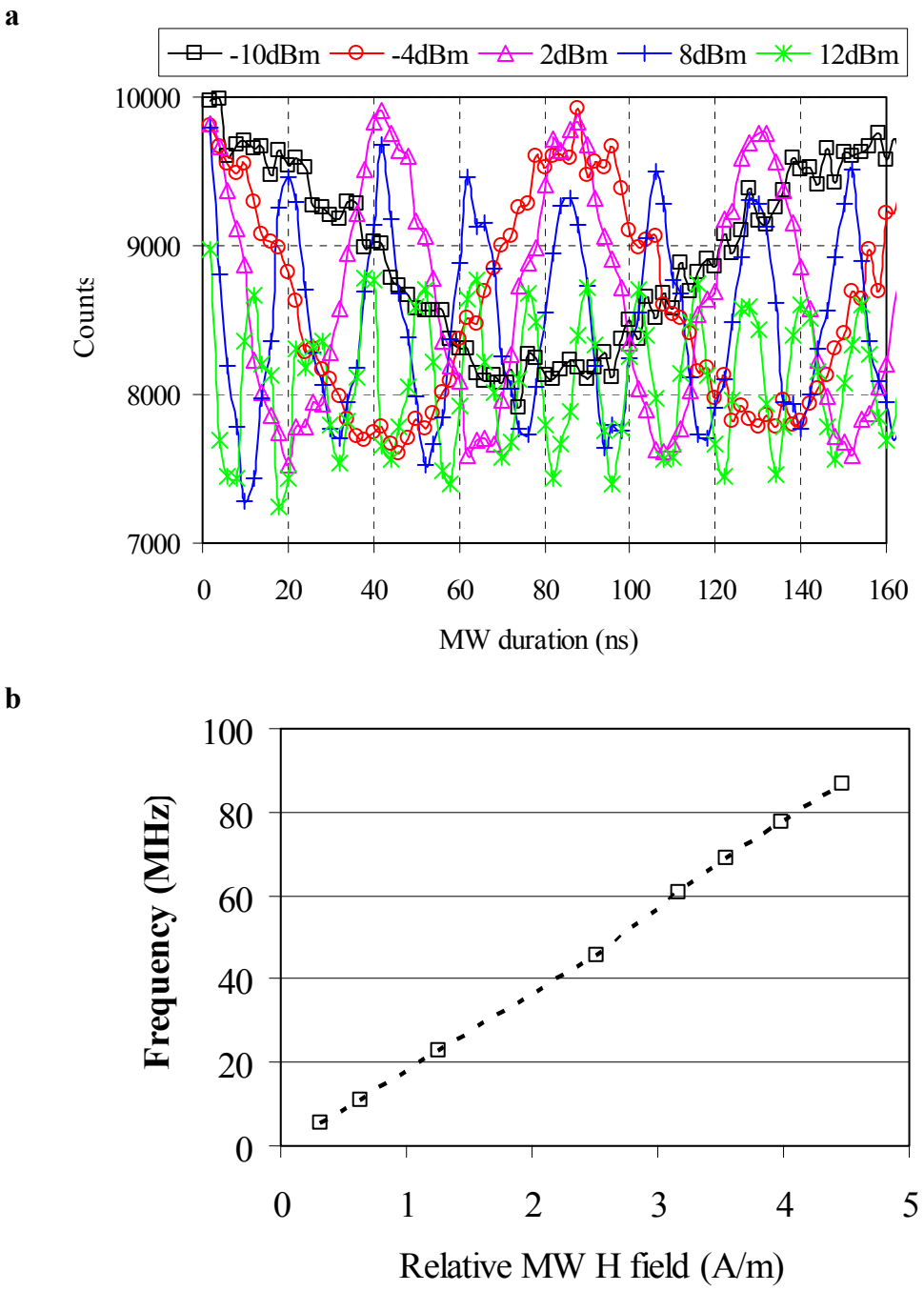

Figure 3.37 Rabi nutations of NV defect site #5 at various microwave power applied along the micro strip-lines. **a**, Relative microwave power, measured at the output of the microwave source, is indicated in plot. **b**, Rabi frequency in MHz vs. relative microwave magnetic field strength is plotted.

As the microwave power increases by 6dB the Rabi nutation period decreases by a factor of 2, therefore the Rabi nutation frequency depends linearly on the microwave current or magnetic field strength.

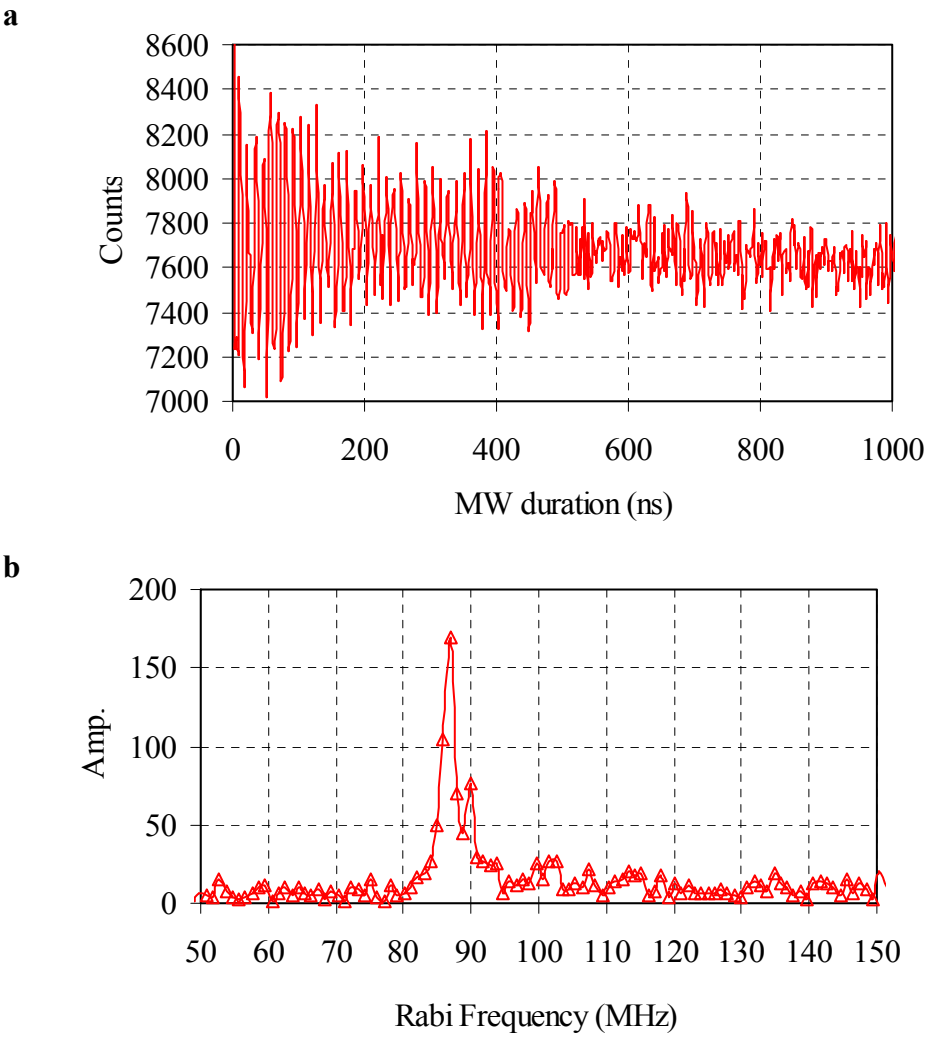

Figure 3.38 **a**, Rabi nutations of NV defect site #5 at a relative microwave power of 13dBm. **b**, Its frequency spectrum after taking FFT.

When a higher microwave power was applied the Rabi nutation signal showed a strong decaying for microwave pulse duration longer than 600ns, as shown in figure 3.38.

The decay observed in the Rabi nutations was attributed to drift in the microwave power. If the microwave power drifts then the Rabi frequency slightly changes, and so an average over many traces would give a decaying amplitude. The frequency spectrum in figure 3.38 (b) shows two frequency components clearly. They could be due to multiple NVs in the spatially non-uniform microwave magnetic field strength, but due to the decaying oscillations it is un-clear at this point. If a microwave power stabilization circuit is integrated into the system, this question can be answered, but it remains as a future work at this point.

In order to demonstrate the feasibility of ultra-fast spin manipulations by using the fabricated devices, another experiment was carried out by collaborators with nano-diamond crystals, spin-coated on the fabricated device.

Nano diamond crystals, in which NV defects were created, were spin-coated on the low fluorescence quartz cover slip with a fabricated device on top, and the fluorescence image is obtained as shown in figure 3.39. Red or bright regions represent NV defects, which are embedded in the nano diamond crystals.

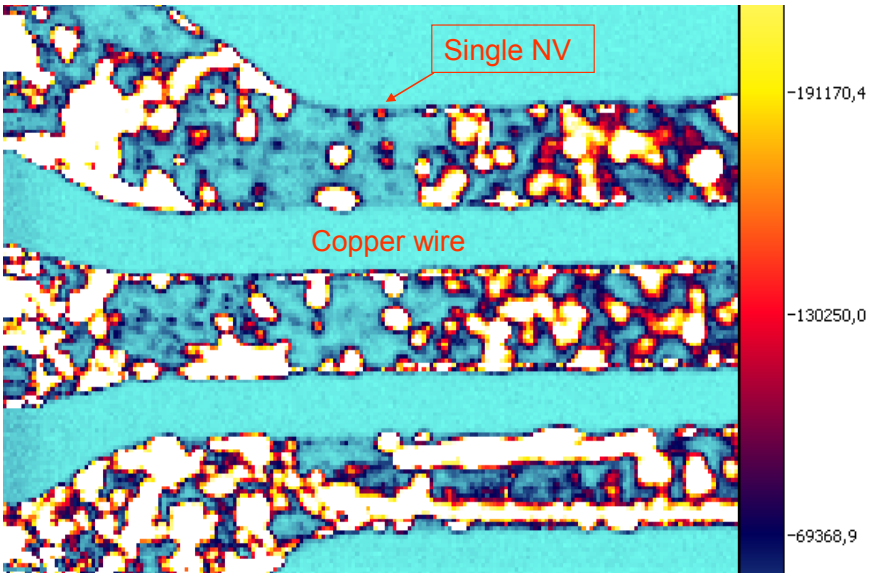

Figure 3.39 Fluorescence image of the co-planar microwave striplines with nano diamond crystals, and single NV defects close to the striplines were chosen for subsequent experiments.

CW ESR experiments were carried out in a weak external magnetic field, and ESR transition frequencies of 2.608GHz and 3.171GHz were identified as shown in figure 3.40. MW power of approximately 1mW was applied.

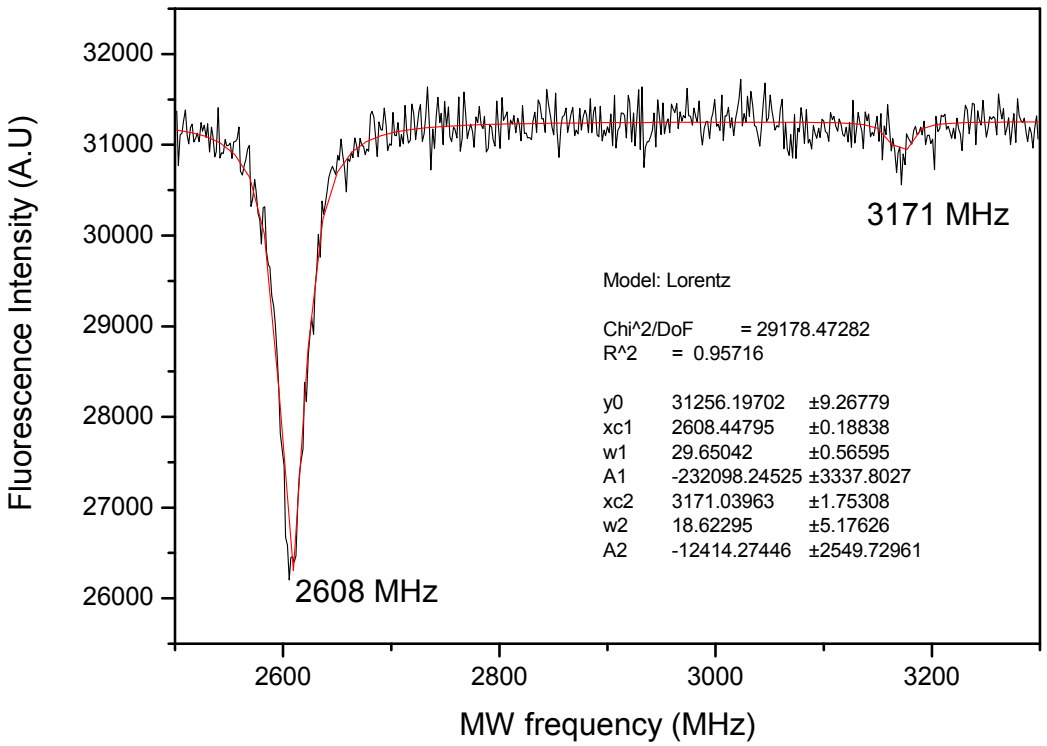

Figure 3.40 CW ESR experiments on a single NV defect in a nano crystalline diamond. MW power of approximately 1mW was applied with a small external magnetic field.

Rabi nutation experiments were carried out at the lower ESR transition frequency, i.e. 2.608GHz with the maximum available power of the TWT amplifier, i.e. 10Watts, in pulse mode. The MW pulse duration was varied form 8.5ns to 16.5ns in steps of 0.33ns, and a Rabi nutation period of 1.33ns was observed, as shown in figure 3.41. The corresponding oscillation frequency is 732MHz. Any noticeable heating at this power and pulse duty cycle was not observed.

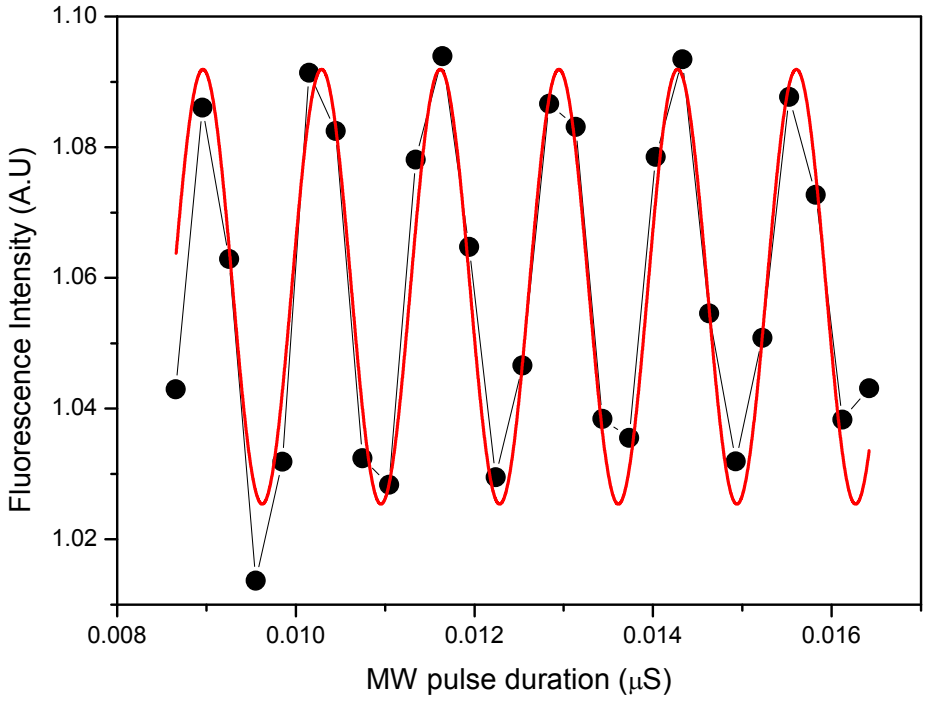

Figure 3.41 Rabi nutation period of 1.33ns was observed, which corresponds to the oscillation frequency of 732MHz.

2. Results and Discussion

As shown in the experimental data in figures 3.36, fabricated co-planar microstrip line enhances microwave magnetic field intensity by a factor of 25 higher than the 50μm wire which was shown in figure 2.25. Using the fabricated devices, fast Rabi nutations of electron spins were obtained. For the case of 13dBm of RF power applied to a region known to have multiple NV defects, i.e. NV site #5 in the previous CW ESR experiments, the frequency spectrum of the Rabi nutation signal showed two frequency components, but it is un-clear if this is originated from the spatially non-uniform microwave magnetic field or not.

Ultra fast Rabi nutations of the electron spins of a single NV defect in a nano diamond crystal was demonstrated and Rabi nutation frequency of 732MHz was achieved. This may allow us to manipulate spins fast enough to perform many quantum algorithms in a spin dephasing time.

In summary, ultra fast Rabi nutation was demonstrated by using the fabricated co-planar microwave striplines. Therefore, ultra fast spin manipulation can also be achieved by using the fabricated microwave striplines. These will enhance the ability to manipulate spins on single molecules. These devices can find many applications in single electron spin imaging, or quantum computing applications, etc.

CHAPTER IV

SUMMARY AND CONCLUSION

In summary of this research, a home-made laser scanning confocal fluorescence microscopy was built on an optics table. The confocal configuration was achieved by using a 50μm pinhole together with a pair of lenses. Using this experimental setup together with avalanche single photon detectors, the fluorescence image of molecules can be obtained with the resolution of a diffraction limited microscope spot, e.g. 300~400nm with a Nd:YAG excitation laser.

Background noise was efficiently rejected by the confocal microscope configuration. Therefore using single photon counting modules, photon antibunching experiments on quantum emitters such as nitrogen-vacancy defects in diamond can efficiently estimate the number of molecules in the focal volume of the excitation laser, if there are not too many molecules present.

Microwave equipment was also integrated into the microscope setup, so that optically detected electron spin resonance experiments, such as CW ESR experiments, electron spin Rabi nutation experiments, electron spin echo experiments, and electron spin echo envelope modulation experiments, can be performed.

In order to produce strong magnetic field gradients, such as a DC magnetic field gradient or a microwave magnetic field gradient, micrometer sized devices are designed and fabricated by optical lithography together with copper electroplating on a thin quartz cover-slip substrate with a thickness of 150-200μm. The fabricated gradient coil was

able to produce a high enough magnetic field gradient around the wire to achieve subwavelength imaging. Using the fabricated devices together with the experimental setups proof-of-principle experiments for single spin imaging were demonstrated by CW ESR experiments and ESEEM experiments. The experimental setup together with these fabricated devices enabled us to individually resolve multiple NV defects present in the focal volume of the diffraction limited microscope spot and to measure the distance between the molecules with sub-wavelength resolution, e.g. ~84nm.

The ESR experimental setup together with the fabricated devices can allow us to study local environments of molecules, and their dynamics at the single molecule level, and to rapidly manipulate the spin state of a single molecule, such as NV defects in diamond. Therefore, these techniques can overcome the loss of information caused by ensemble averaging, and find many applications such as molecular imaging and spin manipulation with sub-wavelength spatial selectivity.

Ultra fast Rabi nutation experiments are also demonstrated by using micrometer sized co-planar micro-striplines. Using a very high microwave magnetic field gradient, spatially non-uniform Rabi nutations can be induced, which may be used to image individual spins located in the focal volume of the microscope spot.

This may be advantageous over to the spin imaging techniques using CW ESR or ESEEM experiments. The reason is that the resolution of the CW ESR spectrum is limited by the broad line width and the resolution of the ESEEM signal is limited by the spin dephasing time, i.e. T_2, but the resolution of the Rabi nutations experiments is limited by the spin-lattice relaxation time, i.e. T_1. Typically, T_2 of the electron spin of

NV defects in diamond is on the order of 10s of microseconds but T_1 is on the order of milliseconds. Therefore, a much narrower line width can be obtainable.

Owing to the microwave power fluctuations in the current setup, the Rabi nutations signal for the case of high microwave power decayed after a few hundred nanoseconds. However, if a feedback circuit is developed to stabilize the microwave power, this problem can be overcome. This remains as a future work.

Fabricated microwave devices produce very high microwave magnetic fields. Using nano diamond crystals spin-coated on the fabricated devices ultra fast Rabi nutations with an oscillation frequency of 732MHz were demonstrated. This is the fastest Rabi nutations ever reported to the author's knowledge. Using this device, fast quantum information processing may be realized with a low microwave power, and more quantum algorithms can be processed for a given time, e.g. T_2.

In conclusion, optically detected ESR techniques including CW ESR, ESEEM, and Rabi nutations are very promising technologies to study individual molecules and to manipulate their spin states. Developed micrometer sized devices including DC magnetic field gradient wires and co-planar microwave striplines can also find many applications.

REFERENCES

[1] Hahn E. L. Spin echoes. *Phys. Rev.* **80**, 580-594 (1950).

[2] Blume R. J. Electron spin relaxation times in sodium-ammonia solutions. *Phys. Rev.* **109**, 1867-1873 (1958).

[3] Rowan L. G., Hahn E. L., and Mims W. B. Electron-spin-echo envelope modulation. *Phys. Rev.* **137**, A61-A71 **(**1965).

[4] Breiland W. G., Harris C. B., and Pines A. Optically detected electron spin echoes and free precession in molecular excited states. *Phys. Rev. Lett*. **30**, 158-161 (1973).

[5] Feher G. Electron spin resonance experiments on donors in silicon. I. Electronic structure of donors by the electron nuclear double resonance technique. *Phys. Rev.* **114**, 1219-1243 (1959).

[6] Köhler J., Disselhorst J. A. J. M., Donckers M. C. J. M., Groenen E. J. J., Schmidt J., and Moerner W. E. Magnetic resonance of a single molecular spin. *Nature* **363**, 242-244 (1993).

[7] Drndić M., Johnson K. S., Thywissen J. H., Prentiss M., and Westervelt R. M. Micro-electromagnets for atom manipulation. *App. Phys. Lett.* **72**, 2906-2908 (1998)

[8] Neamen Donald A. *Semiconductor Physics and Devices* (Richard D. Irwin Inc., Boston, 1992).

[9] Trajkov E. *The Study of Defect and Trapping Levels in CVD Polysrystalline Diamond with Applications to Ultraviolet Dosimetry* (School of Physics, The University of Melbourne, Australia, May 2004).

[10] Dyer H. B., Raal F. A., du Preez L., and Loubser J. H. N. Optical absorption features associated with paramagnetic nitrogen in diamond. *Phil. Mag.* **11**, 763-774 (1965).

[11] Lax M. and Burstein E. Infrared lattice absorption in ionic and homopolar crystals. *Phys. Rev.* **97**, 39-52 (1955).

[12] Bibby D. M., Fesq H. W. and Sellschop J. P. F. Trace elements in diamonds of different types. *Nature* **276**, 379-381 (1978).

[13] Davies G. and Hamer M. F. Optical studies of the 1.945eV vibronic band in diamond. *Proc. R. Soc. London* **A. 348**, 285-298 (1976).

[14] Collins A. T., Thomaz M. F., Jorge M. I. B. Luminescence decay time of the 1.945eV centre in type Ib diamond. *J. Phys. C: Solid State Phys.* **16**, 2177-2181 (1983).

[15] Reddy N. R. S., Manson N. B., and Krausz E. R. Two-laser spectral hole burning in a colour centre in diamond. *J. Lumin.* **38**, 46-47 (1987).

[16] Oort E. van, Manson N. B., and Glasbeek M. Optically detected spin coherence of the diamond NV centre in its triplet ground state. *J. Phys. C* **21**, 4385-4391 (1988).

[17] Holliday K., Manson N. B., Glasbeek M., and Oort E. van Optical hole-bleaching by level anti-crossing and cross relaxation in the N-V centre in diamond. *J. Phys.: Condens. Matt.* **1**, 7093-7102 (1989).

[18] Manson N. B., He X. F., and Fisk P. T. H. Raman heterodyne detected electron-nuclear-double-resonance measurements of the nitrogen-vacancy center in diamond. *Opt. Lett.* **15**, 1094-1096 (1990).

[19] Redman D. A., Brown S., Sands R. H., and Rand S. C. Spin dynamics and electronic states of N-V centers in diamond by EPR and four-wave-mixing spectroscopy. *Phys. Rev. Lett.* **67**, 3420-3423 (1991).

[20] Loubser J. H. N. and Wyk J. A. Electron spin resonance in the study of diamond. *Rep. Prog. Phys.* **41**, 1201-1248 (1978).

[21] Harrison J., Sellars M. J., Manson N. B. Optical spin polarization of the N-V centre in diamond. *J. Lumin.* **107**, 245-248 (2004).

[22] Wrachtrup J. and Jelezko F. Quantum information processing in diamond. *J. Phys.: Condens. Matter* **18,** S807-S824 (2006).

[23] Uedono A., Mori K., Morishita N., Itoh H., Tahigawa S., Fujii S., and Shikata S. Annealing behaviours of defects in electron-irradiated diamond probed by positron annihilation. *J. Phys.: Condens. Matter* **11**, 4925-4934 (1999).

[24] Gaebel T., Domhan M., Wittmann C., Popa I., Jelezko F., Rabeau J., Greentree A., Prawer S., Trajkov E., Hemmer P. R., and Wrachtrup J. Photochromism in single nitrogen-vacancy defect in diamond. *Appl. Phys. B* **82**, 243-246 (2006).

[25] Smith W. V., Sorokin P. P., Gelles I. L., and Lasher G. J. Electron-spin resonance of nitrogen donors in diamond. *Phys. Rev.* **115**, 1546-1552 (1959).

[26] Cook R. J. and Whiffen D. H. Electron nuclear double resonance study of a nitrogen centre in diamond. *Proc. R. Soc. A* **295**, 99-106 (1966).

[27] Oort E. B., Stroomer P., and Glasbeek M. Low-field optically detected magnetic resonance of a coupled triplet-doublet defect pair in diamond. *Phys. Rev. B* **42**, 8605-8608 (1999).

[28] He X. F., Manson N. B., and Fisk P. T. H. Paramagnetic resonance of photoexcited N-V defects in diamond. II. Hyperfine interaction with the ^{14}N nucleus. *Phys. Rev. B* **47**, 8816-8822 (1993).

[29] Oort E. V. and Glasbeek M. Cross-relaxation dynamics of optically excited N-V centers in diamond. *Phys. Rev. B* **40**, 6509-6517 (1989).

[30] Gaebel T. et.al. Room-temperature coherent coupling of single spins in diamond. *Nature Physics* **2**, 408-413 (2006).

[31] Holliday K., He X. -F., Fisk P. T. H., and Manson N. B. Raman heterodyne detection of electron paramagnetic resonance. *Opt. Lett.* **15**, 983-985 (1990).

[32] He X. F., Manson N. B., and Fisk P. T. H. Paramagnetic resonance of photoexcited N-V defects in diamond. I. Level anticrossing in the ^{3}A ground state. *Phys. Rev. B* **47**, 8809-8815 (1993).

[33] Wei C. and Manson N. B. Observation of electromagnetically induced transparency within an electron spin resonance transition. *J. Opt. B: Quantum Semiclass. Opt.* **1**, 464-468 (1999).

[34] Wei C. and Manson N. B. Observation of the dynamic Stark effect on electromagnetically induced transparency. *Phys. Rev. A* **60**, 2540-2546 (1999).

[35] Hemmer P. R., Turukhin A. V., Shahriar M. S., and Musser J. A. Raman-excited spin coherences in nitrogen-vacancy color centers in diamond. *Optics Lett.* **26**, 361-363 (2001).

[36] Gruber A., Dräbenstedt A., Tietz C., Fleury L., Wrachtrup J., and Borczyskowski C. V. Scanning confocal optical microscopy and magnetic resonance on single defect centers. *Science* **276**, 2012-2014 (1997).

[37] Becker W. *Advanced Time-Correlated Single Photon Counting Techniques* (Springer, Germany, 2005).

[38] Kurtsiefer C., Mayer S., Zarda P. and Weinfurter H. Stable solid-state source of single photons. *Phys. Rev. Lett.* **85**, 290-293 (2000).

[39] Brouri R., Beveratos A., Poizat J.-P., Grangier P. Photon antibunching in the fluorescence of individual color center in diamond. *Opt. Lett*. **25**, 1294-1296 (2000).

[40] Beveratos A., Brouri R., Poizat J.-P., and Grangier P. Bunching and antibunching from single NV color centers in diamond. *Proceedings of the International Conference on Quantum Information, Measurement and Computing*, Capri, July (2000).

[41] Beveratos A., Kühn S., Brouri R., Gacoin T., Poizat J.-P., Grangier P. Room temperature stable single-photon source. *Eur. Phys. J. D* **18**, 191-196 (2002).

[42] Fu C.-C., Lee H.-Y., Chen K., Lim T.-S., Wu H.-Y., Lin P.-K., Wei P.-K., Tsao P.-H., Chang H.-C., and Fann W. Characterization and application of single fluorescent nanodiamonds as cellular biomarkers. *Proc. Natl. Acad. Sci. USA*. **104(3)**: 727–732 (2007).

[43] Meijer J., Burchard B., Domhan M., Wittmann C., Gaebel T., Popa I., Jelezko F., and Wrachtrup J. Generation of single color centers by focused nitrogen implantation. *Appl. Phys. Lett.* **87**, 261909 (2005).

[44] Rabeau J. R., Reichart P., Tamanyan G., Jamieson D. N., and Prawer S., Jelezko F., Gaebel T., Popa I., Domhan M., and Wrachtrup J. Implantation of labelled single nitrogen vacancy centers in diamond using ^{15}N. *Appl. Phys. Lett.* **88**, 023113 (2006).

[45] Gruber A., Drabenstedt D., Tietz C., Fleury L., Wrachtrup J., Borczyskowski C. V. Scanning confocal optical microscopy and magnetic resonance on single defect centers. *Science* **276**, 2012-2014 (1997).

[46] Oort E. van and Glasbeek M. Optically detected low field electron spin echo envelope modulations of fluorescent N-V centers in diamond. *Chem. Phys.* **143,** 131-140 (1990).

[47] Oort E. van, Manson N.B. and Glasbeek M. Optically detected spin coherence of the N-V diamond centre in its triplet ground state. *J. Phys. C* **21**, 4385-4391 (1988).

[48] Harley R.T., Henderson M. J., and Macfarlane R. M. Persistent spectral hole burning of colour centres in diamond. *J. Phys. C* **17**, L233-L236 (1984).

[49] Martin J., Wannemacher R., Teichert J., Bischoff L., Köhler B. Generation and detection of fluoresence color centers in diamond with submicron resolution. *Appl. Phys. Lett.* **75**, 3096-3098 (1999).

[50] Charnock F. T. and Kennedy T. A. Combined optical and microwave approach for performing quantum spin operations on nitrogen-vacancy center in diamond. *Phys. Rev. B* **64**, 041201 (2001).

[51] Jelezko F., Popa I., Gruger A., Tietz D., and Wrachtrup J. Single spin states in a defect center resolved by optical spectroscopy. Appl. Phys. Lett. **81**, 2160-2162 (2002).

[52] Jelezko F., Gaebel T., Popa I., GrugeA. r, and Wrachtrup J. Observation of coherent oscillations in a single electron spin. *Phys. Rev. Lett.* **92**, 076401 (2004).

[53] Popa I., Gaebel T., Domhan M., Wittmann C., Jelezko F., and Wrachtrup J. Energy levels and decoherence properties of single electron and nuclear spins in a defect center in diamond. *Phys. Rev. B* **70**, 201203 (2004).

[54] Jelezko F., Gaebel T., Popa I., Domhan M., Gruber A., and Wrachtrup J. Observation of coherent oscillation of a single nuclear spin and realization of a two-qubit conditional quantum gate. *Phys. Rev. Lett.* **93**, 130501 (2004).

[55] Martin J., Wannemacher R., Teichert J., Bischoff L. and Köhler B. Generation and detection of fluorescent color centers in diamond with submicron resolution. *Appl. Phys. Lett.* **75**, 3096-3098 (1999).

[56] Hettich C., Schmitt C., Zitzmann J., Kühn S., Gerhardt I., and Sandoghdar V. Nanometer resolution and coherent optical dipole coupling of two individual molecules. *Science* **298**, 385-389 (2002).

[57] Epstein R. J., Mendoza F. M., Kato Y. K., and Awschalom D. D. Anisotropic interactions of a single spin and dark-spin spectroscopy in diamond. *Nature Phys.* **1**, 94-98 (2005).

[58] Gaebel R., Domhan M., Popa I., Wittmann C., Neumann P., Jelezko F., Rabeau J., Stravrias N., Greentree A., Prawer S., Meijer J., Twamley J., Hemmer P. R., and Wrachtrup J. Room-temperature coherent coupling of single spins in diamond. *Nature Phys.* **2**, 408-413 (2006).

[59] Childress L., Dutt M. V. G., Taylor J. M., Zibrov A. S., Jelezko F., Wrachtrup J., Hemmer P. R., Lukin M. D. Coherent dynamics of coupled electron and nuclear spin qubits in diamond. *Science* **314**, 281-285 (2006).

[60] Jelezko F. and Wrachtrup J. Read-out of single spins by optical spectroscopy. *J. Phys.: Condens. Matter* **16**: R1089-S1104 (2004).

[61] Jelezko F. and Wrachtrup J. Quantum information processing in diamond. *J. Phys.: Condens. Matter* **18**: S807-S824 (2006).

[62] Jelezko F. and Wrachtrup J. Single defect centers in diamond: A review. *physica status solidi (a)* 203, 3207-3225 (2006).

[63] Corle T. R. and Kino G. S. *Confocal Scanning Optical Microscopy and Related Imaging Systems*. (Academic Press Limited, London, 1996).

[64] Meinhart C. D. and Wereley S. T. The theory of diffraction-limited resolution in microparticle image velocimetry. *Meas. Sci. Technol*. **14,** 1047-1053 (2003).

[65] Gökhan Ulu, Sergienko A. V., and Ünlü M. S. Influence of hot-carrier luminescence from avalanche photodiodes on time-correlated photon detection. *Opt. Lett.* **25**, 758-760 (2000).

[66] Davies G. *Properties and Growth of Diamond*. (IEE/INSPEC, 1994).

[67] Jelezko F. and Wrachtrup J. Read-out of single spins by optical spectroscopy. *Phys.: Condens. Matter* **16**, R1089-R1104 (2004).

[68] Brouri R., Beveratos A., Poizat J. P., Grangier P. Photon antibunching in the fluorescence of individual color centers in diamond. *Opt. Lett.* **25**, 1294-1296 (2000).

[69] Kurtsiefer C., Mayer S., Zarda P., and Weinfurter H. Stable solid-state source of single photons. *Phys. Rev. Lett.* **85**, 290 - 293 (2000).

[70] Beveratos A., Kühn S., Brouri R., Gacoin, T., Poizat J.-P., Grangier P. Room temperature stable single-photon source. *Eur. Phys. J. D* **18**, 191-196 (2002).

[71] Kitson S. C., Jonsson P., Rarity J. G., and Tapster P. R. Intensity fluctuation spectroscopy of small numbers of dye molecules in a microcavity. *Phys. Rev. A* **58**, 620-627 (1998).

[72] Arecchi F. T., Corti M., Degiorgio V., and Donati S. Measurements of the light intensity correlations in the subnanosecond region by photomultipliers. *J. Opt. Commun.* **3**, 284-288 (1971).

[73] Beveratos A., Brouri R., Poizat J.-P., and Grangier P. Bunching and antibunching from single NV color centers in diamond. *Proceedings of the International Conference on Quantum Information, Measurement and Computing*, Capri, July (2000).

[74] Cook R. J., Whiffen, D. H. Electron nuclear double resonance study of a nitrogen centre in diamond. *Proceedings of the Royal Society of London Series A, Mathematical and Physical Sciences* **295**, 99-106 (1966).

[75] He Xing-Fei, Manson, Neil B., Fisk Peter T. H. Paramagnetic resonance of photoexcited NV defects in diamond. II. Hyperfine interaction with the ^{14}N nucleus. *Phys. Rev. B Condensed Matter* **47,** 8816-8822 (1993).

[76] Popa, I., Gaebel, T., Domhan, M., Wittmann, C., Jelezko, F., Wrachtrup, J. Energy levels and decoherence properties of single electron and nuclear spins in a defect center in diamond. *Phys. Rev. B* **70**, 201203 (2004).

[77] Charnock Forrest T., Kennedy T. A. Combined optical and microwave approach for performing quantum spin operations on the nitrogen-vacancy center in diamond. *Phys. Rev. B* **64,** 041201 (2001).

[78] McGlynn S. P., Azumi T. Kinoshita M. *Molecular Spectroscopy of the Triplet State* (Prentice-Hall, Englewood Cliffs, NJ, 1970).

[79] Mandel L., Wolf E. *Optical Coherence and Quantum Optics*. (Cambridge University Press, 1995).

[80] Cheng David K. *Field and Wave Electromagnetics* (Addison-Wesley Pullishing Company, Reading, MA, 1992).

APPENDIX

A. ECT to TTL logic conversion circuit

As discussed in chapter II, the arbitrary waveform generator (AWG2041, Tektronix) is used to program pulse sequences for pulse mode experiments. Its digital outputs are emitter-coupled logic (ECL) signals (logic 'high' at -0.9Volt logic 'low' at -1.75 Volt) at 50 Ohm, but equipments such as ultra-fast microwave switches, RF drivers of the AOM, etc., accept transistor-transistor logic (TTL) signals at 50 Ohm or higher impedance. In an effort to convert the ECL signals of the AWG2041 to TTL signal outputs, logic conversion circuits were developed by a colleague, Changdong Kim, as seen in figures A-1 and A-2. The output signal shown in figure A-1 (a) is modeled as VG1 in figure A-2.

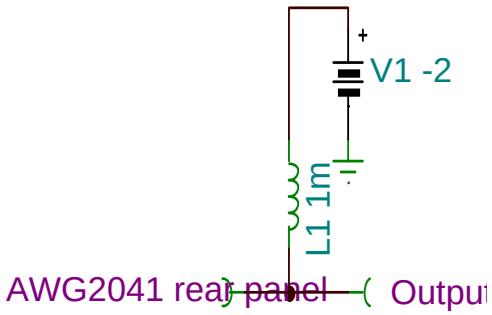

(a)

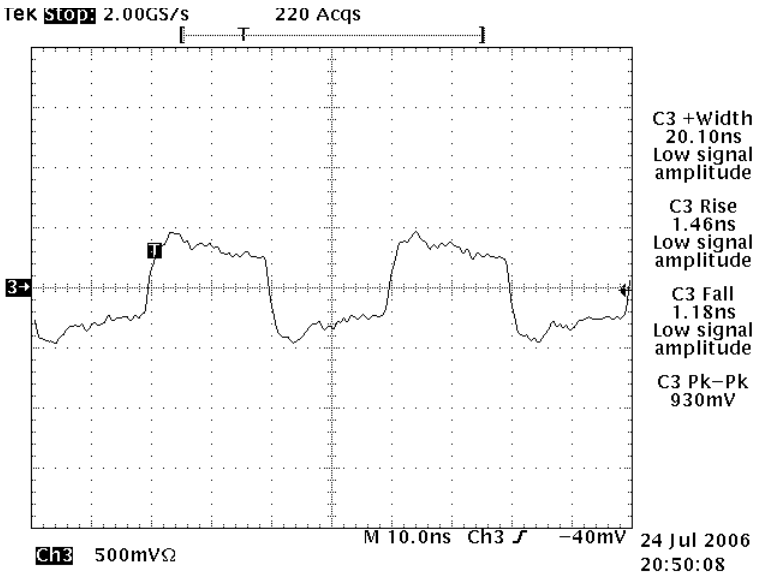

(b)

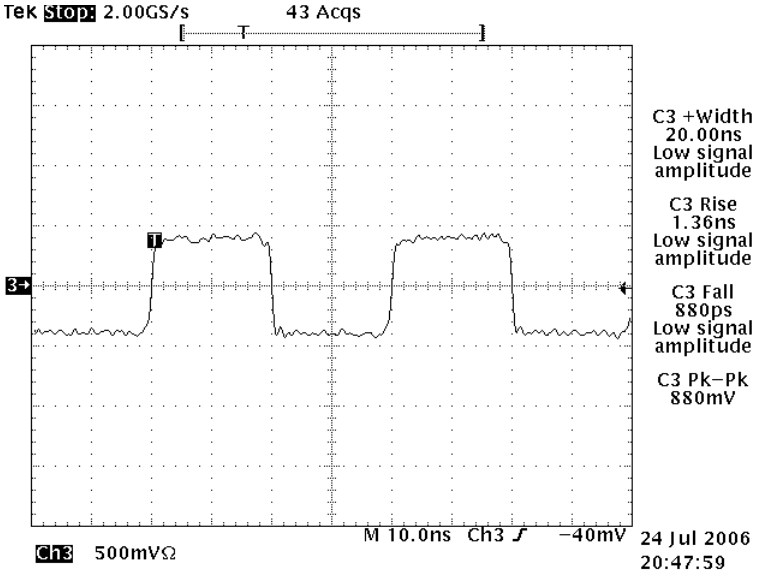

(c)

Figure A-1 ECL level digital output pulses of the AWG2041. Schematic diagram of the biasing circuit for input signal (a), 20ns pulse signal for the case without an inductor (b), and 20ns pulse signal for the case with the inductor of 1mH (c).

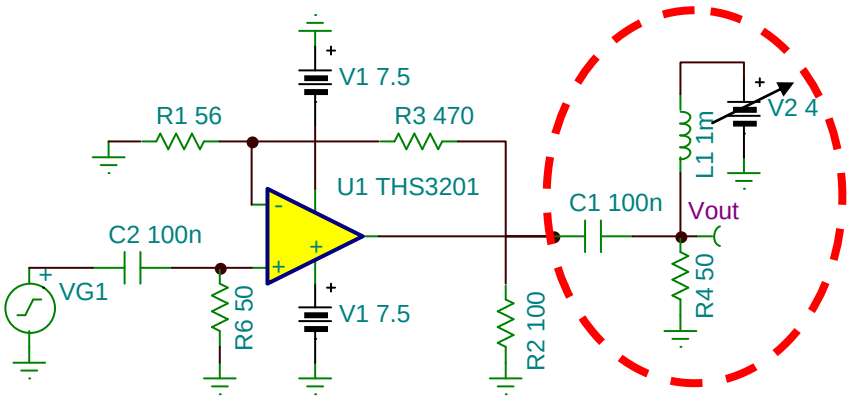

Figure A-2 Schematic diagram of logic conversion circuit. Bias circuit (in red circle) with an inductor of 1mH was used to give offset voltage.

For the digital outputs at ECL level, digital output transistors of the AWG2041 were biased with -2 Volts. After the ECL signal was amplified by the OP amplifier (TH3201, Texas Instruments Inc.), DC offset voltage was applied to raise the signal for TTL level (logic 'low' at 0 Volt, logic 'high' at 5 Volt). In the bias circuits for signal input and output, inductance of 1mH was used to reduce noise.

B. DC current pulse switching circuit

In order to achieve a large magnetic field gradient, large current should flow along the gradient coils. Due to the limited power dissipation capability of the fabricated gradient coils, large current can not be applied continuously. Therefore a fast current switching circuit was developed by a colleague, Dr. Roman Kolesov as shown in figure A-3.

When TTL pulse sequences from the logic conversion circuit output are fed to the input port of the current switching circuit (V2 in the diagram), DC current through the gradient coil (R8 in the diagram) is switched according to the input pulse sequences.

The gradient coil is modeled as R-L-C circuit as shown in the red dotted box. R-C snubber circuit, shown in the green dotted box, was inserted to reduce overshooting of the output current at the end of the pulse, which was induced by the unclamped stray inductance of the wire.

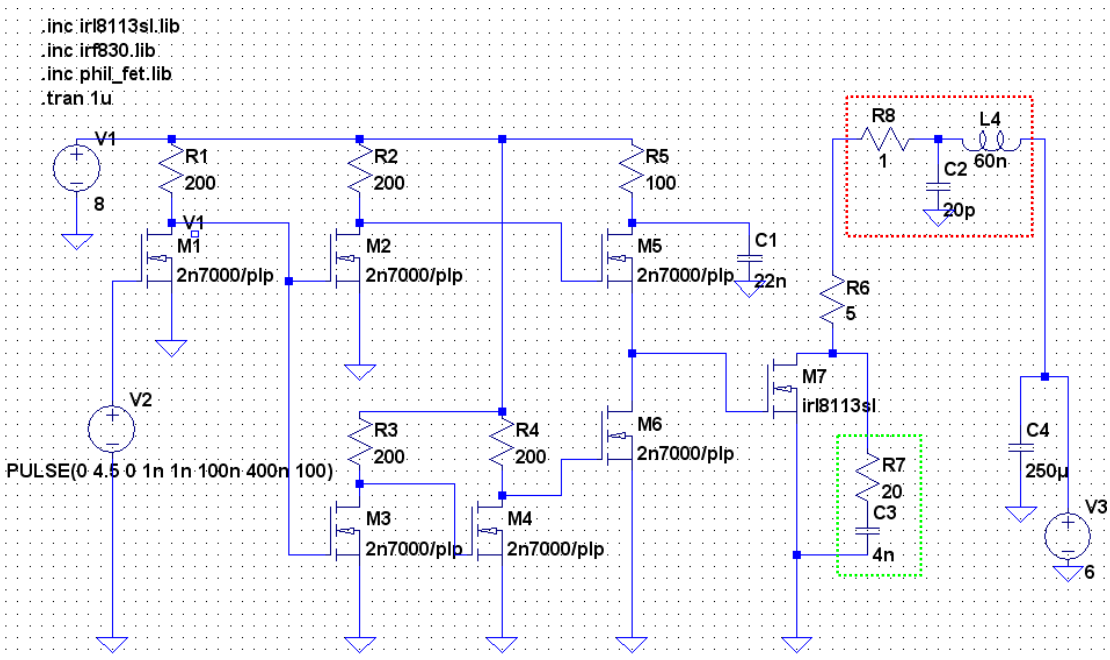

Figure A-3 Schematic diagram of the DC current switching circuit.

Using this home-built current switch, DC current pulses can be efficiently synchronized with other signals such as optical excitation, microwave signal, etc., and relative large current (~2A) with duration of a few hundred nano seconds to microseconds can be applied.

C. Ramp signal generator circuit for the frequency sweep input of microwave signal

Due to the slow electronic circuits of the microwave source used in the setup (HP8350B, Hewlett-Packard Inc.), internal frequency sweep mode is very slow (the fastest is 10ms) with delay time of about 10ms. In order to sweep faster without much delay time a ramp signal generator circuit (0~10Volts) was designed by a colleague, Dr. Roman Kolesov as shown in figure A-4.

When a TTL pulse with pre-determined duration (typically several milliseconds) was applied to the input port (V1), a ramp voltage signal with the same duration is generated at the output port (V_{out}). By adjusting capacitance (C2) and resistances (R6 and R7), a 0 to 10Volts linear ramp signal can be achieved. This signal output was used to sweep the frequency of the microwave signal externally. Since the TTL input signal is from the master timing signal, it will be synchronized to other signals.

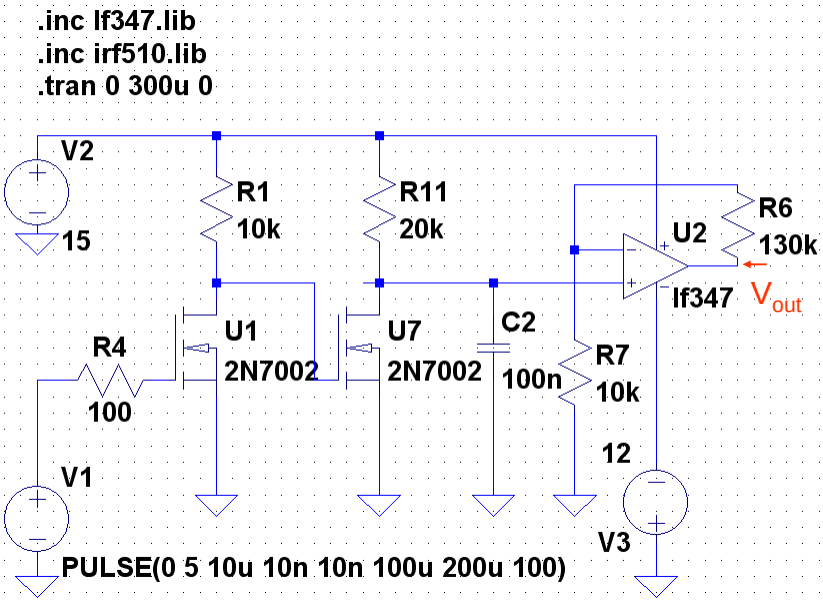

Figure A-3 0~10Volts ramp voltage generator ciruit.

D. PCB fabrication

In order to reduce reflection loss due to impedance mismatch, microwave striplines were fabricated on the microwave circuit board. Using a microwave simulator (IE3D, Zeland Inc.) 50 Ohm transmission lines were designed, and negative film with designed patterns was generated.

Flexible substrates (RT/duroid 5870, Rogers Corp.) were used. Dielectric constant of the substrate was 2.33, thickness was 0.508mm, and copper thickness was 17μm. After laminating the photoresist film on the substrate, it was masked with negative film, exposed by UV lamp, and developed with a developer followed by copper etching. Typical resolution of this process is about 200 micrometers. If we use typical optical lithography, a higher resolution should be achieved.

E. Photo images of the experimental setup

Photo images of the experimental setup are shown in this section with brief captions. Detailed information may be found in the main chapters.

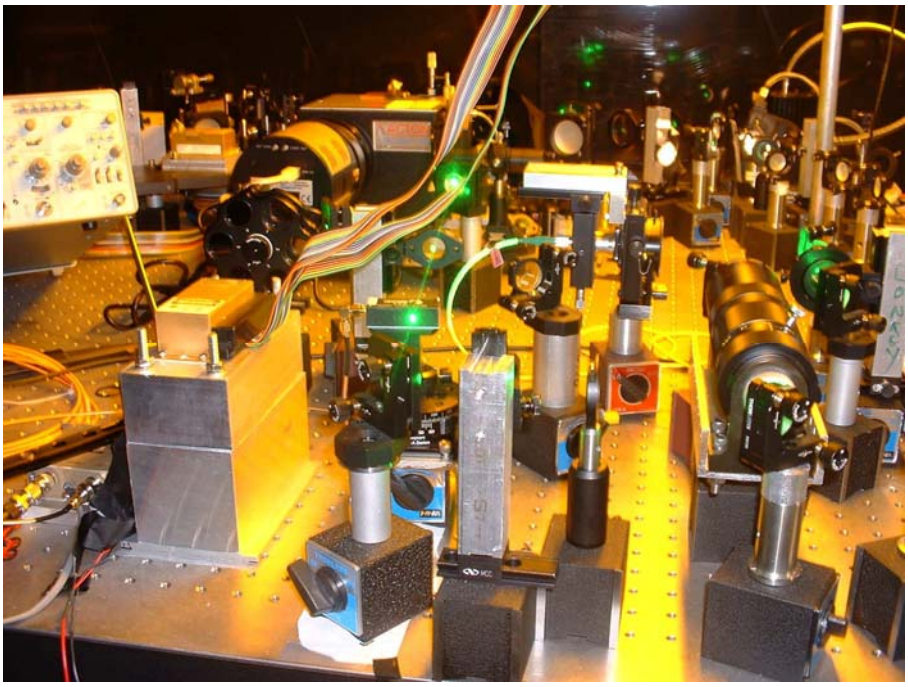

Figure A-4 Photo image of the Nd:YAG laser, AOM, telescope, input collimation.

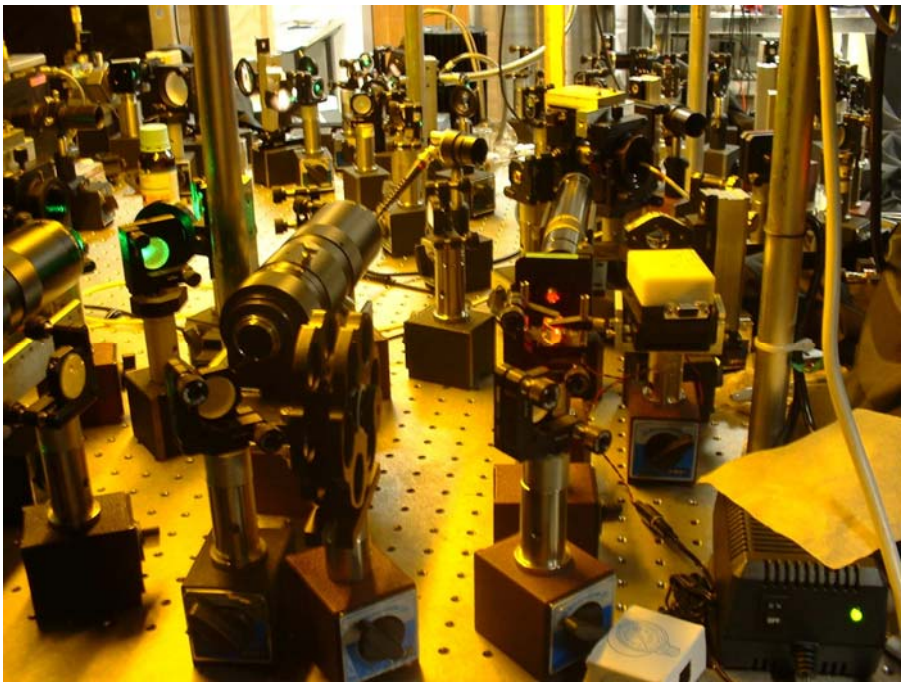

Figure A-5 Photo image of the alignment laser with telescope.

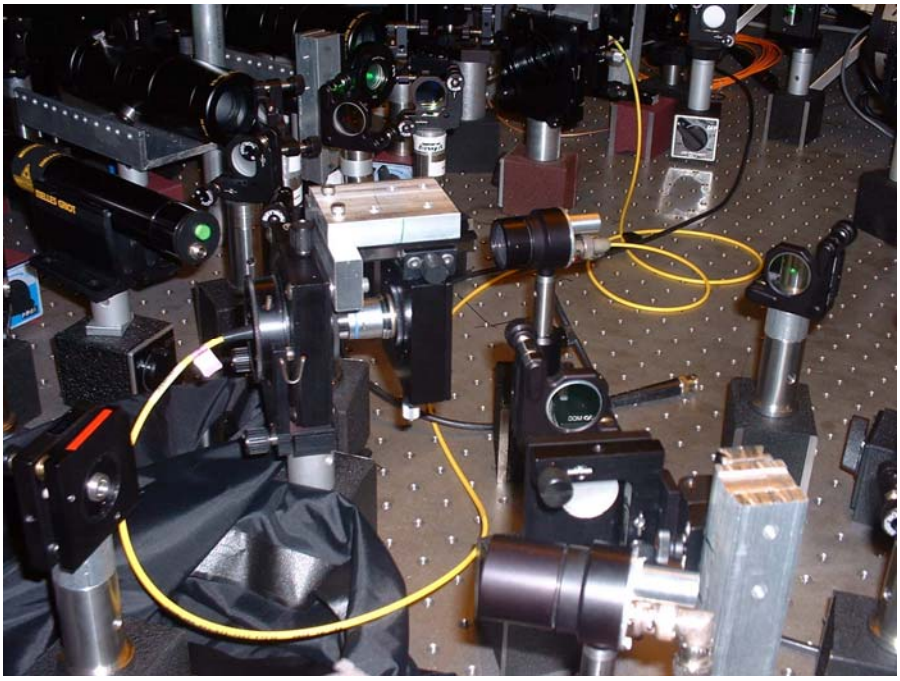

Figure A-6 Photo image of output collimation with single mode fiber.

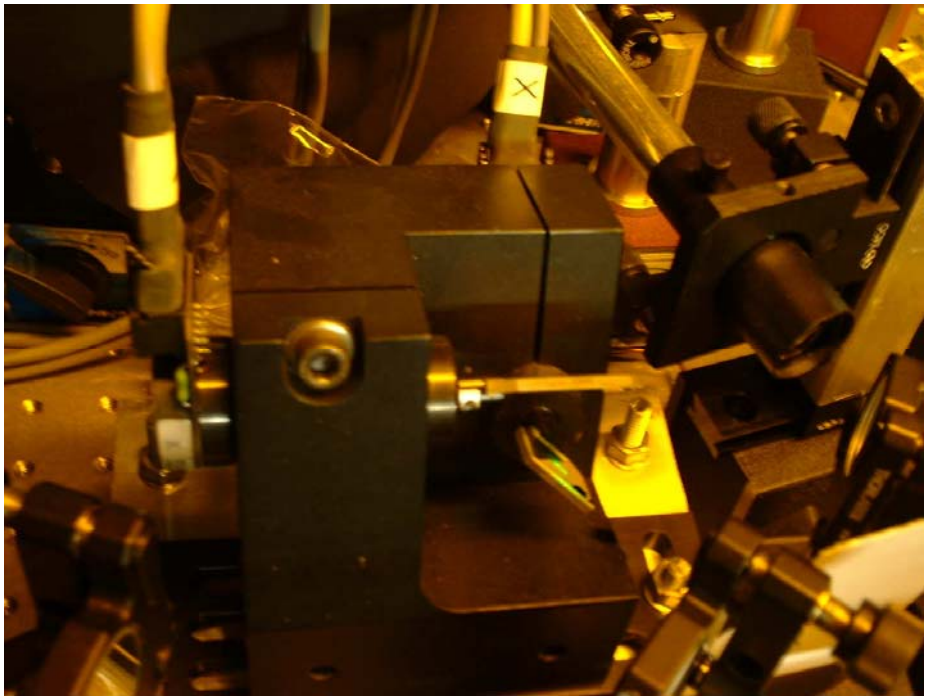

Figure A-7 Photo image of two axes galvo mirrors for beam steering.

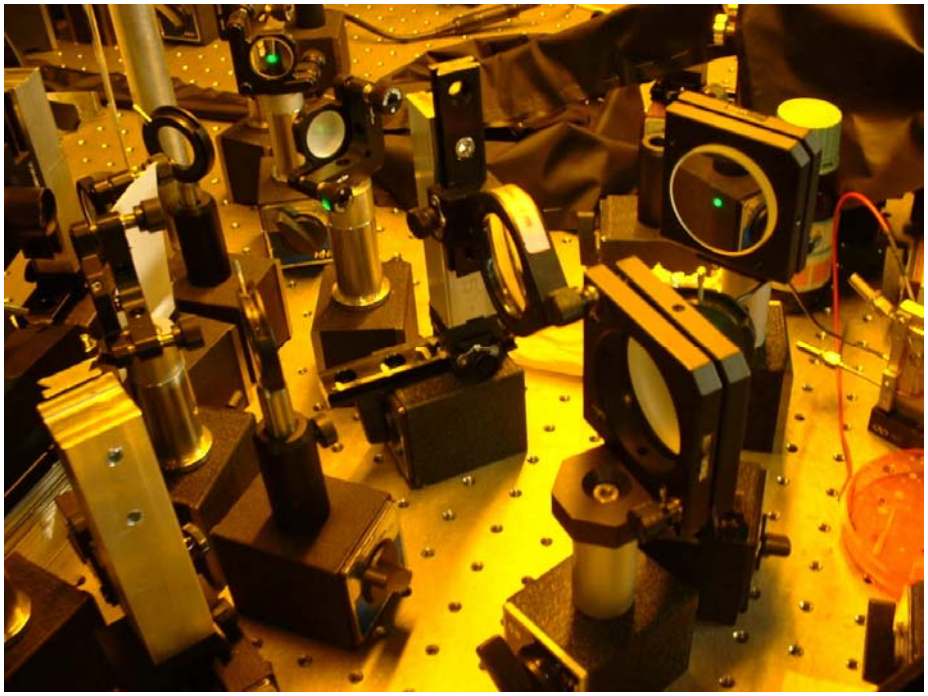

Figure A-8 Photo image of 2f imaging lens with mirrors.

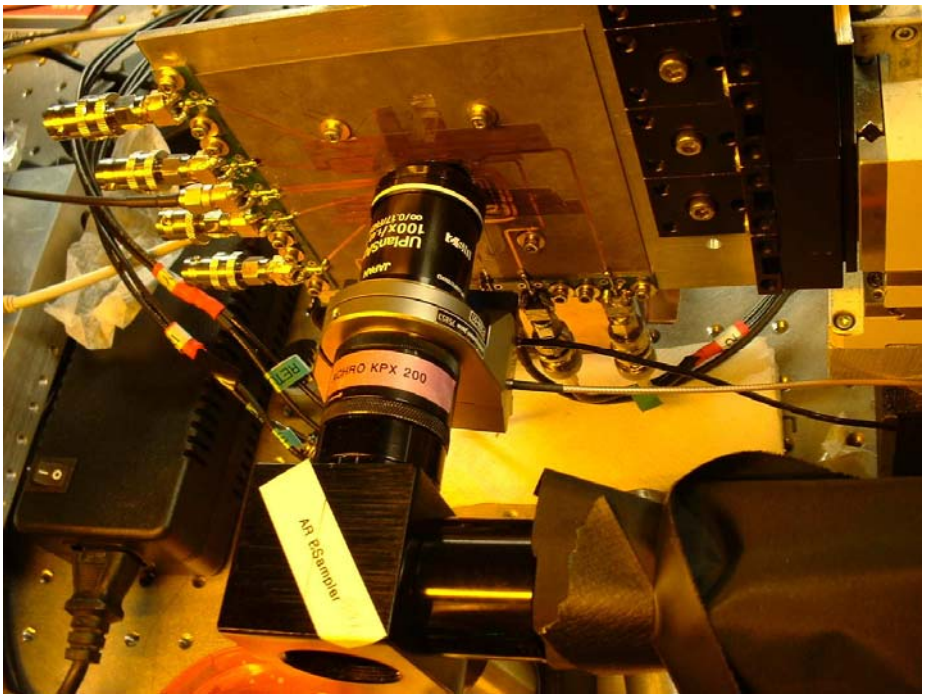

Figure A-9 Photo image of microscope objective with sample mount and beam splitter.

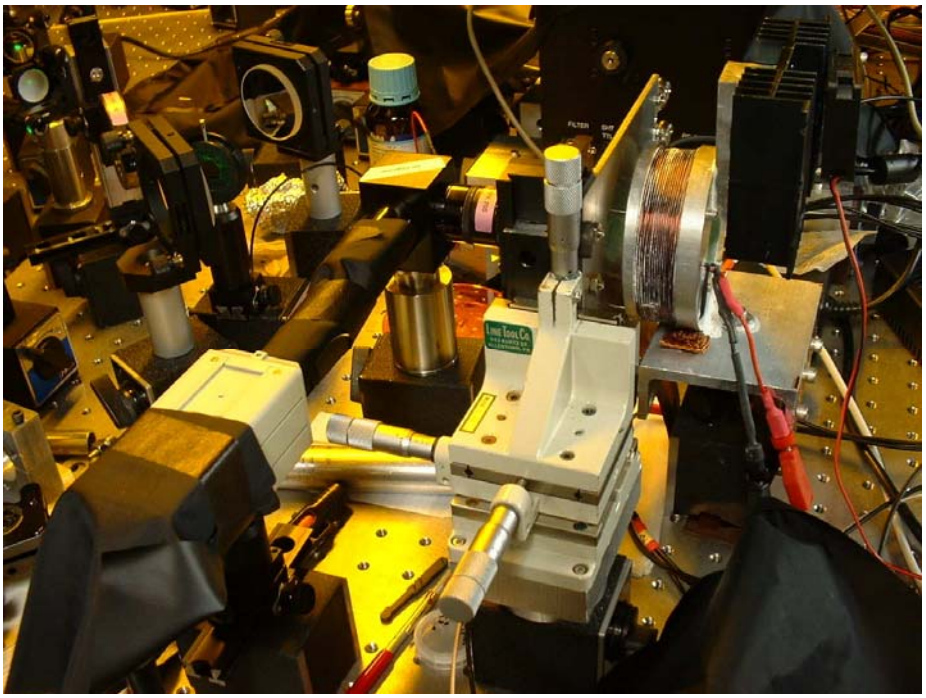

Figure A-10 Photo image of stage, electromagnet, and CCD camera.

Figure A-11 Photo image of covered detection channels.

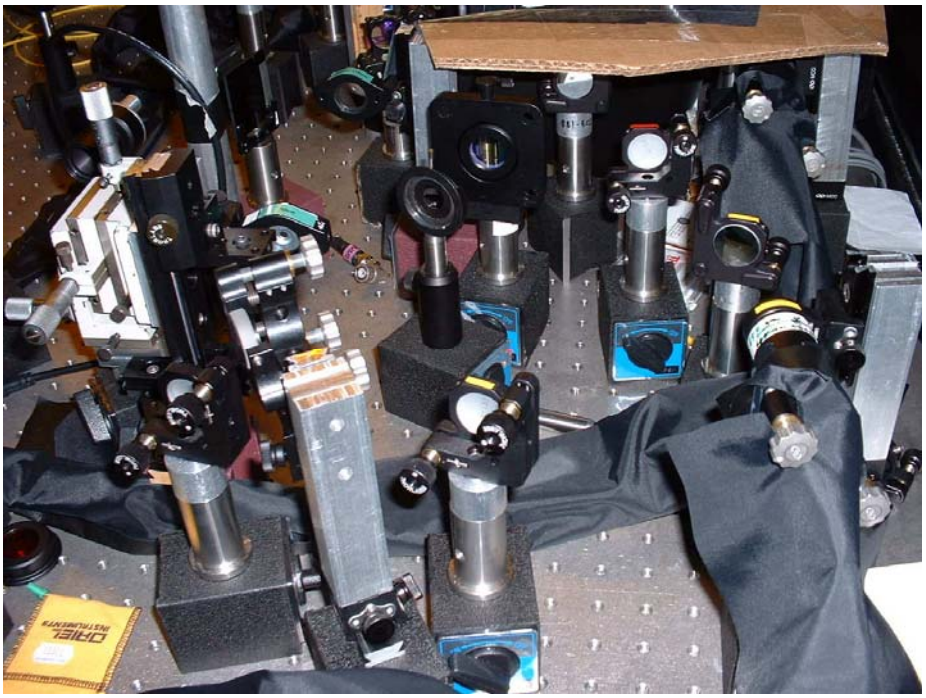

Figure A-12 Photo image of un-covered detection channels.

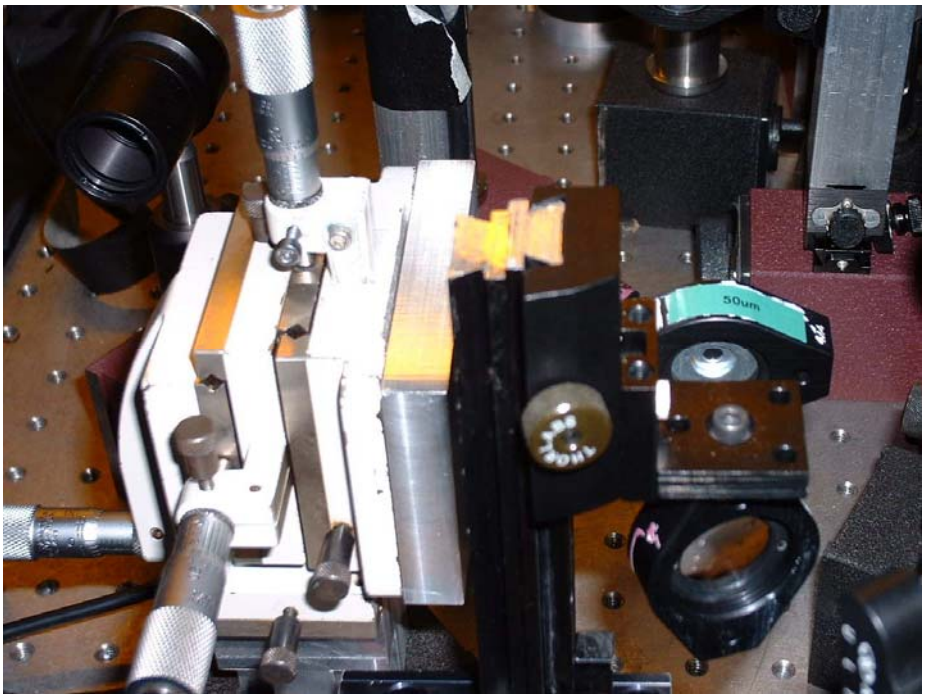

Figure A-13 Photo image of spatial filter using 50μm pin-hole.

Figure A-14 Photo image of a detection channel with 650nm long pass filter in front.

Figure A-15 Photo image of two APDs for single photon detection with multimode fibers.

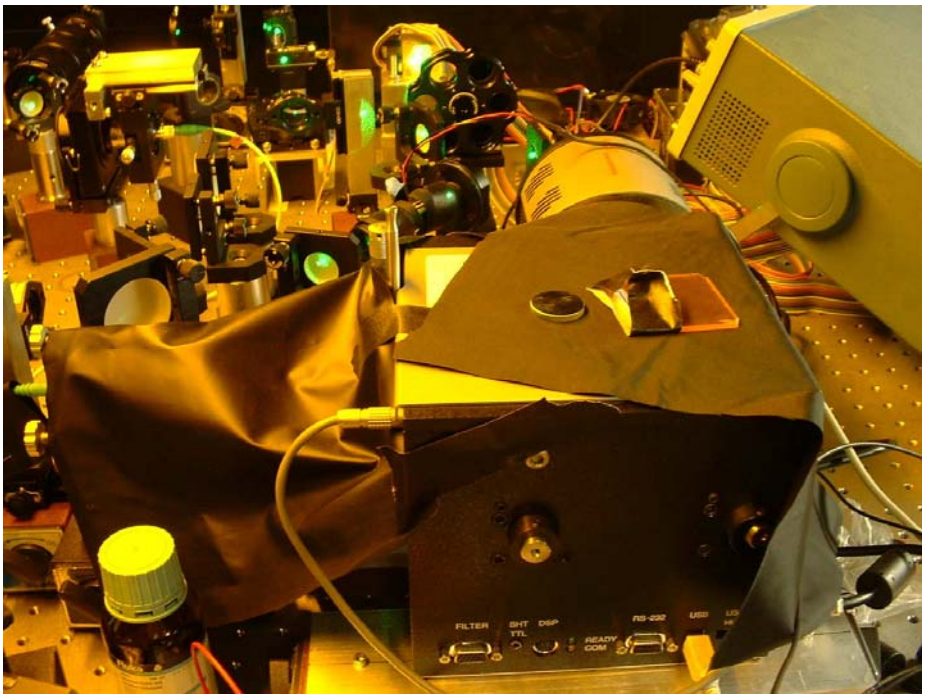

Figure A-16 Photo image of a spectrometer.

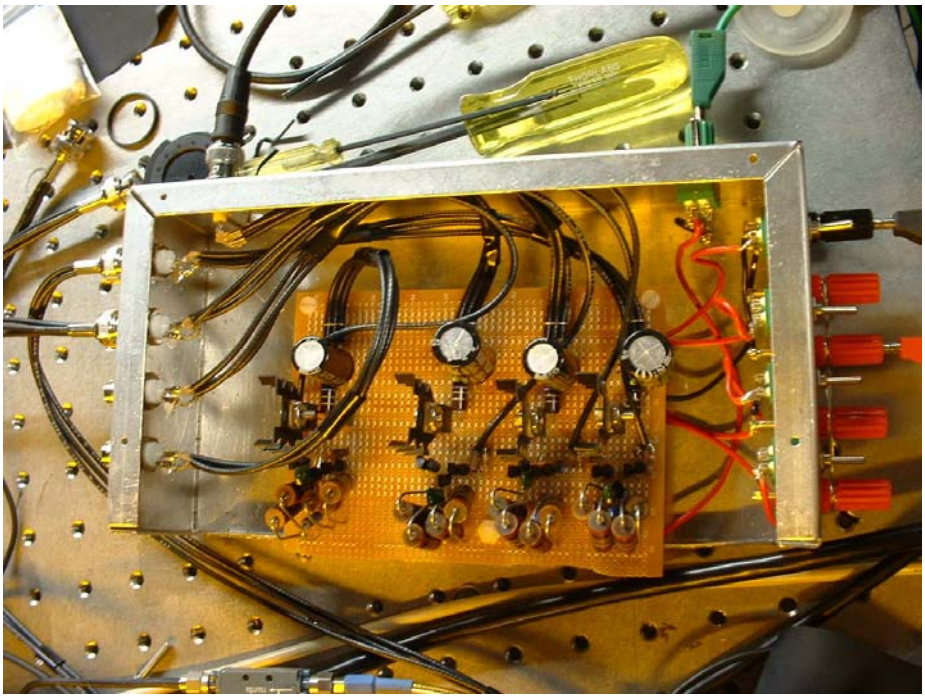

Figure A-17 Photo image of DC current switch for DC magnetic field gradient .

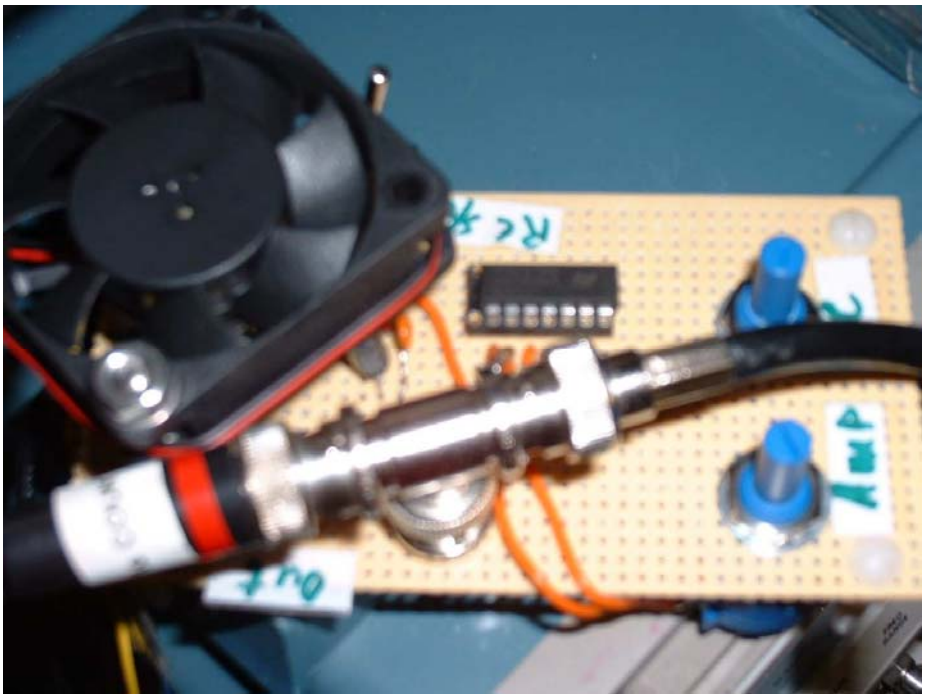

Figure A-18 Photo image of a ramp generator circuit.

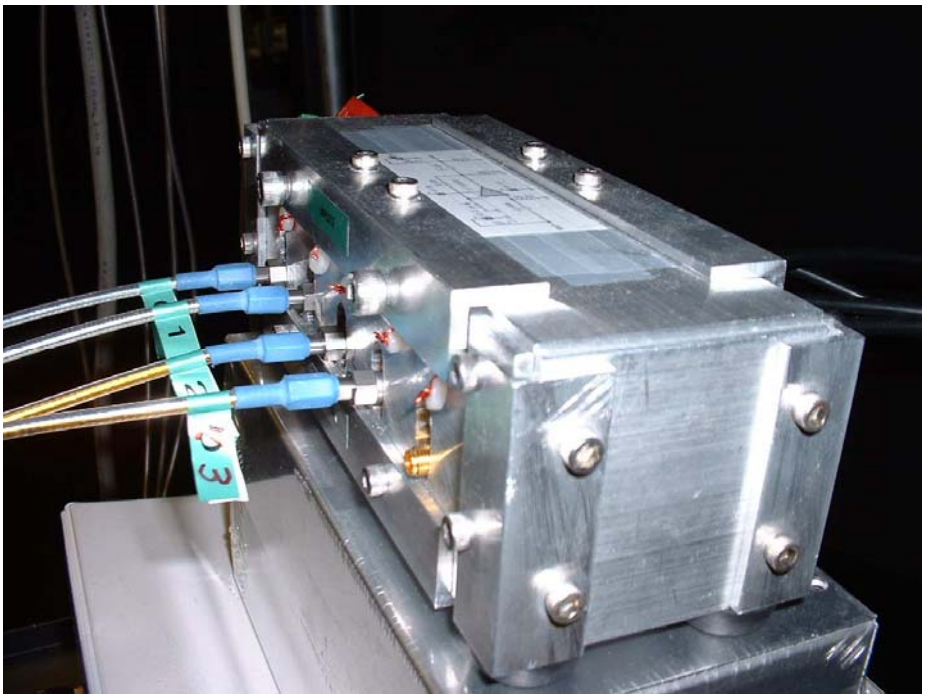

Figure A-19 Photo image of logic converter circuit.

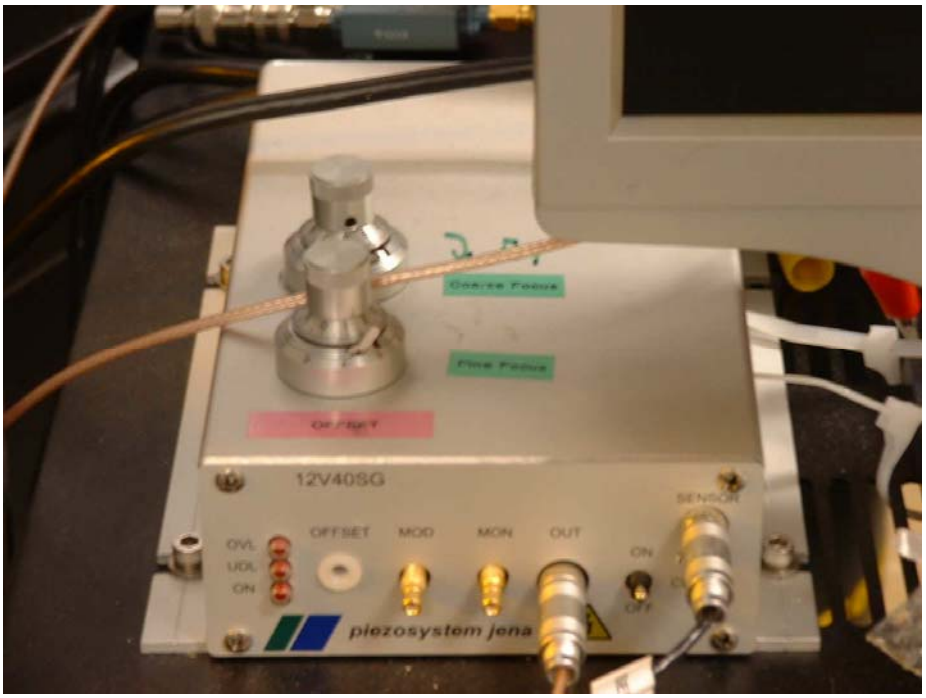

Figure A-20 Photo image of piezo driver for the z-axis lens positioning.

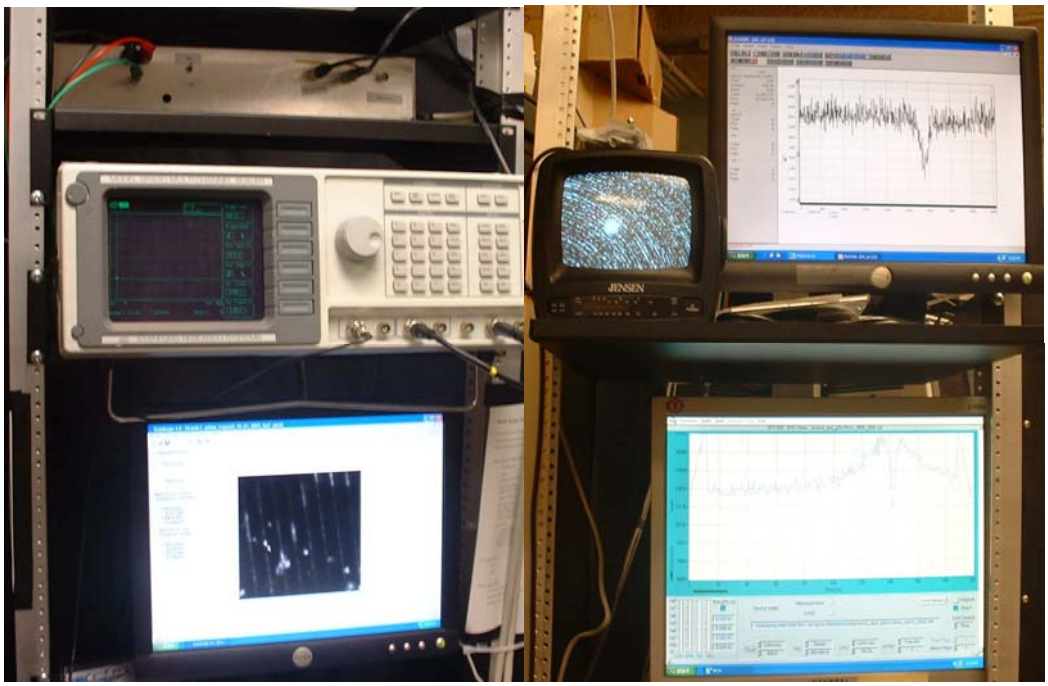

Figure A-21 Photo images of galvo driver with SR430 and Fluorescence image using Scanscope program(left), and ESR and antibunching experiments (right).

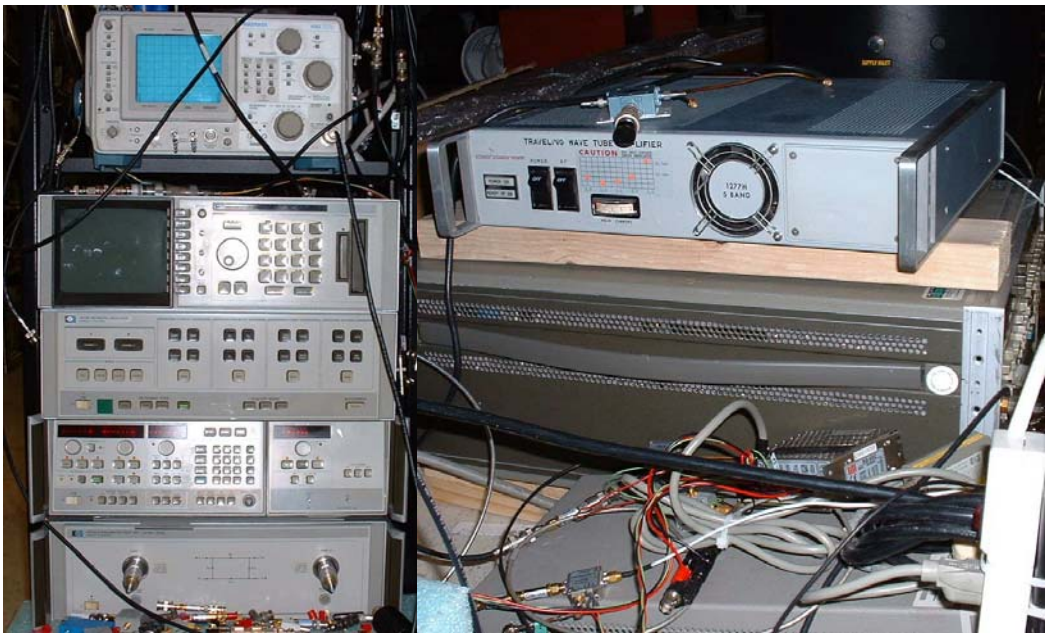

Figure A-22 Photo images of network analyzer and spectrum analyzer (left), and TWT amplifier with microscope switches (right).

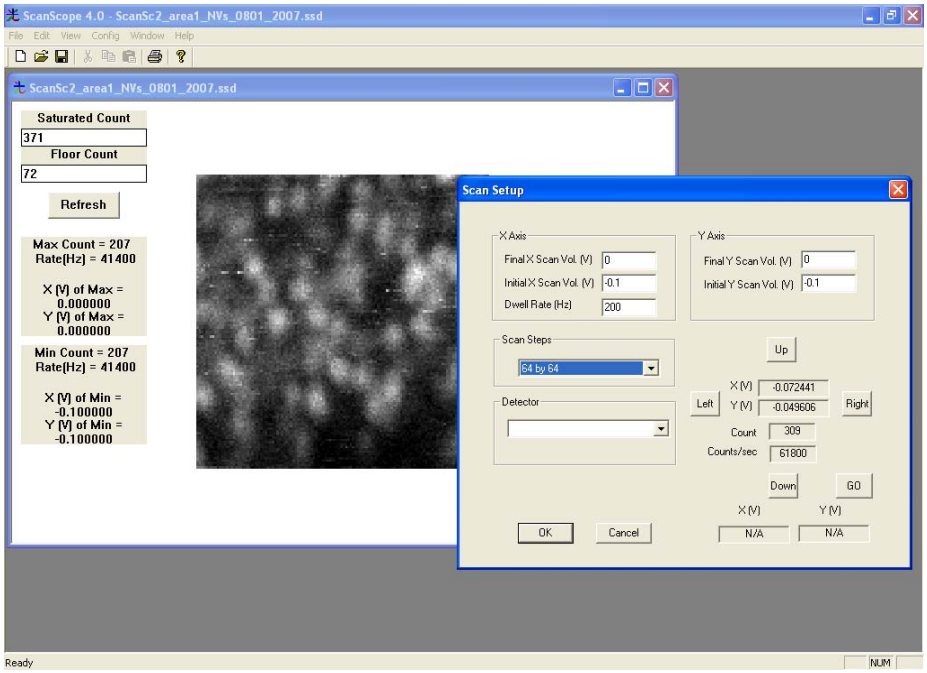

Figure A-23 Screen capture image of Scanscope program for laser scanning fluorescence microscopy developed by colleagues, Dr. Zhijie Deng and Dr. Aleksander Wojcik.

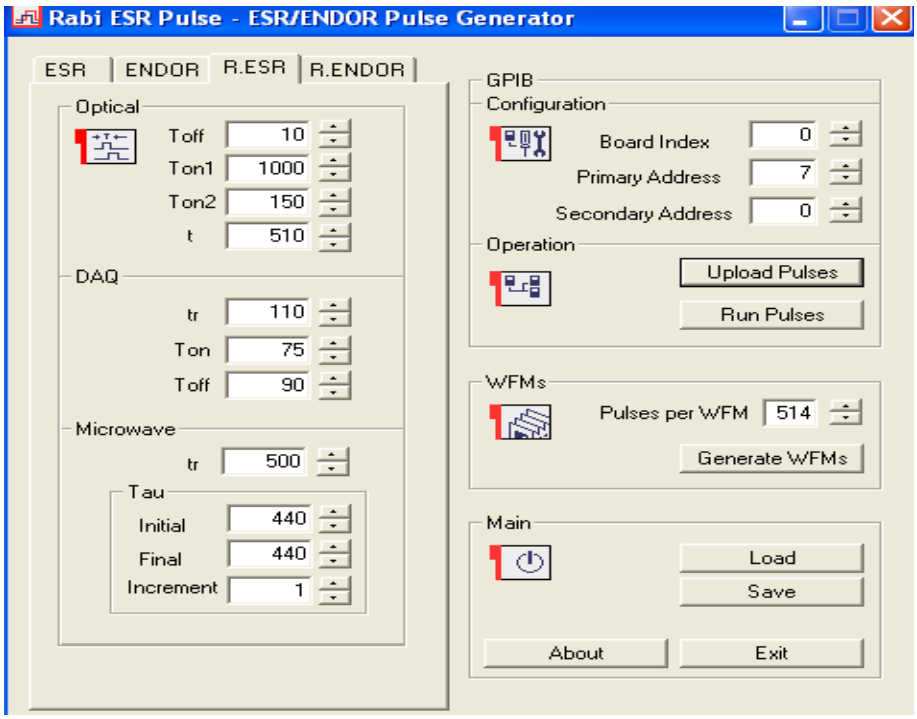

Figure A-24 Screen capture image of pulse sequence generation program developed by a colleague, Dr. Aleksander Wojcik.

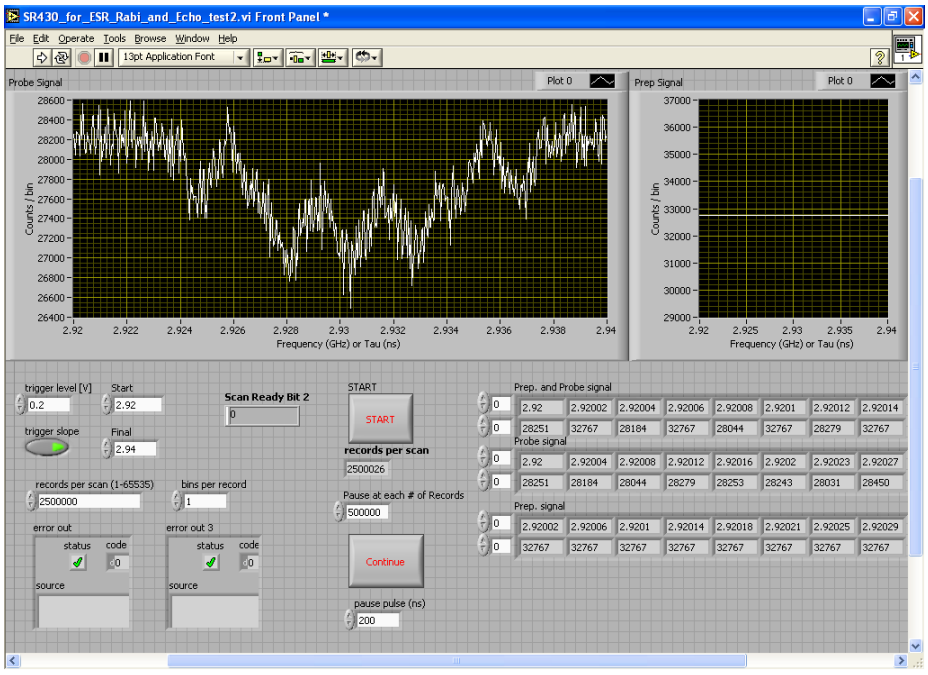

Figure A-25 Screen capture image of Labview VI for pulse mode experiments developed by the author.

VITA

Chang-Seok Shin received his Bachelor of Science degree in Electronics Engineering from The University of Seoul, Korea in 1999. He entered the Electrical Engineering program at Texas A&M University in September 1999 and received his Master of Science degree in August 2002. He then continued his Ph.D. study in the Electrical and Computer Engineering at the Texas A&M University and received his Doctor of Philosophy degree in May 2008. His research interests include fluorescence microscopy, single molecule imaging using electron spin resonance techniques and electron spin envelope modulation techniques, micrometer sized microwave transmission line, micro fabrications by optical lithography and sub-wavelength resonators for local field enhancement and meta-material applications.

Dr. Shin may be reached at the Department of Electrical and Computer Engineering, Texas A&M University, 3128 TAMU, College Station, TX 77843-3128, USA. His email is changshin71@gmail.com.